UNIVERSITY OF COPENHAGEN

THE CENTER OF GRAVITY

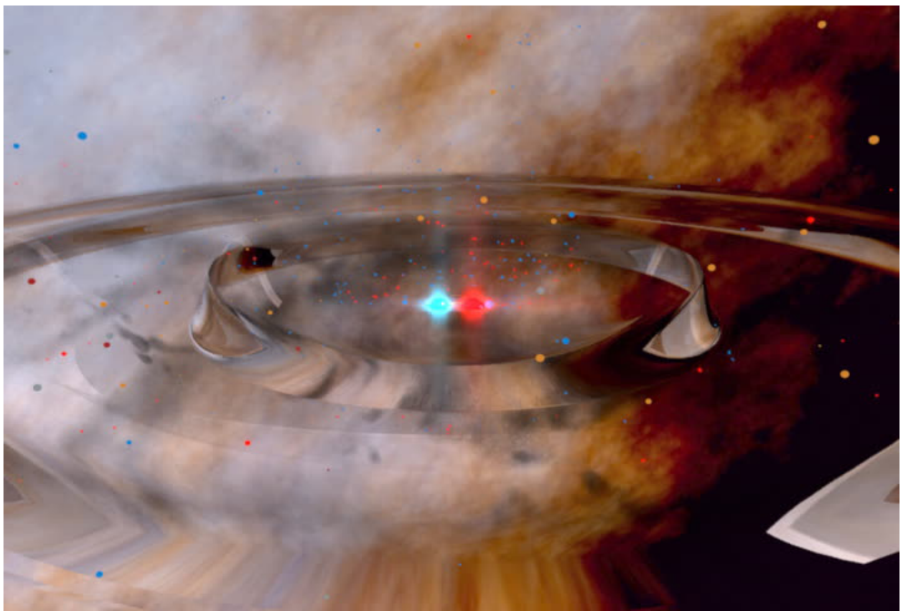

Master's thesis

Gravitational wave lensing - Probing the strong gravity regime

Date: 20^{th} of May 2025

Advisor: Jose María Ezquiaga

Department: Niels Bohr Institute

Faculty: Faculty of Science, Copenhagen University

Author(s): Matilde Serôdio Pereira Neto Garcia

Title and subtitle: Gravitational waves lensing: probing the strong gravity regime

Advisor: Jose María Ezquiaga Bravo

Date: 20^{th} of May 2025

Abstract

The first detection of gravitational waves in 2015 opened the door to gravitational wave physics, which has allowed us to test gravity, astrophysics and cosmology with unprecedented precision. When emitted by a merging binary of compact objects, such as black holes, gravitational waves propagate mostly unaltered through the cosmos. However, if they encounter objects in their path that are massive/compact enough, those will act as cosmic lenses, affecting their properties. Gravitational lensing offers a unique probe of both the large-scale structure of the Universe and the fundamental properties of gravitational wave propagation. Depending on the properties of the wave, the lens, and the overall physical setup, different lensing regimes arise, each leading to distinct phenomenology which require different formalisms and techniques to describe.

This master's thesis gives an overview of different lensing regimes and explores some of the least familiar ones. To start, we go over the weak gravity approximation, where all the information regarding how the wave is amplified, as well as time and phase shifted, is encapsulated in a diffraction integral. This integral can be solved in full, analytically, giving us frequency dependent amplification functions. We test these amplification factors for real waveforms and obtain heavy distortions and modulations in the waveform that lead to mismatches of order ~ 0.3 and amplifications up to order ~ 14 in favorable setups. There is, in parallel, the option of solving this integral for short waves, which yields the creation of discrete images with time delays and relative magnifications, which is rather familiar since it is how electromagnetic radiation is lensed. In strong gravity, we focus on the case of a non-rotating black hole acting as a lens, and start by going over the geometric optics regime which, similarly to light, consists of tracing the trajectory of a massless particle in Schwarzschild metric. We find that, for simplistic active galactic nuclei disk models, gravitational waves emitted by a stellar mass binary source located on the disk can loop around the black hole or get deflected by angles of order $\sim 2\pi$. On the other hand, in the wave optics regime, we solve, through the Regge-Wheeler equation, the scattering of the wave off a black hole and are able to obtain frequency dependent amplification factors. These amplification factors have an overall different behavior from the ones obtained under the weak gravity approximation due to the structure of a black hole when compared to, for example, a point mass. We find that, although the physical system yields small orders of magnitude in the amplification functions, the black hole causes visible and measurable distortions in the wavefront, qualitatively different from the ones in weak gravity, such as polarization mixing and absorption.

There is yet a lot of progress to be done in, for example, studying the effects of the spin of a black hole in the amplification functions and geodesic deviations, and preforming more accurate population studies of binaries in the vicinity of black holes acting as lenses (triple systems, active galactic nuclei disks). There is also much to be done within the setup we analyze in strong gravity, such as considering different physical setups in order to find more prominent lensing signatures, and, for example, applying them to extend current gravitational wave template banks in order to identify these signals in current and future detections.

Table of contents

Abbreviations and notation

GW	Gravitational Wave
BH	Black Hole
BBH	Binary Black Hole
GR	General Relativity
SMBH	Super Massive Black Hole
PML	Point Mass Lens
SPA	Stationary Phase Approximation
LIGO	Laser Interferometer Gravitational-wave Observatory
LISA	Laser Interferometer Space Antenna
HST	Hubble Space Telescope
AGN	Active Galactic Nuclei
SNR	Signal to Noise Ratio
RWZ	Regge-Wheeler-Zerilli

1 Introduction

The first detection of gravitational waves (GWs) in 2015 opened a new window into the cosmos and has allowed us to test Gravity with unprecedented precision - [1]. They were, however, predicted by Einstein's General Relativity (GR) - which is the current theory of gravity - long before they were first detected - [29].

When emitted by a **source**, usually a merging binary, they can be altered by objects in their path as they propagate through the cosmos. These objects have to be large/massive enough to affect the properties of the wave. They are what we call **lenses**, and they deflect the GW's trajectories, delay their arrival and occasionally produce multiple images[1] , not unlike what has been observed for light waves. This means that a different "version" of the original GW reaches the **observer** (detector) here on Earth.

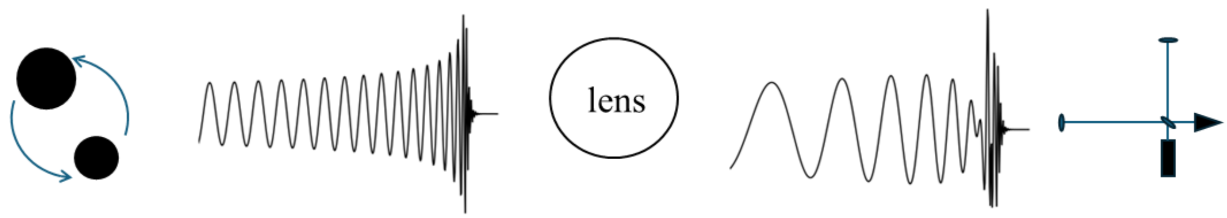

Figure 1: Schematic representation of the lensing of GWs: the source (merging binary) emits a GW whose properties are altered by the lens at the time they reach the observer (here represented by an interferometer).

Gravitational lensing has been thoroughly studied and even detected on several occasions for light waves [38]. The theory, observations, and applications of gravitational lensing constitute one of the most rapidly growing branches of extragalactic astrophysics . However, the prospect of detecting GW lensed signals with next generation ground based (Advanced LIGO, VIRGO and KAGRA, Cosmic Explorer, Einstein Telescope) and space based detectors (LISA) has recently garnered increasing interest in the field. It is predicted that these will routinely detected GW lensed signals [48], allowing us to probe not only lens mass distribution across the universe, but also BBH population in general and properties of the GWs themselves.

Furthermore, due to the nature of GWs as **spin-2 fields** as opposed to light (spin-1 fields), as well as their **characteristically lower wavelengths**, very interesting phenomena is expected to happen, such as mixing of the two polarization states [20, 3, 33] when in the presence of a strong gravitational field; interference and diffraction (wave optics) effects [22]. Nevertheless, not unlike light, it can lead to the production of multiple images with different relative magnifications and arrival times - see figures 2 and 3.

Depending on the scales of the problem, we find ourselves in different **lensing regimes** and the phenomena we expect to observe differs. It is sometimes challenging to know where to draw the lines between all the different regimes; to know which phenomena will be more prominent, and when or if it is valid to make certain approximations.

The goal of this thesis is to go over some of the already very established regimes in lensing and attempt to probe some more unfamiliar scenarios, and hopefully, try to draw a bridge between them.

[1]By images we simply mean discrete peaks in flux intensity, both for light and GWs.

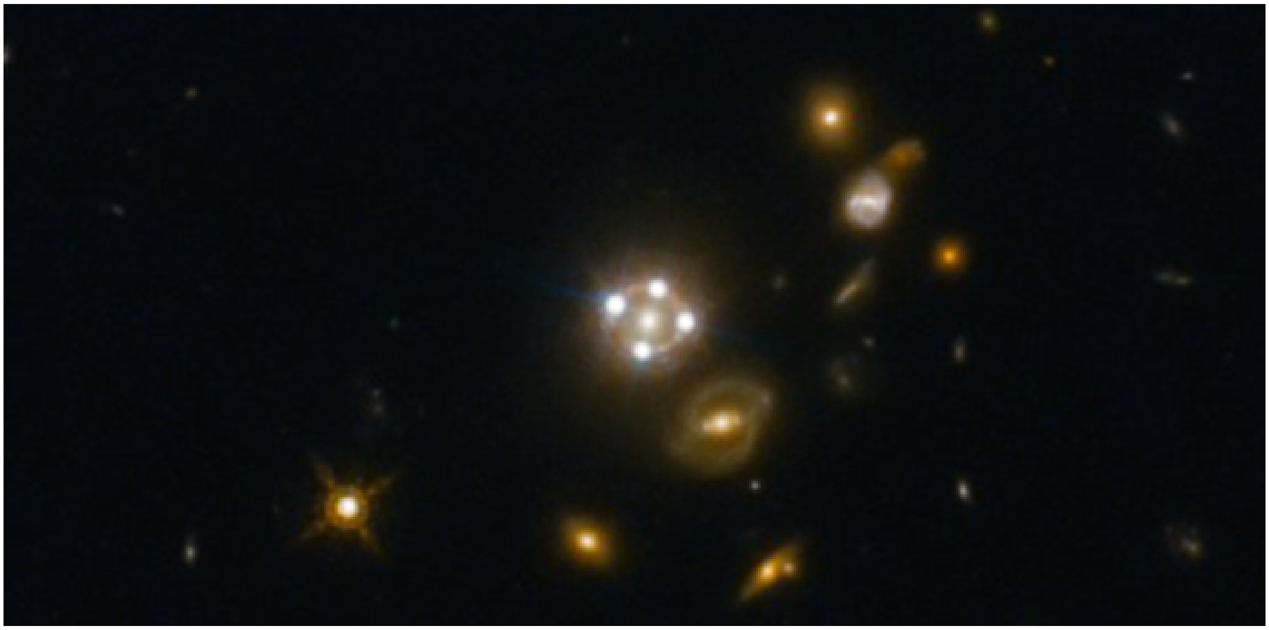

Figure 2: Multiple imaging of HE0435-1223 quasar observed with the HST (Hubble Space Telescope) - we observe the same source 4 times in the shape of cross due to lensing from intervening objects aligned with the line of sight source-observer (Einstein cross).

Figure 3: Observation of the Einstein ring phenomena by the HST.

1.1 The lensing landscape

Depending on the particular physical setup of our system (source-lens-observer), lensing leads to different phenomenology. The three main variables/scales of the problem are:

- the wavelength of our GW compared to the size of the lens;
- the compactness of the lens - i.e., if we treat it as a classic Newtonial potential or if we use a strong gravity framework (this will also be dependent on how close the source is to the lens);
- the impact parameter - the perpendicular distance between the path of the wave and the center of the potential.

If the wavelength, when compared to the lens, is small enough such that we can treat the wave as a ray, we are in the **geometric optics** regime. This means that we can track the trajectory of the wave as if a massless particle was propagating along a null geodesic which, as with light, is deflected. In this regime, it is possible to observe the production of multiple images, the ray "looping" around a BH acting as a lens, and other interesting phenomena - top panel of figure 4.

In geometric optics, it is also important to distinguish between **strong** and **weak lensing** - sub-panel of figure 4. The separation of these two regimes is dictated by the impact parameter. In weak lensing (at large impact parameters), our ray is simply deflected at an angle such that the actual source position and the apparent source position don't coincide. In strong lensing, which is what happens when the impact parameter is small, we observe multiple images of the source, all arriving at different times.

If the wavelength has a comparable size to that of the lens, we enter the **wave optics regime**. In this regime, we can't treat the wave as a simple geodesic since the multiple geodesic paths are expected to cross - i.e., different sections of the wavefront interfere - bottom panel of figure 4. Even though the terminology of weak and strong lensing is not used in wave optics, since it is associated with image multiplicity, **the impact parameter** plays a very important role on how prominent lensing effects will be in this regime as well.

Lastly, the compactness of the lens will also deeply affect the problem at hands: being lensed by a galaxy or galaxy cluster as opposed to being lensed by a BH are two very different phenomena. If we work under the **strong gravity** framework, we observe features such as polarization mixing and absorption which we cannot when assuming a **Newtonian potential** - left versus right panel of figure 4.

Essentially, each corner or region of figure 4 represents how a GW is lensed, or which regime of lensing we are in. Each corner requires different mathematical techniques and physical approximations to approach the problem at hands. For example, geometric optics results are obtained by using the WKB (Wentzel-Kramers-Brillouin) approximation [21], which yields a geodesic equation that can be solved for a strong gravitational field - [7, 6, 18]. The weak field approximation stems simply from the statement $R_s/R \ll 1$, which turns the mathematical problem into an integral that encapsulates the information on the overall amplification and time delay of the wave (which is indifferent to polarization) - [40, 42, 31, 26]. This turns the lensing problem into a much easier one. When solving for strong gravity, on the other hand, for longer wavelengths, lensing turns into a scattering problem - where we have an incoming wave hitting a BH. The problem is solved using **Black Hole Perturbation Theory** - [49, 34, 10] and it is not as trivial. We will go over some of these mathematical techniques and study the outcome, as well as what it can mean for observational prospects.

To understand the roots for the techniques used in solving the problem of lensing for different regimes, as well as how they are derived, we will start by studying what exactly are GWs and how they propagate. In the following section, we will show how to derive an equation that describes how GWs propagate in an arbitrarily curved background metric from linearized gravity.

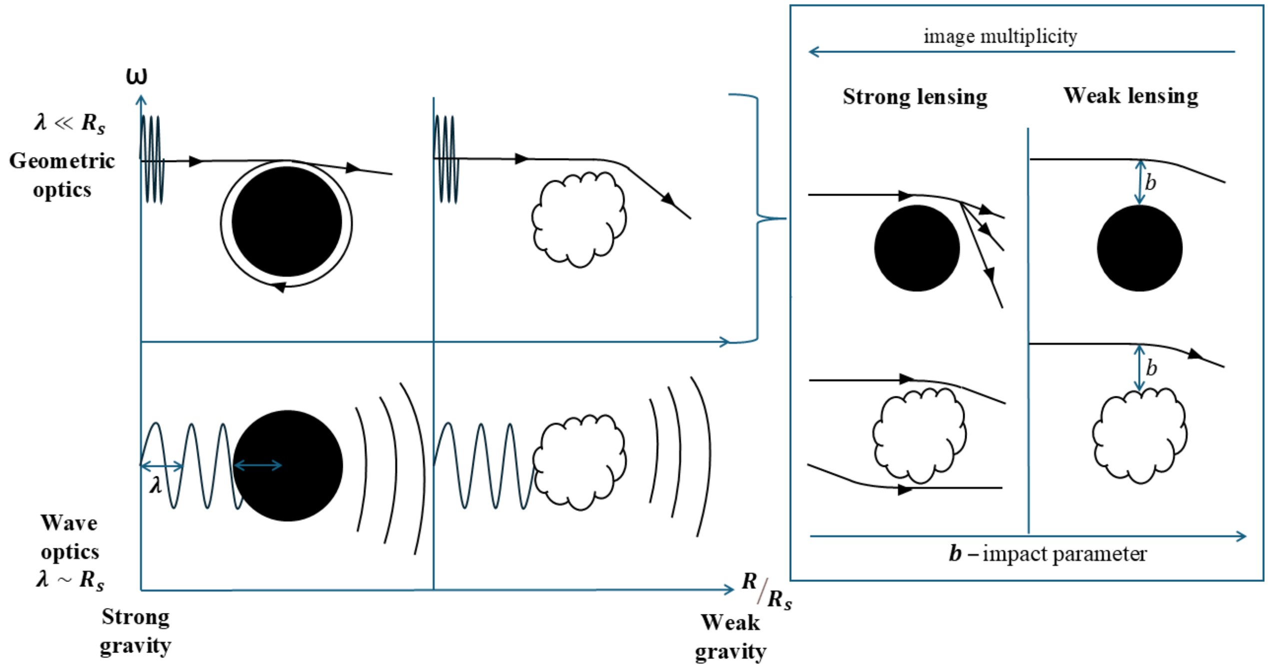

Figure 4: A schematic representation of the different regimes in lensing and how important scales in the problem set the regime we are in.

1.2 How gravitational waves propagate

Gravitational waves are features of Einstein's GR theory which can be described as a small perturbation around some specific metric $g_{\mu\nu}$. Even though, for most cases, we can consider that metric to be either Minkowski for simplicity or FRLW (Friedmann–Lemaître–Robertson–Walker) if we want to describe cosmological propagation, at this point we will only make one assumption about the background metric: it is **curved**. Furthermore, we will assume that our metric perturbation (which encodes the information of our gravitational waves) has a small enough amplitude leading to the consideration of only linear order terms. This means that we can decompose our metric (background + perturbation) as seen in equation (1) [2]:

$$g_{\mu\nu} = g^{(B)}_{\mu\nu} + h_{\mu\nu}, \tag{1}$$

and only consider linear orders of that perturbation ($\mathcal{O}(h^2) \sim 0$) - this framework of GR is called **linearized gravity**. Essentially, $g_{\mu\nu}$ is our perturbed metric, $g^{(B)}_{\mu\nu}$ is the background and $h_{\mu\nu}$ is the perturbation.

The Ricci tensor for such a metric can be expanded around the background in orders of the amplitude of the perturbation($\mid h_{\mu\nu} \mid \leq \mid g^{(B)}_{\mu\nu} \mid \mathcal{A}$), as such:

$$R_{\mu\nu} = R^{(B)}_{\mu\nu} + R^{(1)}_{\mu\nu} + R^{(2)}_{\mu\nu} + \ldots \tag{2}$$

Each of the terms in this sum encodes a different kind of information regarding how our perturbation affects the background and vice-versa. For example, the background Ricci tensor, denoted by $R^{(B)}_{\mu\nu}$ tells us how our perturbations induce curvature (on top of the already curved background metric) in a non-linear way, meaning it is non-linear in $\mathcal{A}$. Our

[2] one can also follow this derivation from chapter 35.13 - 35.14 of [29]), or even the lecture notes for the Black Holes and Gravitational Waves course - [14], [27]

focus, however, will be in the part of the Ricci tensor that tells us **how our perturbation propagates in an arbitrary background metric**, which is $R^{(1)}_{\mu\nu}$. Furthermore, we are going to assume that, despite being in a curved background, which is induced by the presence of mass, our perturbation is propagating in the vacuum outside that mass distribution - i.e., we wish to solve $R^{(1)}_{\mu\nu} = 0$. It is shown in appendix A how to exactly derive an expression for $R^{(1)}_{\mu\nu}$ that gives us equation (3):

$$\frac{1}{2}(-\Box h_{\nu\mu} - D_\nu D_\mu h + 2D^\lambda D_{(\nu} h_{\mu)\lambda}) = 0, \tag{3}$$

where $\Box$ is the D'Alembertian operator of the background metric, and h is the trace of our perturbation $h = g^{\alpha\lambda(B)} h_{\alpha\lambda}$. The d'Alembertian operator is the contraction of two covariant derivatives $\Box = D_\lambda D^\lambda$ matching the background metric. From now on that all the mentioned operators will refer to the background metric.

Furthermore, we introduce the trace reversed metric perturbation as

$$\bar{h}_{\mu\nu} = h_{\mu\nu} - \frac{1}{2} g^{(B)}_{\mu\nu} h, \tag{4}$$

simply because it allows us to write a more compact propagation equation. It is called trace reversed because its trace is symmetric to that of the original perturbation, i.e. - $\bar{h} = -h$. This property can easily be tested out simply by contracting the trace reserved perturbation $\bar{h}_{\mu\nu}$ with the metric to get $\bar{h} = g^{\mu\nu}\bar{h}_{\mu\nu} = h - \frac{1}{2}4h = -h$. Plugging the trace reversed metric perturbation into Eq.(3) gives:

$$\Box\bar{h}_{\mu\nu} - \frac{1}{2} g_{\mu\nu}\Box\bar{h} + D_\nu D_\mu h - 2D^\lambda D_{(\nu}\bar{h}_{\mu)\lambda} + D^\lambda D_{(\nu} g_{\mu)\lambda}\bar{h} = 0. \tag{5}$$

In order to further simplify this expression, one can write $\bar{h} = g^{\mu\nu}\bar{h}_{\mu\nu}$ explicitly and contract the two background metrics on the second term (this can be done because the metric $g^{\mu\nu}$ is constant with respect to the d'Alembertian operator since they both refer to the background metric). This way, the first and second term simplify to $-\Box\bar{h}_{\mu\nu}$. A similar strategy can be applied to the last term - we pull the metric out to lower the index of the first derivative to give us $D_\nu D_\mu \bar{h}$, which cancels out with the third term. These two simplifications render the previous equation substantially more straightforward:

$$\Box\bar{h}_{\mu\nu} + 2D^\lambda D_{(\nu}\bar{h}_{\mu)\lambda} = 0. \tag{6}$$

As a final step, we will use the general commutation property of the covariant derivative

$$D_\mu D_\nu \bar{h}_{\alpha\beta} = D_\nu D_\mu \bar{h}_{\alpha\beta} + R^{\gamma(B)}_{\ \mu\nu\beta}\bar{h}_{\alpha\gamma} + R^{\gamma}_{\ \mu\nu\alpha}\bar{h}_{\gamma\beta}, \tag{7}$$

in order to rewrite the second term in Eq.(6) in terms of Riemann and Ricci tensors:

$$D^\lambda D_{(\nu}\bar{h}_{\mu)\lambda} = 2D_{(\nu} D^\lambda \bar{h}_{\mu)\lambda} + 2R^{(B)}_{(\mu\lambda}\bar{h}_{\nu)\lambda} + g^{\lambda\alpha} 2R^{\gamma(B)}_{\ \alpha(\nu\mu)}\bar{h}_{\mu\lambda}. \tag{8}$$

The first term vanishes due to the gauge freedom of our metric perturbation [3]. This gauge allows us to choose a coordinate transformation that follows $D^\mu\bar{h}_{\mu\nu} = 0$ (see Eq.s (35.65)-(35.66) of [29]).

Because we have turned our attention to vacuum, even though we have a curvature, the only source of energy-momentum $T_{\mu\nu}$ (in the region of space-time where the GW is propagating) comes form the perturbation itself. However, since our perturbation curves space-time in a non-linear way, in fact, GWs contribute to $T_{\mu\nu}$ at second order, this indicates

[3] To cite Regge and Wheeler [37], "different waves can represent the same physical phenomena viewed in different coordinates". Therefore, it is useful to use gauge vectors to alternate between coordinate systems, but imposing that the same physical phenomena is being described.

that the Ricci tensor $R_{\mu\nu}$ will be $\mathcal{O}(h^2)$. Therefore, when contracted with $\bar{h}_{\mu\nu}$, it becomes negligible, which allows us to dispose of the second term. The third term, using Riemann curvature symmetries, reduces to $R^{(B)}_{\mu\alpha\nu\beta}\bar{h}^{\alpha\beta}$, turning our Eq.(6) into:

$$\Box\bar{h}_{\mu\nu} + 2R_{\mu\alpha\nu\beta}\bar{h}^{\alpha\beta} = 0. \tag{9}$$

This equation is of vital importance since it describes **the propagation of a small perturbation through any curved background metric**. In the context of lensing, our lens structure is embedded in the information about the curvature of the space-time, since, as we know from GR, **Mass = Curvature**. For a lot of the scenarios, the space-time is approximated to be flat everywhere except for a slight curvature next to the lens (weak field gravity), which is a (somewhat limited) realistic and yet extremely simplifying assumption.

In its full generality, Eq.(9) sets the framework for all of the phenomena related to GW propagation in the cosmos, and we will go through some of the different scenarios that arise from solving this equation through various methods. Some of these methods include, as mentioned, using a weak gravitational potential; or even assuming high frequency so that we can observe phenomena such as gravitational deflection of the propagation direction, similarly to light. At low enough frequencies, we can scatter the GWs off the background curvature and observe "tails", which are non linear effects in the GW, but this will be left for future work.

So, essentially, to solve the problem of lensing, what we need to do is to **propagate our gravitational perturbation** $h_{\mu\nu}$ **through some background metric**. This background metric will be dictated by the local distribution of mass, which is our lens. We will focus exclusively on two different background metrics in this work: a **nearly flat metric** in section 2 for the **weak gravity approximation** , and the **Schwarzschild metric** in section 3 for **strong gravitational fields.**

In strong gravity, this project tackles the lensing problem from two different fronts. In geometric optics, we **trace geodesics,** which is quite well established for Schwarzschild metric. In wave optics, we resort to **Black Hole Perturbation Theory**. Therefore, it is useful to take a short crash course on this topic to become familiarized with it - subsection 1.3.

1.3 Crash course in Black Hole Perturbation Theory

Long after Karl Schwarzschild found the solution to Einstein's field equations for a spherically symmetric distribution of matter in vacuum in 1916, physicists started worrying about the stability of this solution, mostly since it featured a singularity. The question of how a Schwarzschild singularity would respond to a small initial perturbation was first posed by Tulio Regge and John Wheeler in 1957 [37]. To answer this question, the authors propose the methodology introduced in section 1.2 of considering some certain background metric $g^{(B)}_{\mu\nu}$, which, in our case, is Schwarzschild, with a small perturbation $h_{\mu\nu}$ for which they account only for first orders. When solving for the condition $\delta R_{\mu\nu} (= R^{(1)}_{\mu\nu}) = 0$, the authors, recurring to Riemannian geometry experts - [13], arrive at a number of second order differential equations for the components of $h_{\mu\nu}$, which is the information encoded in the propagation equation (9) if one were to use the Schwarzschild metric instead of a generalized curved metric.

Similarly to how we solve any second order differential equation, it is useful to preform a separation of variables, such that each solution can be written as a product of functions, each dependent on a single coordinate (t, r, θ, ϕ). The symmetry of the metric allows for the definition of angular momentum with respect to the 2-$\mathcal{D}$ manifold $(t, r) = cte$. Under these rotations, each component of the metric perturbation transforms differently , namely, as scalar, vector and tensor quantities. In particular, the ten components of the metric perturbation (instead of sixteen because it's symmetric) transform like three scalars - h_{ij} for $i, j = (t, r)$; two vectors - represented by $(h_{kl} \quad h_{mn})$ where for both components, one of the indices $\in (t, r)$ and the other one $\in (\theta, \phi)$; and one second order tensor which are the components of the perturbation on the unit sphere denoted by H_{pq} for $p, q = (\theta, \phi)$:

$$h_{\mu\nu} dx^{\mu} dx^{\nu} = \begin{pmatrix} h_{tt} & h_{tr} & (h_{t\theta} & h_{t\phi}) \\ h_{rt} & h_{rr} & (h_{r\theta} & h_{r\phi}) \\ (h_{\theta t} & h_{\theta r}) & H_{\theta\theta} & H_{\theta\phi} \\ (h_{\phi t} & h_{\phi r}) & H_{\phi\theta} & H_{\phi\phi} \end{pmatrix}. \tag{10}$$

Therefore, one is forced to extend the known definition of scalar spherical harmonics into **vector and tensor harmonics spherical harmonics** . Initially, Regge and Wheeler used the harmonics present in Eq. (6) to (11) of [37], but, many years later, Martel and Poisson [25] proposed a different set of harmonics. However, all of them share the property of being orthogonal and being defined with respect to the indices (ℓ, m), with $-\ell \leq m \leq \ell$, which are the angular momentum and its projection on the z-axis. In both cases, when generalizing spherical harmonics to vector and tensor ones, one is forced to divide the solutions into **even parity** , $(-1)^{\ell}$, and **odd parity** , $(-1)^{\ell+1}$.

Having written the perturbation in terms of these spherical harmonics - see Eq.(12) and (13) of [37], one can focus on solving the differential equations for the t and r dependent functions. Initially, we start by having **three unknown radial functions for odd perturbations** and **seven unknown functions for even perturbations**.

The first step in simplifying them is to assume our perturbation has a defined frequency and, therefore, the time dependence can be described by $\exp[-i\omega t]$. Following this, the authors introduce a canonical gauge/coordinate transformation which reduces the number of independent radial functions. We are then left with:

- Two radial functions - $h_1(r)$ and $h_2(r)$ - for odd perturbations;
- Four radial functions - $H_0(r)$, $H_1(r)$, $H_2(r)$ and $K(r)$ - for even perturbations.

The explicit differential equations for each of these functions, that arise from solving each component of $\delta R_{\mu\nu} = 0$, written in the Regge-Wheeler gauge, were first derived in the odd parity sector by the authors of [37]. Afterwards, Vishveshwara completed the analysis by exploring the even perturbations - [45, 12], and analyzing these equations under a different set of coordinates [4]. Using the Einstein's field equations and algebraic manipulations, one is able to encode the information of all of the radial functions into the functions $\psi^{even}_{\ell m}$ and $\psi^{odd}_{\ell m}$, both of them obeying an equation of the kind:

$$f\partial_r\Big(f\partial_r\psi^{\bullet}_{\ell m}\Big) + \Big(\omega^2 - V^{\bullet}_{\ell m}\Big)\psi^{\bullet}_{\ell m} = 0, \quad \text{where } \bullet = \{odd, even\} \text{ and } f = 1 - \frac{2M}{r}. \tag{11}$$

The potentials $V_{\ell m}$ are called the **effective potentials** and, even though they are different for the even and odd parity sectors, they are both potential barriers that approach zero at infinity ($r_\star \to +/-\infty$, or $r \to +\infty/2M$). The odd parity potential is called Regge-Wheeler and was first derived in [37] and the even parity one is called Zerilli and was explicitly derived in 1970 by Frank J.Zerilli - [50]. They are given by:

$$V^{\text{odd}}_{\ell m} = f\Big(\frac{\ell(\ell+1)}{r^2} - \frac{6M}{r^3}\Big) \quad \text{and} \quad V^{\text{even}}_{\ell m} = \frac{2f}{r^3}\frac{\lambda^2(1+\lambda)r^3 + 3\lambda^2 M r^2 + 9M^2(\lambda r + M)}{(3M+\lambda r)^2}, \tag{12}$$

$$\text{with } \lambda = \frac{(\ell+2)(\ell-1)}{2}. \tag{13}$$

Since we aim to construct the gravitational waves at infinity, which is where the observer lies, we are interested in seeing the behavior of the perturbations at the boundary. Particularly, given the shape of the potentials, we can set the boundary conditions such that the waves are **purely ingoing at the horizon** since all the radiation is being generated by

[4] In Kruskal coordinates, it is shown that the singularity at $r = 2M$ that spherical coordinates display is simply a mathematical artifact, so the author decided to extend the analysis to these sets of coordinates.

sources outside of the black hole and **both ingoing and outgoing at infinity (the time and angular dependencies are suppressed here)** :

$$\psi^{\bullet}_{\ell m} \overset{r\to\infty}{\sim} A^{\text{in}}_{\ell m} e^{-i\omega r_\star} + A^{\text{out}}_{\ell m} e^{i\omega r_\star} \tag{14}$$

$$\psi^{\bullet}_{\ell m} \overset{r\to 2M}{\sim} e^{-i\omega r_\star} \tag{15}$$

Keep in mind that, unlike what is done in the study black hole quasi-normal modes, our **frequency is purely real-** in [37, 45], the authors find that perturbations with purely imaginary frequencies diverge at the boundaries. If one defines the reflectivity of the black hole as the ratio:

$$\mathcal{R}_{\ell m}(\omega) = \frac{A^{\text{out}}_{lm}}{A^{\text{in}}_{\ell m}} \equiv |\mathcal{R}_{\ell m}| e^{i\Theta_{\ell m}}, \tag{16}$$

then the quasi-normal mode frequencies $\omega = \omega^0 - i\Gamma$ are those for which the reflectivities diverge. However, with real frequencies, we are restricted to the case in which this reflectivity is finite. Consider an incoming gravitational wave from infinity $e^{-i\omega(t+r_\star)}$ hitting the black hole. This wave will be partially reflected off the potential barrier and sent back to infinity according to the black hole **reflectivities** $\mathcal{R}_{\ell m}(\omega)$; and partially transmitted through the barrier according to the **transmission coefficients** $\mathcal{T}_{lm}(\omega)$. These coefficients are known as the **grey-body factors** of the black hole and can be obtained via integration of the RW (Regge-Wheeler) and Zerilli equations -[16, 36]. The reflectivities are function of the dimensionless frequency ωM as such:

$$|\mathcal{R}_{\ell m}| = 1 + \mathcal{O}[(\omega M)^{2(\ell+1)}] \tag{17}$$

$$\Theta_{\ell m} = \pi(\ell+1) + 2M\omega\Big[2\log(4M\omega) - \frac{(\ell-1)(\ell+3)}{\ell(\ell+1)}\Big] - 2M\omega\Big[H_\ell + H_{\ell-1} - 2\gamma\Big] + \mathcal{O}(M\omega)^2 \tag{18}$$

The authors of [10] employ two different methods to compute these reflectivities. Using the `Black Hole Perturbation Toolkit` implementation of the Mano-Suzuki-Takasugi (MST) method [30, 5], they are able to accurately compute these reflectivities for dimensionless frequencies $\omega M \in [0.1, 14]$ up to mode $\ell = 70$, for which some are in figure 5.

Now we have described how a non-rotating black hole responds to an incoming gravitational perturbation. In particular, we quantify this response at the boundary - infinity - which is, in lensing terminology, where the observer is located with respect to the lens. Although the language is different, black hole perturbation theory ultimately describes lensing in strong gravity. Therefore, these reflectivities will be vital to construct an actual **scattered waveform** that we can observe, which is done in section 3.2.

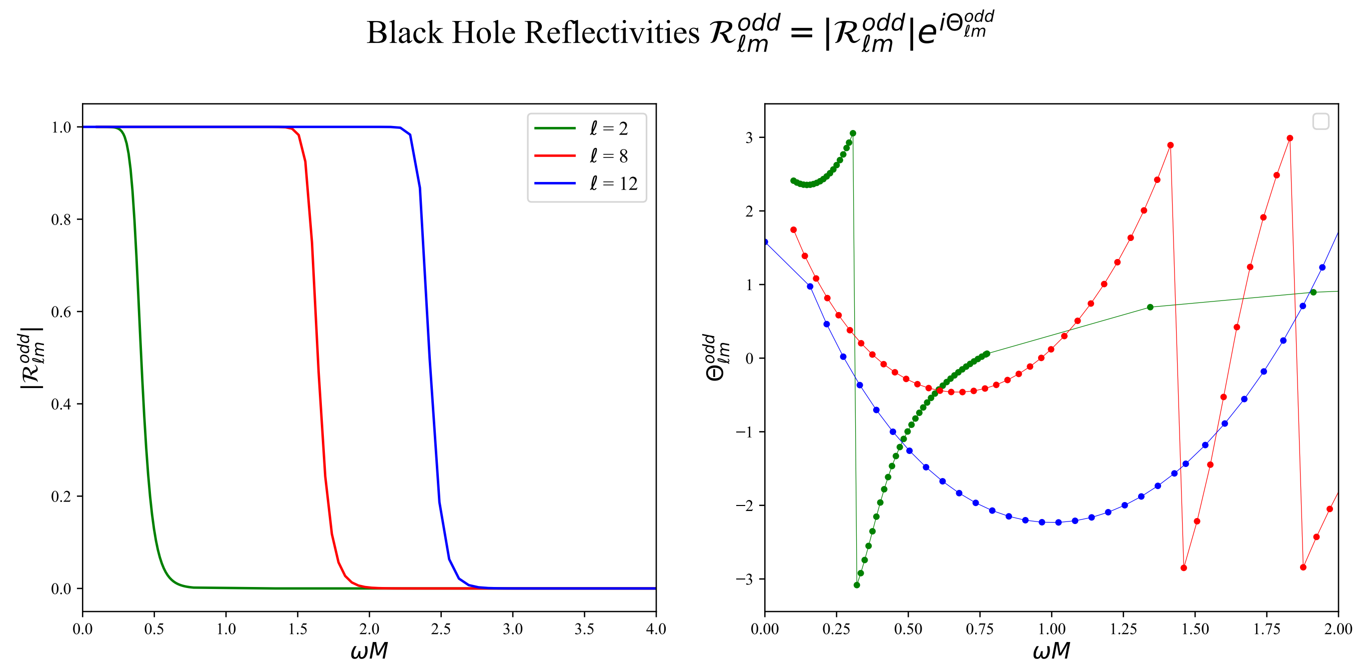

Figure 5: Reflectivity of the BH for three different ℓ modes - odd parity sector. Obtained using the `Black Hole Perturbation Toolkit` by the authors of [10].

2 Weak gravity lensing

One of the most common simplifications to Eq.(9) is to assume our metric is only slightly curved by a Newtonian potential, such that it is a small perturbation around Minkowski metric, given by [5]:

$$ds^2 = -(1+2\Phi)dt^2 + (1-2\Phi)d\vec{r}^2, \tag{19}$$

which we can see right away resembles the Schwarzschild metric for a small enough $\Phi = -M/r$. A good physical understand of this is to think of it as an approximation of Schwarzschild metric if we are standing far away from the source of the potential so that the ratio $\frac{R_s}{r} \ll 1$. Alternatively, we can assume the source of our deviation from flat metric to be a not very compact object, and its radial extent being a lot larger than the Schwarzschild radius - this means we can get arbitrarily close to the object but the weak gravity approximation is still valid. If so, we can expand the term $\left(1 - \frac{R_s}{r}\right)^{-1}$ as $(1 + \frac{R_s}{r})$, such that our metric simplifies to Eq.(19). The source of our potential is both spherically symmetric and static, which means that any partial derivatives of Φ with respect to t, θ, ϕ can be neglected.

It is understood that the source of the weak gravitational potential is the lens itself. If so, this approximation only applies to certain physical systems (for example, a galaxy or galaxy cluster acting as a lens, since they are not very compact objects; or a black hole if the observer is located sufficiently far from it). In reality, this is valid for the majority of lensing systems throughout the cosmos. However, there are some cases in which it breaks down, which are the object of interest of section 3.

[5]For this section, we will work in natural units, where $G = c = 1$.

2.1 Wave optics

Knowing what our background metric looks like, one is able to solve how a gravitational perturbation propagates in such a space-time through Eq.(9). Given that our metric is only slightly curved, the second term is subdominant compared to the first one, which means we can, to a good approximation, ignore it. This statement can be justified considering this back of the envelope derivation:

$$\Gamma \sim \mathcal{O}(\partial g^{(B)}) \sim \mathcal{R}^{-1}, \tag{20}$$

with $\mathcal{R}$ the scale of the curvature and Γ the Christoffel symbol.

$$\Rightarrow \Box h_{\mu\nu} \sim (\partial + \Gamma)^2 h \sim \mathcal{O}(\partial^2 h) + \mathcal{O}(\mathcal{R}^{-2} h); \tag{21}$$

$$R_{\mu\alpha\nu\beta} h^{\alpha\beta} \sim (\partial\Gamma + \Gamma^2) h \sim (\partial^2 g^{(B)} + (\partial^2 g^{(B)})^2) h \sim \mathcal{O}(\mathcal{R}^{-2} h) + \mathcal{O}(\mathcal{R}^{-4} h). \tag{22}$$

Doing some rough scale comparisons, we can see that for a small curvature scale, the coupling of the curvature to the gravitational perturbation (encoded in the second term of Eq.(9)) has little influence on the propagation.[6] Therefore, we will focus on solving

$$\Box h_{\mu\nu} = 0, \tag{23}$$

for the metric given in Eq.(19) (although we dropped the notation, $h_{\mu\nu}$ refers to the trace reversed metric perturbation introduced in section 1.2).

The other important approximation that is made is that the changes in the polarization content of the wave can be neglected in weak gravity to a very good approximation. If we divide our perturbation into a scalar amplitude h_A and some tensor with polarization content $\epsilon_{\mu\nu}$, then:

$$\Box h_{\mu\nu} = (\Box h_A)\epsilon_{\mu\nu} + 2 D_\alpha h_A D^\alpha \epsilon_{\mu\nu} + h_A \Box \epsilon_{\mu\nu} \tag{24}$$

(the cross term is $\sim \mathcal{O}(\Gamma^2)$, so it's negligible)

$$\Rightarrow \Box h_A = 0 \tag{25}$$

The advantage of this assumption is that our tensorial gravitational perturbation is now a scalar, which makes the problem considerably more tractable, since we are now solving a **scalar wave equation**.

$$\Box h_A = \frac{1}{\sqrt{-g}} \partial_\mu \left(\sqrt{-g} g^{\mu\nu} \partial_\nu h_A \right) = 0 \tag{26}$$

(see appendix B for the intermediate steps)

$$\Leftrightarrow \nabla^2 h_A - (1 - 4\Phi) \partial_t^2 h_A = 0 \tag{27}$$

Now that we have a slightly modified version of the scalar wave equation for a flat space-time, we can move it to Fourier space using the inverse Fourier transform of h_A given by $\int d\omega \tilde{h}_A e^{-i\omega t}$. This will turn our time-domain Eq.(27) into

$$(\nabla^2 + \omega^2) \tilde{h}_A(\omega, \vec{r}) = 4\Phi\omega^2 \tilde{h}_A(\omega, \vec{r}). \tag{28}$$

[6] Notice how this is valid for any wavelength. It is common to use the short wave approximation, in which $\lambda/\mathcal{R} \ll 1$ (the scale over which the scale of our perturbation varies is approximately the wavelength: $\partial h \sim \lambda$). We will explore this in detail later on, but for now, no statement is made about the size of our wave, only the background metric.

Since we are analyzing what happens to a GW due to the presence of a lens, it is useful to introduce the **amplification factor** $F(\omega, \vec{r})$ which describes how our original wave is amplified. This factor is given as the ratio of the amplified wave $\tilde{h}_A(\omega, \vec{r})$ and an unlensed spherical wave, with an ansatz $\tilde{h}_{A,0}(\omega, \vec{r}) = e^{i\omega r}/r$ ($h_{A,0}$ is simply the solution of our wave equation in the absence of a potential Φ). After a long but rather trivial computation in which all that is done is plug into the previous equation $\tilde{h}_A(\omega, \vec{r}) = F(\omega, \vec{r})\frac{e^{i\omega r}}{r}$ and compute the derivatives in order to cancel out all the exponentials, one arrives at a partial differencial equation for the amplification factor:

$$\partial_r^2 F + \nabla_{\theta,\phi}^2 F + 2i\omega\partial_r F = 4\Phi\omega^2 F, \tag{29}$$

where $\nabla_{\theta,\phi}^2$ is the angular part of the Laplacian operator in spherical coordinates (the Laplacian operator of the 2D sphere).

The weak gravity approximation is valid as long as the source, lens and observer are at large enough distances that the potential that deforms our metric is rather weak. In astrophysics, this essentially means that the distances source-lens and lens-observer are cosmological. Under this framework, if we place the source at the origin of the spherical coordinates and the observer at $\vec{r}_0 = (r_0, \theta_0, \phi_0)$, it is safe to assume that the waves reaching the observer will be confined to the region where $\theta_0 \ll 1$ - see figure 6 for a better visualization. This allows us to approximate use the small angle approximation on θ. Furthermore, one can also employ the approximation that the typical scale over which the amplification factor changes is a lot smaller than the typical scale over which the amplitude of the wave changes. This translates to $|\partial_r^2 F| \ll |\omega\partial_r F| \equiv \omega/|\partial_r \ln F| \gg 1$, which allows us to obtain a Schrödinger-like equation for the amplification factor:

$$i\partial_r F = -\frac{1}{2\omega}\partial_{\vec{\theta}}^2 F + 2\omega\Phi F, \quad \text{where } \partial_{\vec{\theta}}^2 = \frac{1}{r^2}\left(\partial_\theta^2 + \frac{\partial_\theta}{\theta} + \frac{\partial_\phi^2}{\theta^2}\right). \tag{30}$$

The reason we can write the angular component of the Laplacian operator as such is because, when assuming small θ as well as prescribing a hierarchy between the length scale associated to the GW (ω) and the lens ($\partial_r \ln F$), we introduce the **paraxial approximation** which allows us to separate the radial and angular component of our system, and consider the vector $\vec{\theta} = (\theta, \phi)$ as a two dimensional vector on a flat plane.

This equation resembles Schrödinger's wave equation in the sense that the time coordinate is the radial coordinate r in this case; the mass of the particle is the frequency of the wave; and the "time" dependent potential of Schrödinger's equation is actually Φ (consistent with the fact that our "time" coordinate is r). The same way it is done when solving Schrödinger's equation, we can employ the **path integral formulation**- [17, 8] [7] to obtain an integral expression for the amplification factor:

$$\mathcal{L}(r, \theta, \dot{\vec{\theta}}) = \omega\left[\frac{1}{2}r^2|\dot{\vec{\theta}}|^2 - 2\Phi\right], \text{where } \dot{\vec{\theta}} = \frac{d\vec{\theta}}{dr}, \text{ leading to} \tag{31}$$

$$F(\vec{r_0}) = \int \mathcal{D}\vec{\theta}(r) exp\left\{i\int_0^{r_0} dr\mathcal{L}(r, \vec{\theta}(r), \dot{\vec{\theta}}(r))\right\}. \tag{32}$$

The way this is equivalent to the path integral formulation is: if we start by choosing a particular path $\vec{\theta}(r)$ that connects the source to the observer and then integrate over the Lagrangian corresponding to that path, we get the phase accumulated by the wave on that path. The second integral encapsulating this essentially just means that we will sum over all the possible paths to get the phase contribution from each of the paths to the total amplitude - e^{iS} , where S is the action. The same way quantum mechanics approaches the classical limit of extremizing the action along one path when

[7] Short explanation of the path integral formulation: In classical mechanics, a particle will follow the path that extremizes the action $S = \int dtL$. Once one employs this coniditon given the lagrangian of the system, one obtains the classical Euler-Lagrange equations of motion for that particular path. However, in quantum mechanics, it is argued that all the paths contribute to the motion of the particle going from A to B.

$\hbar \to 0$, we reach the **geometric optics limit** when $1/\omega \to 0$. This means that the wave will travel along one path - ray and not display interference and diffraction effects as it does at lower frequencies. Essentially, in the **wave optics regime**, we sum over all possible paths - bottom right corner of figure 4 - , while in geometric optics we only consider the ones that extremize the action.

One can further simplify this integral expression by means of the **thin lens approximation** , namely that the lens' extension in the direction of propagation (r) is small compared to the one on the plane orthogonal to it. This translates to approximating the potential , $\int dr \Phi(r, \vec{\theta}) = \frac{1}{2}\delta(r - r_L)\psi(\vec{\theta}_L)$ - essentially, we have been able to separate the radial and angular $\vec{\theta} = (\theta, \phi)$ evolution of our system, which turns the integral along the path $\mathcal{D}\theta(\vec{r})$ into an integral evaluated at r_L over the plane $\vec{\theta}_L$, as such:

$$F(\vec{r_0}) = \frac{\omega}{2\pi i} \frac{r_L r_0}{r_{L0}} \int d^2\vec{\theta}_L \exp\left[i\omega\left(\frac{r_L r_0}{2r_{L0}}|\vec{\theta}_L - \vec{\theta}_0|^2 - \psi(\vec{\theta}_L)\right)\right] \tag{33}$$

By interchanging the roles observer-source (i.e., the observer is now in the origin of the coordinate system), as well as redefining the integral in terms of angular diameter distances and impact parameters instead of angles, one can rewrite the previous integral as (see figure 6 to visualize the quantities and distances introduced):

$$F(\vec{\eta}, \omega) = \frac{D_S}{D_L D_{LS}} \frac{\omega(1+z_L)}{2\pi i} \int_{-\infty}^{+\infty} d^2\vec{\xi} \exp\left\{i\omega(1+z_L)\left[\frac{D_L D_S}{2D_{LS}}\left(\frac{\vec{\xi}}{D_L} - \frac{\vec{\eta}}{D_S}\right) - \psi(\vec{\xi})\right]\right\} \tag{34}$$

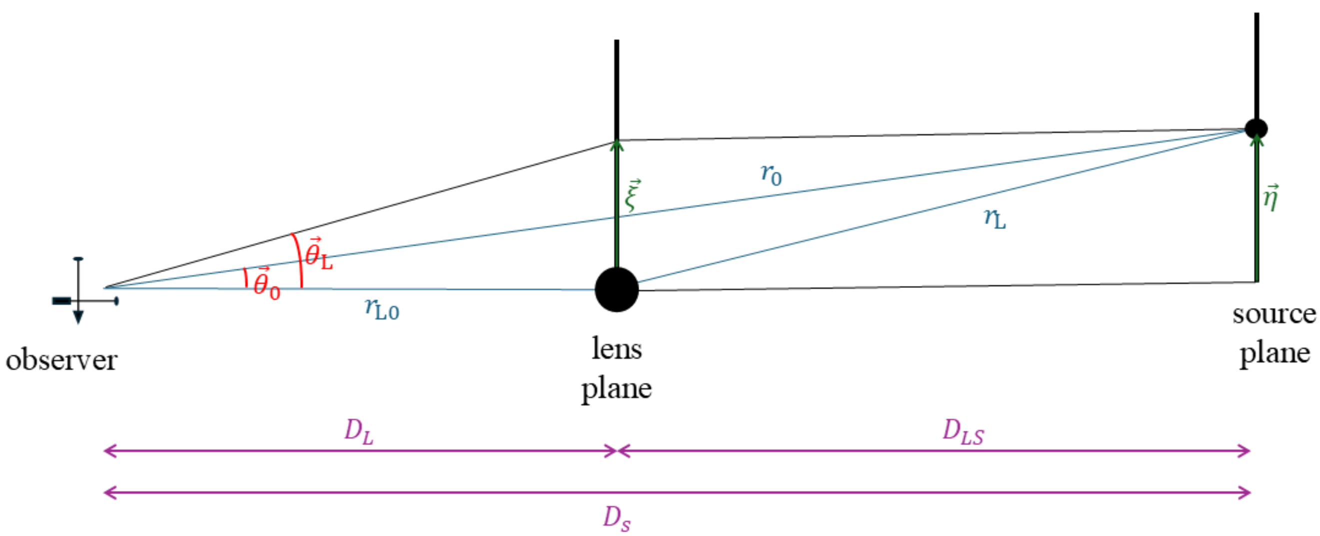

Figure 6: Setup of the physical system we are considering. Angular quantities are marked in red, radial distances are marked in blue, impact parameters are marked in green, and the angular diameter distances between planes are marked in purple. $\vec{\theta}_0 = (\theta_0, \phi_0)$ and $\vec{\theta}_L = (\theta_L, \phi_L)$ are the real and apparent angular positions of the source with respect to the observer. The impact parameters $\vec{\eta}$ and $\vec{\xi}$ are the distances of the source (in the source plane) and the paths of the wave (in the lens plane) from the line of sight. They are obtained by taking the angles $\vec{\theta}_0$ and $\vec{\theta}_L$ divided by the angular diameter distances D_S and D_L, respectively, and serve as the vector coordinates in the source and lens plane. D_{LS} is the angular diameter distance between the source and lens plane. The distances r_0, r_L and r_{L0} are radial/physical distances between source-observer, source-lens and observer-lens, respectively. Keep in mind that, initially, when the radial coordinates are defined, the source is at the origin.

Essentially, we define the lens/image plane with coordinates $\vec{\xi} = \{\xi_1, \xi_2\}$. We replace $\vec{\theta}_L$ with the impact parameter $\vec{\xi}$ - this is just the apparent position of the source in the lens plane, which is, as will be introduced later on, "the image".

In the absence of a potential, the waves would just take the most direct path connecting the source and the observer but, since there is, they cross the lens plane at the position $\vec{\xi}$. The line of sight is defined as the line from the observer crossing the lens plane at the origin, and the source plane is defined perpendicular to this line, with the source being placed at the coordinates $\vec{\eta}$ in the source plane. The distances D_L, D_S and D_{LS} are simply angular diameter distances connecting the planes observer-lens, observer-source and lens-source, respectively. Furthermore, since these distances are cosmological, it is important to account for the influence of cosmological propagation from the lens plane until they reach the observer, which is why we multiply ω by the factor $(1 + z_L)$. One can even take the simplification one step further and rewrite our integral using the dimensionless quantities:

$$\vec{x} = \frac{\vec{\xi}}{\xi_0} \quad , \quad \vec{y} = \frac{\vec{\eta}}{\xi_0}\frac{D_L}{D_S} \quad , \quad \hat{\psi}(\vec{x}) = \frac{D_L D_{LS}}{D_S \xi_0^2}\psi(\vec{x}\xi_0) \quad \text{and} \quad \varpi = \omega(1+z_L)\frac{\xi_0^2 D_S}{D_L D_{LS}}; \tag{35}$$

for which ξ_0 is just an arbitrary normalization constant. This allows us to write the previous integral in the more simplified form:

$$F(\varpi, \vec{y}) = \frac{\varpi}{2\pi i}\int d^2\vec{x}\, \exp\left[i\varpi T_d(\vec{x}, \vec{y})\right] \tag{36}$$

where $T_d(\vec{x}, \vec{y}) = \frac{1}{2}(\vec{x} - \vec{y})^2 - \hat{\psi}(\vec{x})$ is the dimensionless time delay surface (also known as **Fermat potential**).

The first term of the time delay surface is the geometrical time delay, which is just the time delay the wave acquires from taking the longer path instead of the most direct one connecting the observer and the source. The second term - Shapiro time delay - is the influence of the potential in the propagation of the wave. The Shapiro time delay $\hat{\psi}$ is the gravitational potential of the lens projected onto the 2-D lens plane (we see that it only depends on the coordinates $\vec{x} = \{x_1, x_2\}$) and arises from the deflection potential - [38]. The choice of the normalization constant is arbitrary, however, for practical reasons, it is usually defined in terms of the Einstein angle

$$\theta_E = \sqrt{\frac{4GM}{c^2}\frac{D_{LS}}{D_L D_S}} \quad \text{as} \quad \xi_0 = D_L\theta_E. \tag{37}$$

Equation (36) is, perhaps, the most important analytical expression for lensing in weak gravity since it encapsulates the behavior of the amplification factor as a function of the dimensionless frequency and impact parameter - i.e. position of the source with respect to the observer line of sight. In theory, knowing what the lens projected potential looks like, one can solve this integral and obtain the amplification and phase shift of the wave at each frequency value. However, the problem is not that trivial and there are few lens models that allow us to obtain a clean analytical solution to this integral - sec.2.3. Nonetheless, if one reaches high enough frequency values, since we're integrating over a complex exponential, Eq.(36) becomes too oscillatory and we can no longer evaluate the integral analytically, which is where the stationary phase approximation comes in.

2.2 Geometric optics

If the dimensionless frequency ϖ in the diffraction integral is large enough when compared to the time delay surface T_d, the integrand of Eq.(36) becomes a highly oscillating function ($\varpi \gg T_d^{-1} \Rightarrow \varpi T_d \rightarrow \infty$). Under these conditions, the **stationary phase approximation** (SPA) can be employed to solve this integral - placing us in the top right corner of figure 4. We are, then, in the regime of lensing that always applies to light, and can be applied to gravitational waves in certain systems. This technique allows us to approximate the integrand as a sum of its stationary points which, in fact, are the dominant contributions to the integral. We can interpret this using Fermat's principle: this principle states that, when light travels from a source to an observer, from all of the paths connecting them, the ones that extremize the arrival time will be the ones corresponding to the actual rays - these are our **images**. Let us put this into practice:

$$\partial_{\vec{x}} T_d(\vec{x},\vec{y}) = 0 \qquad \Longleftrightarrow \qquad \partial_{\vec{x}}\left[\frac{1}{2}(\vec{x}-\vec{y})^2 - \hat{\psi}(\vec{x})\right] = 0 \Longleftrightarrow \tag{38}$$

$$\vec{y} = \vec{x} - \partial_{\vec{x}}\hat{\psi}(\vec{x}), \qquad \text{or, adding dimensions back to the problem,} \qquad \vec{\eta} = \frac{D_S}{D_L}\vec{\xi} - D_{LS}\partial_{\vec{\xi}}\psi(\vec{\xi}) \tag{39}$$

Finding the stationary points of the time delay surface leads us to the **lens equation** . For a given source position in the source plane $\vec{y} = (y_1, y_2)$ and a given deflection caused by the lens potential $\hat{\alpha}(\vec{x}) = \partial_{\vec{x}}\hat{\psi}(\vec{x})$, this equations tells us the image positions $\vec{x} = (x_1, x_2)$ in the image/lens plane. In practical terms, an image is a discrete peak in the intensity of the wave, and the position of the images in the lens plane are simply the "apparent" positions of the source (the fact that we can have multiple images means that, in some cases, we see the same source multiple times in the ski, which is exactly what we see in figure 3). The deflection angle $\vec{\alpha}$, that arises from the derivatives of the projected potential ψ, can be directly traced back to the surface density of the lens $\Sigma(\vec{\xi})$ - intuitively, one can think that if ψ is the projection of a volume density integrated on the lens plane; the derivative of ψ is just the integral of a surface density over the lens plane:

$$\hat{\alpha}(\vec{x}) = \frac{D_L D_{LS}}{\xi_0 D_s}\alpha(\vec{\xi}) = \frac{D_L D_{LS}}{\xi_0 D_s}\int_{\mathbb{R}} d^2\xi' 4\Sigma(\vec{\xi'})\frac{\vec{\xi}-\vec{\xi'}}{|\vec{\xi}-\vec{\xi'}|^2}. \tag{40}$$

This means that for a given surface density of a lens, we can get a projected lens potential $\psi(\vec{\xi})$ quite easily, and then predict the image positions by use of the lens equation Eq.(39). However, very often happens that, for a single source position a single potential can, at small impact parameters, create multiple images. This is called **strong lensing**, as opposed to when we have a ray propagating that gets deflected at a relatively small angle, which is **weak lensing** - a schematic representation can be seen in figure 4 [8]. Ultimately, the more massive the potential is, the higher the image multiplicity. This means that, theoretically, knowing all the image positions and the lens potential, one can trivially map the source plane and infer the source position. However, the opposite is not necessarily true: if, for a given potential and source position, multiple images can be created, further constraints are needed in order to infer the positions of all of the solutions to the lens equation ($\vec{x}$- the image positions).

It is established that lensing is not only the deflection of the propagation of the wave but also its amplification. To get the **image magnifications**, we preform a Taylor expansion fo the time delay surface around each of its stationary points - the images will have coordinates $\vec{x_j} = (x_{1,j}, x_{2,j})$.

$$T_d(\vec{x},\vec{y}) = T_j + \sum_{a,b}\frac{1}{2}\partial_b\partial_a(T_d)_j(x_a - x_{a,j})(x_b - x_{b,j}) + \sum_{a,b,c}\frac{1}{3!}\partial_c\partial_b\partial_a(T_d)_j(x_a - x_{a,j})(x_b - x_{b,j})(x_c - c_{c,j}) \tag{41}$$

$$+ \sum_{a,b,c,d}\frac{1}{4!}\partial_d\partial_c\partial_b\partial_a(T_d)_j(x_a - x_{a,j})(x_b - x_{b,j})(x_c - c_{c,j})(x_d - x_{d,j}) + \mathcal{O}(\tilde{x}^5)... \tag{42}$$

T_d is a 2-D surface, which means the indices $\{a,b,c,d\}$ can only take the values $\{1,2\}$ (we can only be deriving with respect to x_1 or x_2). It is a good enough approximation to neglect third and higher order terms such that the only remaining terms of our expansion are the arrival time of the image T_j and the sum of the second order derivatives evaluated at the image positions $\vec{x_j}$. We can always perform a rotation on the coordinates (x_1, x_2) such that the Hessian matrix (2×2

[8] Strong lensing $\neq$ strong field lensing!! Strong lensing refers to the image multiplicity; strong field lensing happens for a strong gravitational field.

matrix with the second order derivatives of the Fermat potential) is diagonal and the diffraction integral - Eq.(36) becomes:

$$F(\varpi, \vec{y}) = \frac{\varpi}{2\pi i} \int d^2\vec{x} \exp\left[i\varpi T_d(\vec{x}, \vec{y})\right] = \frac{\varpi}{2\pi i} \sum_j exp(i\varpi T_j) \int d^2\vec{x}' exp\left[i\frac{\varpi}{2}\left((\partial^2_{x'_1} T_d)_j x'^2_1 + (\partial^2_{x'_2} T_d)_j x'^2_2\right)\right], \quad (43)$$

where the second order derivatives computed at the image positions $\lambda_{1,2} \equiv (\partial^2_{x'_{1,2}} T_d)_j$ are the diagonal components of the Hessian matrix and $\{x'_1, x'_2\}$ are the coordinates in which the matrix is diagonal. As such, each of the integrals becomes a gaussian integral:

$$F(\varpi, \vec{y}) = \frac{\varpi}{2\pi i} \sum_j exp(i\varpi T_j) \iint_{-\infty}^{\infty} exp\left(\frac{i\varpi\lambda_1}{2}(x'_1)^2\right) exp\left(\frac{i\varpi\lambda_2}{2}(x'_2)^2\right) dx'_1 dx'_2 \Leftrightarrow \quad (44)$$

$$F(\varpi, \vec{y}) = \frac{\varpi}{2\pi i} \sum_j exp(i\varpi T_j) \sqrt{\frac{2\pi}{-i\varpi\lambda_1}} \sqrt{\frac{2\pi}{-i\varpi\lambda_2}} = \sum_j exp(i\varpi T_j) \frac{1}{\sqrt{\lambda_1}\sqrt{\lambda_2}}. \quad (45)$$

However, to ensure that this integral is physical ($Re\{a\} < 0$), we need to keep in mind that the eigenvalues of the Hessian matrix can be positive or negative, depending on the kind of stationary point the image is. If both the eigenvalues of the Hessian matrix computed at the stationary point j are positive, we are in the presence of a minimum; if they are both negative, it's a maximum and if one of them is positive and the other is negative we are in the presence of a saddle point. We have reduced our complex exponential integral to a discrete sum of complex exponentials, each representing an image, scaled by a $\sqrt{\lambda_1}\sqrt{\lambda_2} = \mu_j^{-1/2}$ factor. This factor is the **magnification of that particular image** and, depending on the type of stationary point (or, in other words, **parity** of the image), it can be:

- $|\mu_j|^{1/2}$ if it's a minimum , or **type I** image;
- $-|\mu_j|^{1/2}$ if it's a maximum, or **type II** image;
- $i|\mu_j|^{-1/2}$ if it's a saddle point, or **type III** image.

An alternative method to account for the parity of the image is to introduce the **Morse phase**, which is an index n_j that can take values $0, 1/2, 1$ depending on whether the image is a type I, type II or type III image, respectively. Altogether, this yields the following expression for the amplification function under the geometric optics approximation:

$$F(\varpi, \vec{y}) = \sum_j |\mu_j|^{1/2} exp[i\varpi T_j(\vec{y}) - i\pi n_j]. \quad (46)$$

The physical interpretation behind the parity of the images is exactly what the morse phase shift entails: either the images are multiplied by a -1 factor, meaning they are inverted; or they are multiplied by a $+1$ factor and they are "normal" (or the magnification just amplified them); or they are multiplied by a $-i$ factor and they are both inverted and have a π phase shift - see figure 7 for a simplifying visual representation of this.

We have successfully simplified a not so trivial integral expression into a discrete sum of image magnifications and image positions via use of the SPA. Both of these quantities can be obtained simply by knowing the source position and the lens projected potential by use of the lens equation - Eq.(39). To see what this translates to, this approximation is employed to well-known lens models and compared with the full analytical solution obtained from Eq.(36)- section 2.3.

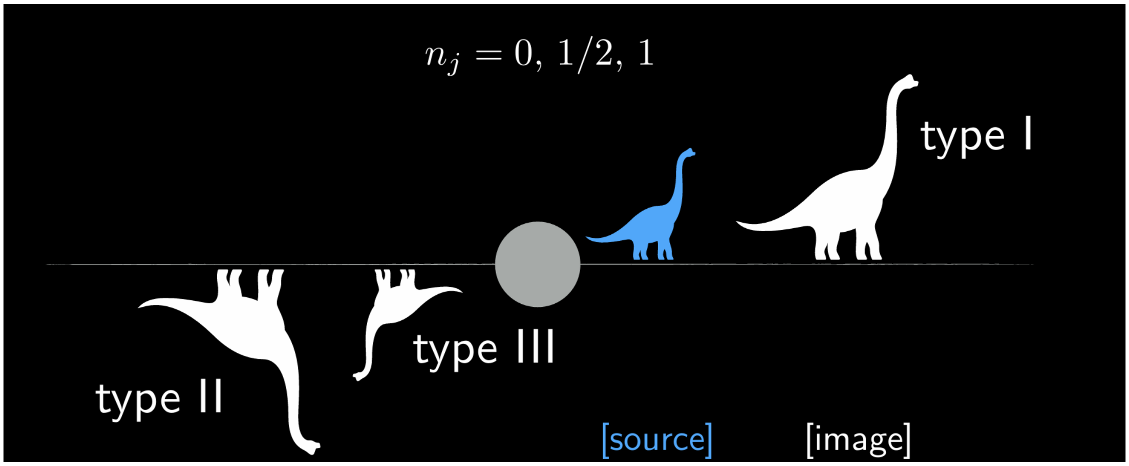

Figure 7: Simplifying visual representation of the classification of gravitational lensing images. Image is adapted from a talk by Professor Jose Maria Ezquiaga, ”Gravitational Wave Lensing: Current Searches and Future Prospects” at the workshop ”Lensing and Wave Optics in Strong Gravity” hosted at the Erwin Schrödinger Institute, 2024.

2.2.1 Beyond geometric optics

Even though the SPA allows us to significantly simplify the problem, it has some limitations. There are two possible scenarios in which the geometric optics approximation breaks down:

- if the integrand of Eq.(36) is not oscillatory enough, i.e. $\varpi \gg T_d^{-1}$ no longer holds;
- if the determinant of the Hessian matrix of the time delay surface is zero, causing formally "infinite magnifications": $\mu_j^{-1} = \lambda_1 \lambda_2 = 0$. This happens for regions in the lens plane which are called **caustics**.

If the first is true, which would place us in the **wave optics regime**, one would assume that the only viable solution would be to solve the diffraction integral numerically or analytically - section 2.3. However, for very small frequencies, we find ourselves in the **deep wave optics regime**, in which the scale of the wave is significantly longer than the size of the lens. In this case, the wave travels unaffected by the lens potential, and $|F| \sim 1$. On the other hand, for the regime where the wave is much shorter than the scale of the lens, the SPA is expected to perfectly converge with the analytical solution to the diffraction integral. However, if the frequency is somewhere between these two regimes, **it is relevant to evaluate wether there is an alternative to solving the diffraction integral in full, which becomes rather complicated for complex lens models.**

When Taylor expanding the time delay surface around its image positions, as done in Eq.(42), we previously neglected any term of order higher than the second order derivatives. However, if we truncate our series at a slightly higher order terms, we can better evaluate the integrand of Eq.(36) as a polynomial in ϖ. If we include third and fourth orders in the expansion, the amplification factor written as a sum of the discrete images, turns into:

$$F(\varpi, \vec{y}) = \frac{1}{2\pi i} \sum_j \int d^2\vec{z} \exp\left[i \left(\varpi T_j + \frac{1}{2} \partial_b \partial_a (T_d)_j \tilde{z}_a \tilde{z}_b \right) \right] \times$$
$$\exp\left[i \left(\frac{1}{6\sqrt{\varpi}} \partial_c \partial_b \partial_a (T_d)_j \tilde{z}_a \tilde{z}_b \tilde{z}_c + \frac{1}{24\Omega} \partial_d \partial_c \partial_b \partial_a (T_d)_j \tilde{z}_a \tilde{z}_b \tilde{z}_c \tilde{z}_d \right) \right], \tag{47}$$

where $\vec{z}$ is simply the result of a coordinate change $\vec{z} = \sqrt{\varpi}\vec{x}$, and we introduce $\tilde{z}_a = z_a - z_{a,j}$ for notation reasons (remember that $\{a, b, c, d\} = \{1, 2\}$). We are left with the product of two exponentials, the first one being the very familiar one that yields a gaussian integral, leaving us with Eq.(46); and the second one will be how the corrections to the magnifications arise, specifically, by expanding this second exponential in its power series. It is important to remember that, even though we are computing "beyond geometric optics" corrections, **we are still within the validity of the stationary phase approximation**, meaning that the frequency is still rather large, allowing for discrete images to form. Therefore, within this expansion, we only account for terms up to order $1/\varpi$. This will lead to only three terms of the expansion actually contributing:

- a term of order $\varpi^{-1/2}$, which is from third order derivatives of the time delay surface;
- a term of order ϖ^{-1} - one proportional to the fourth order derivatives of the time delay surface;
- another term of order ϖ^{-1}, proportional to the third order derivatives squared.

All the other terms are of order $\varpi^{-3/2}$ or lower, rendering them basically negligible. However, the term proportional to $1/\sqrt{\varpi}$ leads to an odd integrand, which vanishes (remember we are integrating along the whole lens plane, which, for an odd function $f(x) = -f(-x)$, gives zero $\int_{-\infty}^{\infty} x^{2n+1} e^{-x^2} dx = 0$). This leaves us with only two terms, both proportional to $1/\varpi$. Explicitly, our diffraction integral now becomes:

$$F(\varpi, y) = \frac{1}{2\pi i} \sum_j exp[i\varpi T_j] \int d^2\vec{z} exp\left[\frac{1}{2}\partial_b\partial_a(T_d)_j \tilde{z}_a\tilde{z}_b\right] \times$$
$$\left[1 + \frac{i}{\Omega}\left(\frac{1}{24}\partial_d\partial_c\partial_b\partial_a(T_d)_j\tilde{z}_a\tilde{z}_b\tilde{z}_c\tilde{z}_d + \frac{i}{72}\left(\partial_c\partial_b\partial_a(T_d)_j\tilde{z}_a\tilde{z}_b\tilde{z}_c\right)^2\right)\right]. \tag{48}$$

Each integrand is no longer a gaussian one but simply a variation, of the form $\int_{-\infty}^{\infty} x^{2n} e^{-\alpha x^2} = \sqrt{\pi}(-1)^n \frac{\partial^n}{\partial\alpha^n}\alpha^{-1/2}$.

In theory, this will allow us to approach lower frequencies where we would need to, otherwise, compute the amplification factor analytically. We will see later on, for some simple lens models, how well these corrections work. The tricky and uncharted part is to see how well it works for complicated lens models, which is left for future work. So far, we have not assumed anything about the projected potential of the lens, which means that, although we have a somewhat "trivial" analytical expression for the diffraction integral, this quickly translates to very complicated expressions if $\psi(\vec{x})$ has no kind of symmetry.

2.3 Common lens models

As introduced earlier, one standard way to solve the diffraction integral introduced in Eq.(36) is by the use of the SPA, which becomes valid once the major contributions to the integrand are the stationary points of the time delay surface T_d. However, there are some simple lens models that provide us with an analytical solution, which is quite useful in the cases in which the geometric optics approximation breaks down. As mentioned earlier, this could be either if the source is located in the vicinity of a caustic or if, on the the other hand, the integrand of Eq.(36) is not highly oscillatory, i.e., if the major contributions are not solely from the stationary points of T_d, which puts us in the **wave optics regime** - bottom right corner of the plot 4.

2.3.1 Axially symmetric lenses

If the our lens has a circularly symmetric mass density, or projected potential, then $\psi(\vec{x}) \equiv \psi(x)$; which means that the mass distribution on the lens plane has only a radial dependence (we assume that the origin of the coordinates $\vec{x}$ is also the center of the lens) [9]. This will allow both our diffraction integral to take a much simpler form, and our (previously

[9] Important to note that axially symmetric around $\vec{x}$ does not mean we have a spherically symmetric lens. For example, a cylinder-like lens will be axially symmetric but not spherically symmetric - see section 8.1 of [38].

vectorial) lens equation to turn into a scalar one. To see exactly how, we can start from differentiating the Fermat potential T_d with respect to $\vec{x}$, which is how the lens equation is obtained:

$$\partial_{\vec{x}} T_d(\vec{x}, \vec{y}) = \partial_{\vec{x}} \left(\frac{1}{2}(\vec{x}^2 - 2\vec{x}\vec{y} - \vec{y}^2) - \psi(x) \right) = 0 \quad \Longleftrightarrow \quad \vec{x} - \vec{y} - \frac{\vec{x}}{x}\partial_x \psi = 0. \tag{49}$$

If $\vec{x} = x\vec{x_1}$ for example, then the whole lens equation is along the $\vec{x}_1$ direction. It is also quite intuitive if one thinks of the deflection angle itself: if the lens has a circularly symmetric distribution on the lens plane, which is what causes the rays to be deflected, than they should only be deflected along one direction. See figure 8 for a visual representation.

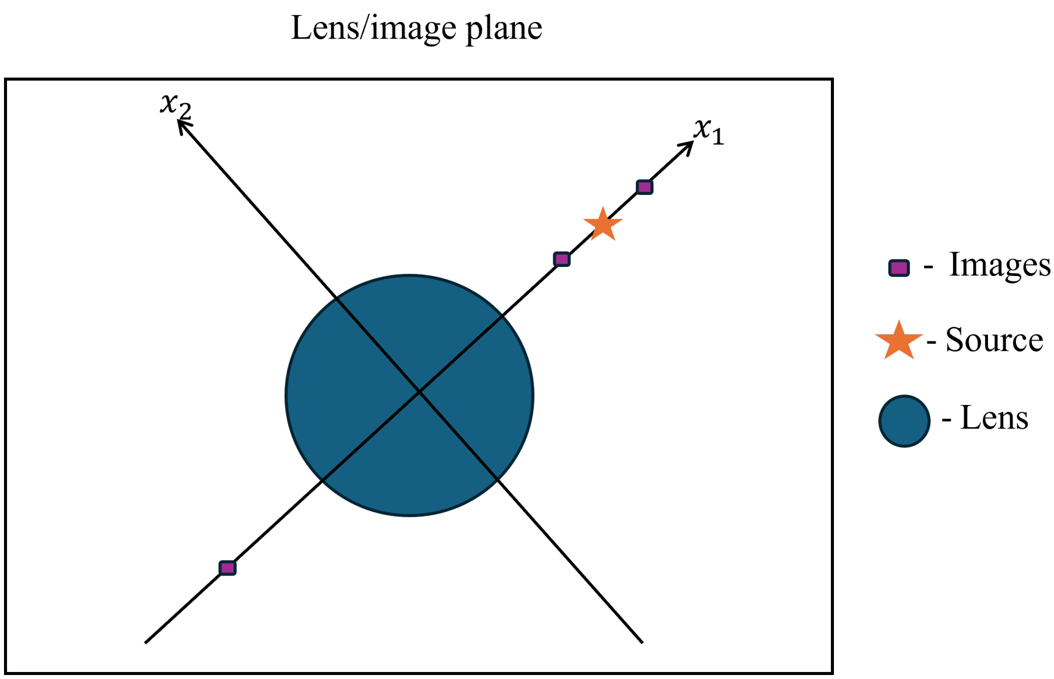

Figure 8: Schematic representation of an axially symmetric lens - one can see that the image and source positions are all along one axis, defined as the one connecting the center of the lens with the source position $\vec{y}$.

This also means that the image positions are $\vec{x}_j = x_j \vec{x}_1$, causing the magnifications to be:

$$\mu_j = \det[(\partial_a \partial_b T_d)_j] = \det[(\partial y/\partial x)_j] = \left(1 - \frac{d\psi}{dx}\bigg|_j \frac{1}{x_j}\right)\left(1 - \frac{d^2\psi}{dx^2}\bigg|_j\right) \tag{50}$$

$$\text{(or, in terms of the deflection angle } \alpha) \quad = \left(1 - \frac{\alpha(x_j)}{x_j}\right)\left(1 - \frac{d\alpha}{dx}\bigg|_j\right). \tag{51}$$

For simplicity, $1 - \frac{d\psi}{dx}\big|_j \frac{1}{x_j} = 2a_j$ and $1 - \frac{d^2\psi}{dx^2}\big|_j = 2b_j$. Finally, the corrections from higher orders of the Fermat potential, introduced in section 2.2.1 turn the amplification factor into the compact form:

$$F(\varpi, y) = \sum_j |\mu_j|^{1/2} \left(1 + \frac{i\Delta_J}{\varpi}\right) \exp[i\varpi T_j - i\pi n_J], \quad \text{where} \tag{52}$$

$$\Delta_J = \frac{1}{16}\left[\frac{1}{2a_j^2}\psi_j^{(4)} + \frac{5}{12a_j^3}\left(\psi_j^{(3)}\right)^2 + \frac{1}{x_j a_j^2}\psi^{(3)} + \frac{a_j - b_j}{a_j b_j x_j^2}\right], \tag{53}$$

and introducing $\psi^{(\alpha)} = \frac{d^\alpha \psi}{dx^\alpha}$ for notation reasons,

where we can single out the frequency independent image magnifications and the frequency dependent corrections introduced from considering higher orders -[41, 43].

As previously stated, the fact that we have an axially symmetric lens potential also greatly simplifies the expression for the diffraction integral, and allows us to solve it analytically for this class of lens models. For $\psi(\vec{x}) \equiv \psi(x)$, Eq.(36) takes the form:

$$F(\varpi, y) = -i\varpi \exp\left[\frac{i\varpi y^2}{2}\right] \int_0^\infty dx x J_0(\varpi x y) \exp\left[i\varpi\left(\frac{1}{2}x^2 - \psi(x) + \phi_m\right)\right], \tag{54}$$

where we introduced the constant ϕ_m in the Fermat potential $T_d(x, y)$ simply so that the time delay of the first image T_1 is zero, and J_0 is the 0-th order Bessel function.

2.3.2 Point Mass Lens

The simplest and perhaps most used lens model is the **point mass lens (PML)** also known as Schwarzschild lens. It essentially describes a lens with a mass M located in the center of the lens plane - see section 8.1.2 of [38]. The surface mass density of such a lens is $\Sigma(\vec{\xi}) = M\delta^2(\xi)$ concentrated on a single point. Using the length scale ξ_0 given in terms of the Einstein angle introduced in section 2 as the normalizing constant to convert from normal coordinates to dimensionless coordinates (x) one can directly obtain the deflection angle $\alpha = \partial_x \psi = 1/x$. Knowing this we can plug the deflection angle directly into the lens equation - Eq.(39), which will take the form $y = x - 1/x$ - and solve for the image positions and their magnifications (the amplification matrix can be obtained by differentiating the time delay surface twice or the lens equation once).

$$x_{1,2} = \frac{1}{2}(y \pm \sqrt{y^2 + 4}), \quad \text{- the two image positions, and} \tag{55}$$

$$\mu_{1,2} = \frac{1}{2} \pm \frac{y^2 + 2}{2y\sqrt{y^2 + 4}} \quad \text{- the magnification of each image.} \tag{56}$$

To write the full amplification factor within the geometric optics approximation, we still need the time delay between the two images (we have the normalizing constant ϕ_m, which means the first image arrives at $t = 0$). We know that $\psi(x) = \log(x)$, either through the integration of the deflection angle with respect to x, or by use of the thin lens approximation on a gravitational potential of the kind $\Phi(r) \propto -M/r$. Now all we need to do is compute $\Delta T_{1,2}$, which will be given as the difference between the time delay surface for the PML model $T_d(x, y) = \frac{1}{2}(x - y)^2 - \psi(x) - \phi_m$ computed at the two image positions $x_{1,2}$. This will allow us to write the amplification factor, as introduced in Eq.(46):

$$F_{GO}(\varpi, y) = |\mu_1|^{1/2} + |\mu_2|^{1/2} e^{i(\varpi\Delta T_{1,2} - \frac{\pi}{2})} = |\mu_1|^{1/2} - i|\mu_2|^{1/2} e^{i\varpi\Delta T_{1,2}}; \quad \text{(GO = Geometric Optics)} \tag{57}$$

where the time delay between images is $$\Delta T_{1,2} = \frac{1}{2} y\sqrt{y^2+4} + \ln\left(\frac{\sqrt{y^2+4}+y}{\sqrt{y^2+4}-y}\right) \tag{58}$$

or, including the corrections introduced in section 2.2.1, we can get Eq.(52) for the PML model

$$F_{(GO+\Delta_J)}(\varpi, y) = \left(1 + \frac{i}{\varpi}\Delta_1\right)|\mu_1|^{1/2} + \left(1 + \frac{1}{\varpi}\Delta_2\right)|\mu_2|^{1/2} e^{i\varpi\Delta T_{1,2}}, \tag{59}$$

by computing $$\Delta_{1,2} = \frac{4x_{1,2}^2 - 1}{3(x_{1,2}^2+1)^3(x_{1,2}^2-1)}. \tag{60}$$

As mentioned earlier, these approximations for the amplification factor stem from using the SPA, which is only valid at high enough frequencies, or when the period of the wave is a lot smaller than the time delay between the two images - if this is not the case, then the two images don't arrive at discrete times and will interfere. It is also not valid when the source is located near a caustic, creating infinite magnifications for the images in the lens plane. For the current lens model, we can notice that, if $y = 0$, both μ_1 and μ_2 diverge. Essentially, **if the source is located right behind the lens with respect to the observer line of sight, both of the images are located at the radial curve $x = 1$ according to the lens equation and they will have "infinite" magnifications.** To get a physical intuition on the phenomena, we can write the image positions with dimensions by use of ξ_0 and see that the radial curve $\vec{\theta} = \theta_E$ will be, itself, an image, called the **Einstein ring**. This image, despite having a finite magnification, is expected to be very bright, which we can confirm by looking at figure 3. The phenomena observed in figure 2 is of very similar nature, but with 4 discrete images instead of a continuous one. Realistically, these two phenomena are very similar to what the Einstein ring would look like for a perfect point mass lens in the cosmos. However, **very little lenses have mass distributions which can be described by a model as the simple as the PML** or by a perfect singular isothermal sphere (SIS - introduced in the following section 2.3.3). Therefore, the resulting image positions and magnifications are slightly deviated from the ones predicted by the lens equation. There is work being done in trying to solve the lens equation and diffraction integral for more complicated lens models, such as elliptic ones, or even lenses with complex substructures, such as galaxies or galaxy clusters, in order to find lensed transients - [46, 44, 28].

Nevertheless, as stated previously, it is possible to get the analytical solution for the diffraction integral for simpler lens models, of which the PML is an example. Knowing the projected lens potential, it is possible to solve Eq.(54):

$$F(\varpi, y) = \exp\left[\frac{\pi\varpi}{4} + i\frac{\varpi}{2}\left\{\ln\left(\frac{\varpi}{2}\right) - 2\phi_m(y)\right\}\right]\Gamma\left(1 - \frac{i}{2}\varpi\right){}_1F_1\left(\frac{i}{2}\varpi, 1; \frac{i}{2}\varpi y^2\right) \tag{61}$$

where Γ is just the Gamma function, ${}_1F_1$ is the hyper-geometric function and

$$\phi_m = \frac{1}{8}\left(\sqrt{y^2+4} - y\right)^2 - \ln\left(\frac{y + \sqrt{y^2+4}}{2}\right). \tag{62}$$

Analyzing this expression further shows that even the analytical solution to the diffraction integral also presents very high amplifications as $y \to 0$, which agrees with the fact that the point $y = 0$ is, indeed, a caustic, and the images of the source in this setup will blend and form a highly magnified one. This is a very powerful result in the sense that it allows us to observe objects/sources that are much more distant than what it appears from detections, offering a window into the high-redshift universe - [15, 24].

As stated in section 2.2.1, it is worth to compare the full analytical solution to the amplification factor obtained through the SPA, with and without the next order corrections - the results are in figure 9.

Point Mass Lens, y=0.1

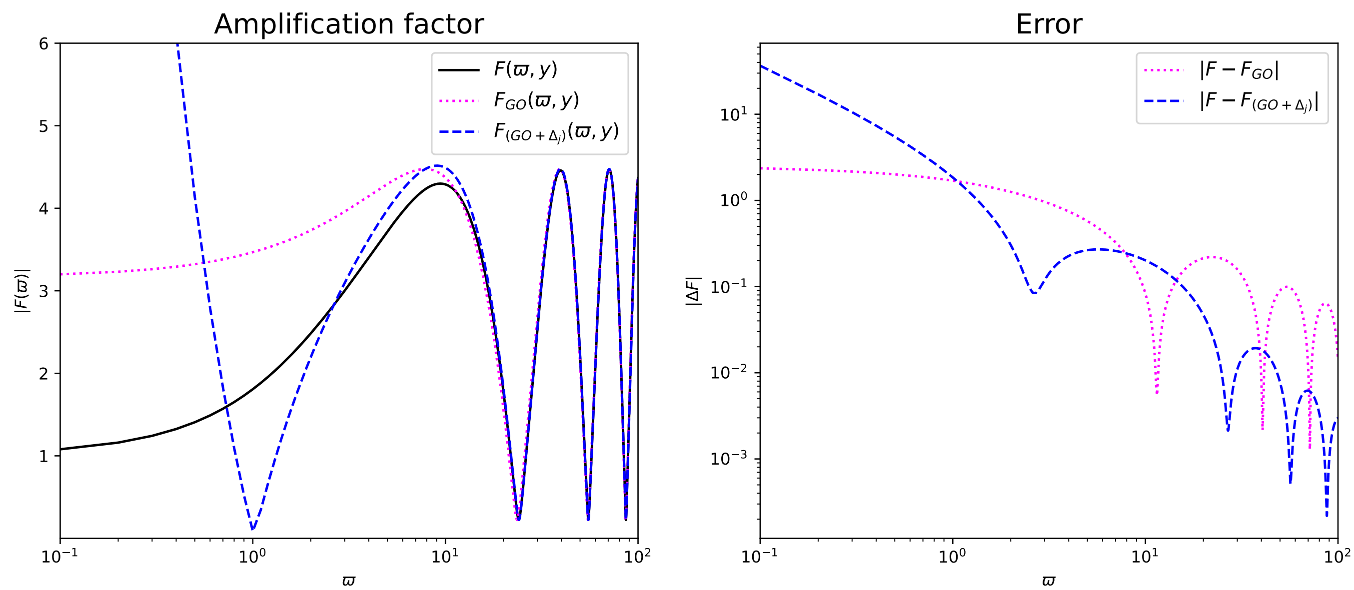

Figure 9: Comparison of the amplification factors for the point mass lens as a function of frequency obtained via equations (61) - black line; (57) - pink line; and (60) - blue line; fixed at a source position of $y = 0.1$. On the left hand side, we show the actual values of the amplification factors. On the right hand side, the error between both approximations - Eq.(57), Eq.(60) - and the analytical solution - Eq.(61).

From the **first panel** of 9, one can see that, at (dimensionless) frequencies starting at 20, the geometric optics (pink line) perfectly matches the analytical solution to the diffraction integral (black line), even without the higher order terms included (blue line), meaning that the stationary phase approximation is perfectly valid at these frequencies. However, at lower frequencies, there is a large discrepancy between the black and pink line of the plot, proof that at lower frequencies one can no longer focus only on the stationary points of the time delay surface and the amplification is better described by the full analytical solution to the diffraction integral. Furthermore, the solution represented in the blue line has a divergent behavior as $\varpi \to 0$, which is simply due to the $1/\varpi$ dependence of Eq.(60).

From the **second panel**, we draw one key conclusion: there is a range of frequencies, after the blue line has a divergent behavior (starting at $\varpi = 1$) and before the SPA describes the full solution to the diffraction integral (until $\varpi = 20$) where the inclusion of higher order terms has a much better performance in matching the analytical solution. This can be confirmed by the fact that the blue line takes a large dip bellow the pink line precisely in this frequency range. Although this may not seem like much, it proves that these extra terms play a vital role in describing the amplification for a range of frequencies which is not too low such that the wave just ignores the lens altogether and propagates unaffected - **deep wave optics** - but also not high enough for the SPA to become properly valid; and this is exactly the frequency range which cannot be covered unless there is a full analytical solution to the diffraction integral. Furthermore, the differences between the approximates and the analytical solution have a decreasing behavior with ϖ. However, the decline of the blue line is faster (overall) than the pink line. This means that, even at higher frequencies, including higher order terms from the Taylor expansion of the Fermat potential expansion yields an even more accurate representation of the full solution (the blue line is $\propto \varpi^{-2}$ and the pink line is $\propto \varpi^{-1}$).

To continue our analysis, we show in figure 10 the analytical amplification function for the point mass lens at different impact parameters (image positions).

Once again, we can see in figure 10 that in the deep wave optics regime, the amplification is almost negligible because

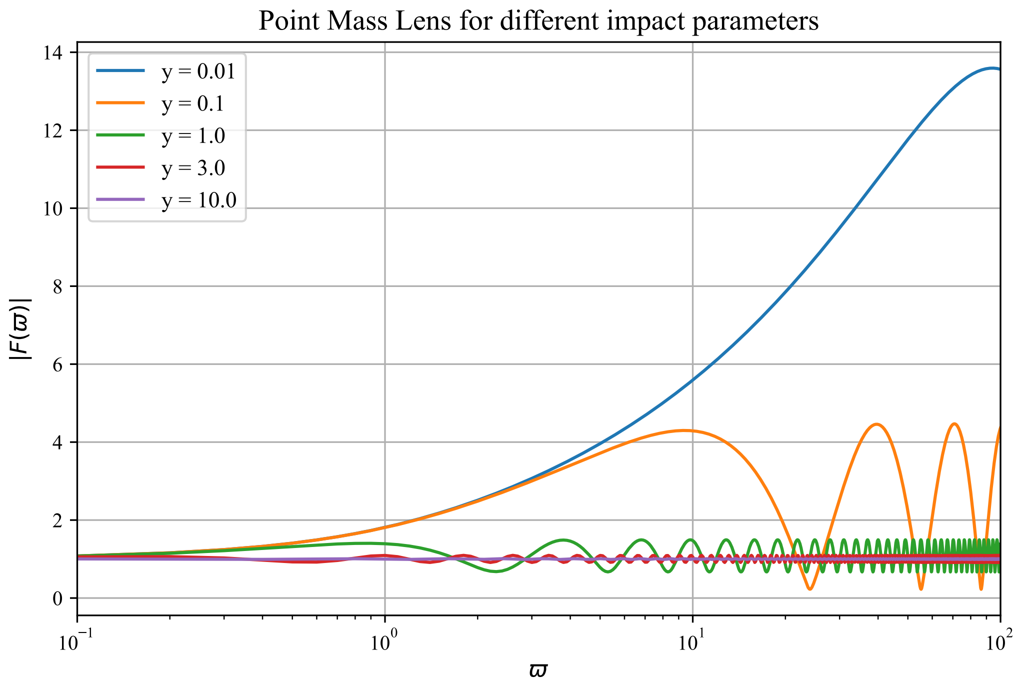

Figure 10: Amplification factor for the point mass lens model obtained through the full solution to the diffraction integral - Eq.(61), computed for different source positions y.

the wavelength is large enough such that the wave does not feel the presence of the lens. We can also see that all the amplification factors asymptotically converge to the geometric optics regime - which is identified by the oscillations in the amplification factor. These oscillations arise from the interference of both of the images that are formed. However, as we approach caustics, the position of the images becomes progressively closer, meaning they essentially merge into one very bright image, which is exactly why the lines for lower impact parameters start oscillating later on in frequency, and they reach much higher values.

2.3.3 Singular Isothermal Sphere

Another very common mass distribution used when modeling lenses in the **Singular Isothermal Sphere (SIS)**, which has a surface density of the kind $\Sigma(\vec{\xi}) = \frac{\sigma_v^2}{2}\xi^{-1}$. It is used to describe galaxies, stellar clusters and dark matter halos, for which σ_v represents the line of sight velocity dispersion. It formally has an infinite mass at $\xi = 0$, but is a very accurate representation of these kinds of matter distribution as ξ increases. There are some modifications one can do to avoid the existence of the singularity, such as considering a particular cut-off radius, but the qualitative behavior of the lens is not deeply affected by this [43].

Adopting $\xi_0 = 4\pi\sigma_v^2\frac{D_L D_{LS}}{D_S}$ as the normalizing constant, and knowing that the projected potential is $\psi(\vec{x}) = x$ (it is also a symmetric lens), one can follow the same methodology as done for the PML in section 2.3.2 and obtain the images positions, magnifications, time delay, and even an analytical solution to the diffraction integral. Solving the lens equation for this kind of potential, we find that there is a maximum of two images forming, with magnifications

$$\mu_{1,2} = \pm 1 + 1/y \quad \text{and time delay} \quad \Delta T_{1,2} = 2y. \tag{63}$$

It is immediately apparent that we only have two positive magnifications for $y < 1$, meaning that for an impact parameter $y \geq 1$, only one image forms. Therefore, the amplification factor in the geometric optics approximation has a similar shape to Eq.(57) - except for $y \geq 1$, in which case the second term disappears. Therefore, in **geometric optics**, Eq.(57) also describes the amplification function for the SIS, except we have to replace magnifications and time delays by the ones introduced in Eq.(63). Likewise, one can also compute the corrections to the amplification factor introduced in section 2.2.1. However, for a SIS model, there is one extra correction one can take into account, which stems from expanding the deflection potential around the core of the sphere - the singularity - where the density is infinite [41]. This means that the amplification factor for the SIS beyond the geometric optics limit will take the form:

$$F_{GO+\Delta_J}(\varpi, y) = \left(1 + \frac{i}{\varpi}\Delta_1\right)|\mu_1|^{1/2} + \left(1 - \frac{1}{\varpi}\Delta_2\right)|\mu_2|^{1/2} e^{i\varpi\Delta T_{1,2}} + \frac{i}{\varpi}\frac{1}{(1-y^2)^{3/2}} e^{i\varpi(y^2/2+y+1/2)}, \tag{64}$$

where $\Delta_{1,2} = \dfrac{1}{8y(1 \pm y)}$, (1 = +; 2 = -) for clarification (65)

Naturally, in the case where we don't have double images forming, the second term of Eq.(64) also vanishes. However, the third term arises from the density profile of the lens around its center, which is why the PML model does not include this correction - it has no density profile outside of the origin.

Similarly to the PML, one can obtain an analytical solution to the diffraction integral for the SIS lens model by solving Eq.(54) for a potential $\psi(x) = x$ - see [26]:

$$F(\varpi, y) = e^{\frac{i}{2}\varpi y^2} \sum_{n=0}^{\infty} \frac{\Gamma\left(1 + \frac{n}{2}\right)}{n!} (2\varpi e^{i\frac{3\pi}{2}})^{n/2} {}_1F_1\left(1 + \frac{n}{2}, 1; -\frac{i}{2}\varpi y^2\right). \tag{66}$$

It is, once again, worthwhile to compare all of these solutions, which is done in figure 11.

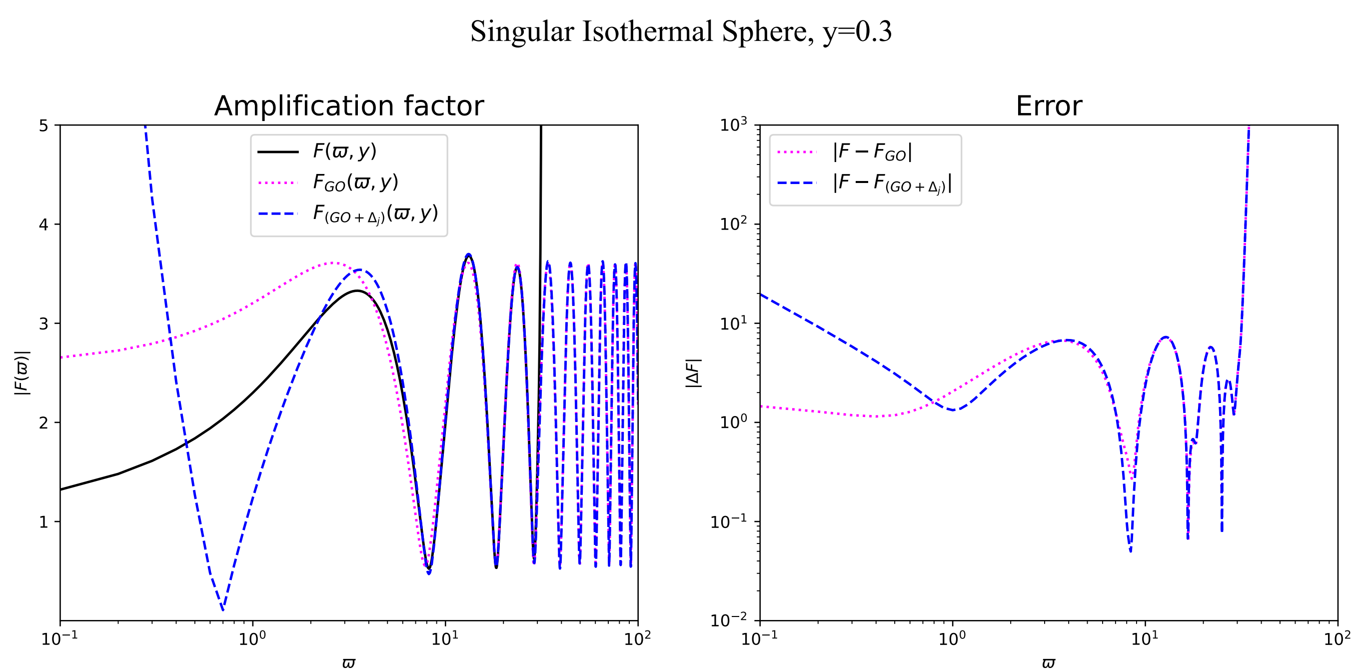

Figure 11: Comparison of the frequency dependent amplification factors of the singular isothermal sphere obtained via equations (66) - black line; (57) with the magnifications and time delays of Eq.(63) - pink line; and (64) - blue line; for a fixed source impact parameter of $y = 0.3$.

The results obtained in figure 11 are very similar to those for the PML on the **first panel** , with the single exception that the analytical solution itself diverges at high frequencies. This is caused by numerical obstacles in computing the analytical solution, due to the fact that it features an infinite sum of hyper geometric and gamma functions with a term $\varpi^{n/2}$. **Although there is an analytical solution for the singular isothermal sphere, it is not a "clean" , "well behaved" one**. This means that getting a concrete result would require more precise computational tools and efficient integration methods, since this solution very quickly diverges at high frequencies, and even faster for larger values of y. However, we can see that **the geometric optics approximation very quickly matches the analytical solution**, meaning that it is enough to describe the amplification factor in geometric optics.

For the **second panel** both of the errors diverge because of the divergence of Eq.(66), but we see that there is a very small frequency range over which the inclusion of the beyond geometric optics corrections makes a positive difference in matching with the analytical solution. However, since the validity of the computed analytical solution is, itself, dependent on more accurate computational methods, further research is needed to draw a concrete conclusion.

Similarly to the point mass lens model, figure 12 shows the existence of caustics (blue line), and interference between the two images that are forming (oscillations in the green line). However, these oscillations are visible only because we are at $y \leq 1$, since otherwise only one image would form.

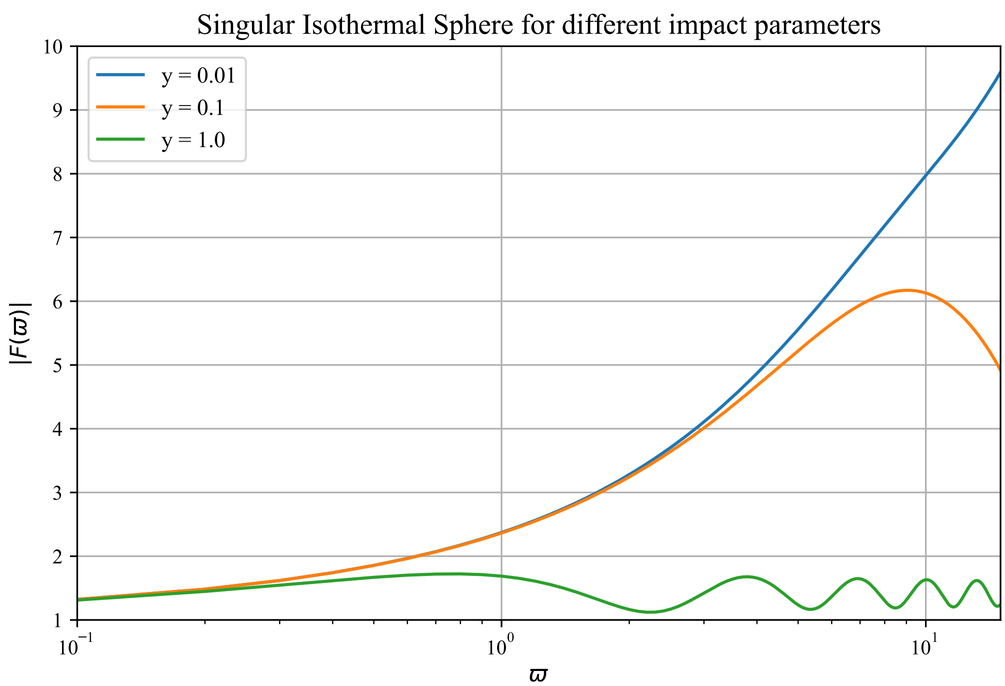

Figure 12: Amplification factor for the singular isothermal sphere lens model obtained through the full solution to the diffraction integral - Eq.(66), computed for different source positions y.

As we approach larger y values, the computational methods used to obtain $F(\varpi, y)$ fall short in the sense that they very quickly make the amplification factor diverge, even for not so large frequencies. This means that we are very limited when employing this model in this work, simply because of this fact. However, there is a lot of active work in improving the computational methods used to solve the diffraction integral - [44] and others.

3 Strong gravity lensing

To a good extent, weak gravity is a valid approximation to several lensing systems throughout the universe. However, for some exceptions, such as **triple black hole systems**, or even **binaries in AGN (Active Galactic Nuclei) disks**, which would be found in the vicinity of a supermassive black hole, **strong gravity effects are important**. Given the scales of the problem, it is expect that, for triple black hole systems, if one of the objects is slightly further away that it acts mostly as a lens, rather than affecting GW emission, we would be mostly in the **wave optics regime** . On the other hand, a stellar or intermediate mass ($\sim 10^{2,3}M_{\odot}$) binary merging in the vicinity of a supermassive black hole ($\sim 10^{6}M_{\odot}$) would nearly always be in the **geometric optics regime**. However, it is important to note that, for next generation detectors, with higher sensitivities that potentially allow us to look at a longer portion of the signal, this might no longer be truth - the very early inspiral stages of even a stellar mass binary could place us in the wave optics regime in a system like this; but it is, however, outside of the range of current detector sensitivities.

3.1 Geometric optics

In the previous section, Eq.(9) was solved for a simplified background metric. In this section we will, instead, simplify the perturbation, stating that it can be written used the WKB approximation. This means that we will employ an anstaz to describe our wave in which the phase oscillates a lot faster than its amplitude. It is a valid approximation when $\lambda \lll \mathcal{R}$ where $\mathcal{R}$ is the scale of the background curvature (**short wave expansion**).

$$h_{\mu\nu} = Re[(A_{\mu\nu} + \varepsilon A^{(1)}_{\mu\nu} + \varepsilon^2 A^{(2)}_{\mu\nu} + ...)e^{i\theta(x)/\varepsilon}] \tag{67}$$

Equation (67) shows the analytical expression employed, where ε is a small expansion parameter. It is also worth defining:

- $k_{\mu} = \partial_{\alpha}\theta$ as the wavevector,
- $A_{\mu\nu}$, $A^{(1)}_{\mu\nu}$, ... which are the complex valued amplitude tensors,
- $A = \sqrt{A^{*}_{\mu\nu}A^{\mu\nu}}$ as the scalar amplitude and
- $\epsilon_{\mu\nu}$ as the polarization tensor such that $\epsilon^{*}_{\mu\nu}\epsilon^{\mu\nu} = 1$ and $A_{\mu\nu} = A\epsilon_{\mu\nu}$.

Recovering the original propagation equation (9), we can use similar dimensional arguments to the ones used in the beginning of section 2 to simplify it. In particular, the first term ($\Box h_{\mu\nu}$) represents the scale over which the amplitude of our perturbation changes, which can be approximated to $\mathcal{O}(h/\lambda^2)$; whereas the second is comparable to the scale of the background metric curvature, as such - $\mathcal{O}(h/\mathcal{R}^2)$. Since the geometric optics approximation relies on the fact that the wavelength is a lot smaller than the scale of the background space-time curvature, we can neglect the second term of the propagation equation, which leaves us with solving simply

$$\Box h_{\mu\nu} = 0. \tag{68}$$

However, it is worth mentioning that the sub-dominance of the curvature corrections, arising from the second term of the propagation equation ($2R_{\mu\alpha\nu\beta}h^{\alpha\beta}$), becomes irrelevant if we focus on only solving for the leading order term ($\sim \varepsilon^{-2}$), since the corrections arising from this term start only at order ε^{0}.

Plugging the ansatz introduced previously - Eq.(67) into Eq.(68), we can group the terms with different orders in the expansion parameter together to get:

$$Re[\Box A_{\mu\nu} + \varepsilon \Box A^{(1)}_{\mu\nu} + \varepsilon^2 \Box A^{(2)}_{\mu\nu} + \dots] + \frac{i}{\varepsilon}\Bigg(Re[A_{\mu\nu} + \varepsilon A^{(1)}_{\mu\nu} + \varepsilon^2 A^{(2)}_{\mu\nu} + \dots] D_\alpha \partial^\alpha \theta. \tag{69}$$

$$+ Re[D_\alpha A_{\mu\nu} + \varepsilon D_\alpha A^{(1)}_{\mu\nu} + \varepsilon^2 D_\alpha A^{(2)}_{\mu\nu} + \dots]\partial^\alpha \theta + Re[D^\alpha A_{\mu\nu} + \varepsilon D^\alpha A^{(1)}_{\mu\nu} + \varepsilon^2 D^\alpha A^{(2)}_{\mu\nu} + \dots]\partial_\alpha \theta \Bigg) \tag{70}$$

$$+ \frac{1}{\varepsilon^2} Re[A_{\mu\nu} + \varepsilon A^{(1)}_{\mu\nu} + \varepsilon^2 A^{(2)}_{\mu\nu} + \dots]\partial_\alpha \theta \partial^\alpha \theta = 0. \tag{71}$$

Because ε is a small expansion parameter, we want to solve for each order iteratively, starting with the leading order - ε^{-2}. We can allow our perturbation to have a gauge freedom such that $D^\mu h_{\mu\nu} = 0$, similarly to section 1.2, which gives:

$$(D^\mu A_{\mu\nu} + \varepsilon D^\mu A^{(1)}_{\mu\nu} + \varepsilon^2 D^\mu A^{(2)}_{\mu\nu} + \dots) + \frac{i}{\varepsilon}(A_{\mu\nu} + \varepsilon A^{(1)}_{\mu\nu} + \varepsilon^2 A^{(2)}_{\mu\nu} + \dots)k^\mu = 0. \tag{72}$$

Using this, we can solve the linear order of our expansion to find:

$$\partial_\alpha \theta \partial^\alpha \theta = 0 \iff g^{(B)}_{\alpha\beta} \partial^\beta \theta \partial^\alpha \theta = 0 \iff g^{(B)}_{\alpha\beta} k^\beta k^\alpha = 0, \tag{73}$$

which means that our propagation travels along **null geodesics**, similarly to light! In order to study lensing for null geodesics, the goal is to compute the deflection angle of the geodesics, and attempt try to translate that into quantities previously derived for the geometric optics approximation in section 2.2 (image positions and magnifications). Solving for the sub-leading orders of the expansion parameter ε allows us to derive other interesting results about our perturbation, in particular, the equivalent to the electromagnetic conservation of current (in our case, of gravitons) - left as an exercise to the reader.

Tracing geodesics is very well established in GR, particularly for the Schwarschild metric. Essentially, we want to answer the question of what happens to a geodesic when propagation in the vicinity of a non-rotating black hole. The geodesic equation for the Schwarzschild metric is the following:

$$-\left(1 - \frac{2M}{r}\right)(k^t)^2 + \frac{1}{(1 - \frac{2M}{r})}(k^r)^2 + r^2((k^\theta)^2 + \sin^2\theta (k^\phi)^2) = 0, \text{ where} \tag{74}$$

$$(k^t, k^r, k^\theta, k^\phi) = \left(\frac{dt}{d\tau}, \frac{dr}{d\tau}, \frac{d\theta}{d\tau}, \frac{d\phi}{d\tau}\right) \text{ are the components of the wave-vector,} \tag{75}$$

and τ is the affine parameter used to parametrize the null geodesic (if it was time-like, τ would be the proper time) - see section 6.3 of [47]. For Schwarzschild, the metric is invariant for a $\theta \to \pi - \theta$ transformation (parity reflection symmetry). Meaning that if our geodesic lies in the equatorial plane of the sphere ($\theta = \pi/2$) initially, it will remain in that plane. So, without loss of generality, we can fix $\theta = \pi/2$, leading to $k^\theta = 0$ and $\sin\theta = 1$. To find the components of the wave vector for Schwrzschild metric (which is the evolution of the coordinates along the affine parameter τ), we write the action between two point along one curve as:

$$S = \int_{\tau_0}^{\tau_1} d\tau \sqrt{-g_{\alpha\beta}\frac{dx^\alpha}{d\tau}\frac{dx^\beta}{d\tau}}. \tag{76}$$

According to the principle of least action, a geodesic is precisely the path that extremizes the action, which means that the integrand is the Lagrangian. Solving the Euler-Lagrange equations we find that we have two constants of motion along the geodesic, given by:

$$E = \left(1 - \frac{2M}{r}\right)\frac{dt}{d\tau} \quad \text{when we solve for the } t \text{ coordinate, and} \tag{77}$$

$$L = r^2 \frac{d\phi}{d\tau} \quad \text{when we solve for the } \phi \text{ coordinate.} \tag{78}$$

Plugging these constants in the original geodesic equation - Eq.(74) leads to the following relation:

$$\frac{1}{2}\left(\frac{dr}{d\tau}\right)^2 + \frac{L^2}{2r^2}\left(1 - \frac{2M}{r}\right) = \frac{1}{2}E^2. \tag{79}$$

One can interpret this equation as the motion of a unit mass particle with total energy $\frac{1}{2}E^2$ subject to a potential $V = \frac{L^2}{2r^2}\left(1 - \frac{2M}{r}\right)$, which we can be seen in figure 13.

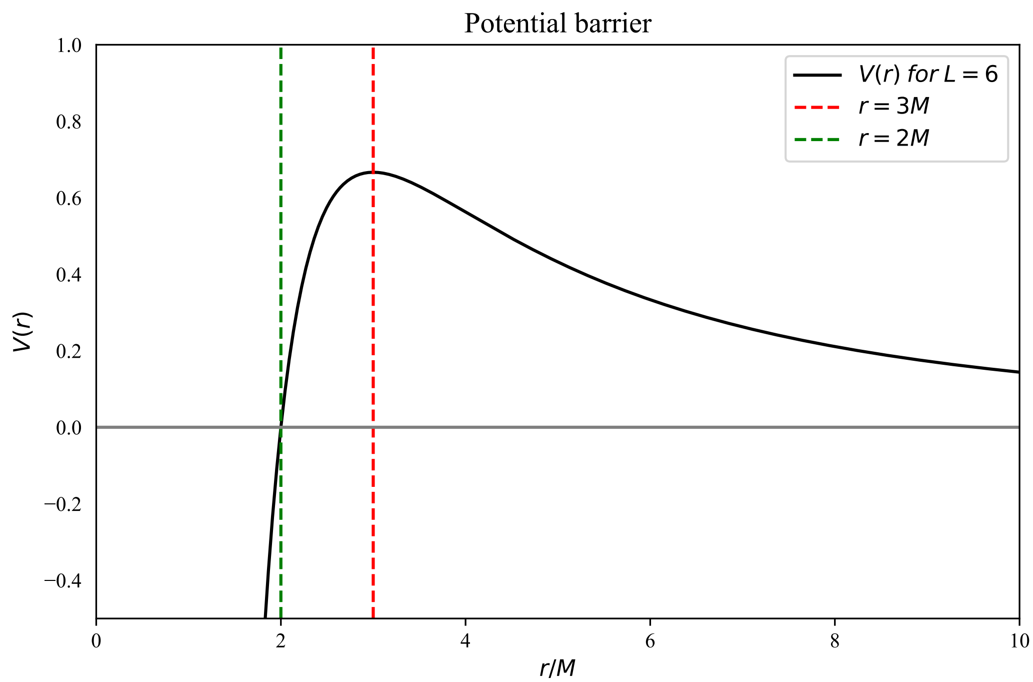

Figure 13: Representation of the Schwarzschild potential barrier for a random value of the constant of motion L. The value of these parameters has no physical importance since we simply want to understand the qualitative behavior of this potential barrier.

As we can see, this potential is zero at the Schwarzschild radius, has a single maximum for $r = 3M$ and decreases from there on. This means that a particle traveling along a geodesic (at this point, we will focus on the ones coming from infinity, since the Schwarzschild metric is asympototically flat) needs to have an energy greater than this barrier in order to not get absorbed into the BH. The minimum required energy is given by the condition:

$$\frac{1}{2}E^2 = \frac{L^2 M}{2(3M)^3} \iff b_c = 3^{3/2}M, \quad \text{where } b = \left(\frac{L}{E}\right)_{r \gg M} \text{ is the apparent impact parameter.} \tag{80}$$

Assuming that the geodesic does not plunge into the BH, the **closest approach distance** of the ray to the center of the black hole depends on the **apparent impact parameter** at ∞ and is given by the condition:

$$V(r_0) = E^2/2 \iff b^2 = \frac{r_0^3}{r_0 - 2M}. \tag{81}$$

In the absence of mass - flat metric - the impact parameter is, indeed, the same as the closest approach distance r_0, which, in section 2, we call ξ. However, in the presence of mass, this point is where the geodesic "turns" and deflects. Naturally, if the closest approach distance r_0 is the radius at which the potential has its maximum value ($r = 3M$), the impact parameter is the critical one.

The same way we used the constants of motion to rewrite the geodesic equation Eq.(74) as an equation for the evolution of r along the parameter τ, we can do the same for the coordinate ϕ and use $\frac{dr}{d\tau}\frac{d\tau}{d\phi} = \frac{dr}{d\phi}$ and the equation for $\frac{dr}{d\tau}$ to eliminate the affine parameter dependency altogether. This allows us to get the evolution of the azimuthal angle ϕ along the radial coordinate r:

$$\frac{d\phi}{dr} = \pm \frac{1}{\sqrt{r^4 b^{-2} - r(r-2M)}}. \tag{82}$$

Integrating this equation from the point of the closes approach distance r_0 until $r = \infty$ gives us how much the trajectory of the geodesic is bent due to the presence of the gravitational potential or, in other words, the **deflection angle**.

$$\Delta\phi = 2\int_{x_0}^{\infty} \frac{dx}{x\sqrt{\left(\frac{x}{x_0}\right)^2\left(1-\frac{1}{x_0}\right) - \left(1-\frac{1}{x}\right)}} - \pi, \qquad \text{where } x = \frac{r}{2M} \tag{83}$$

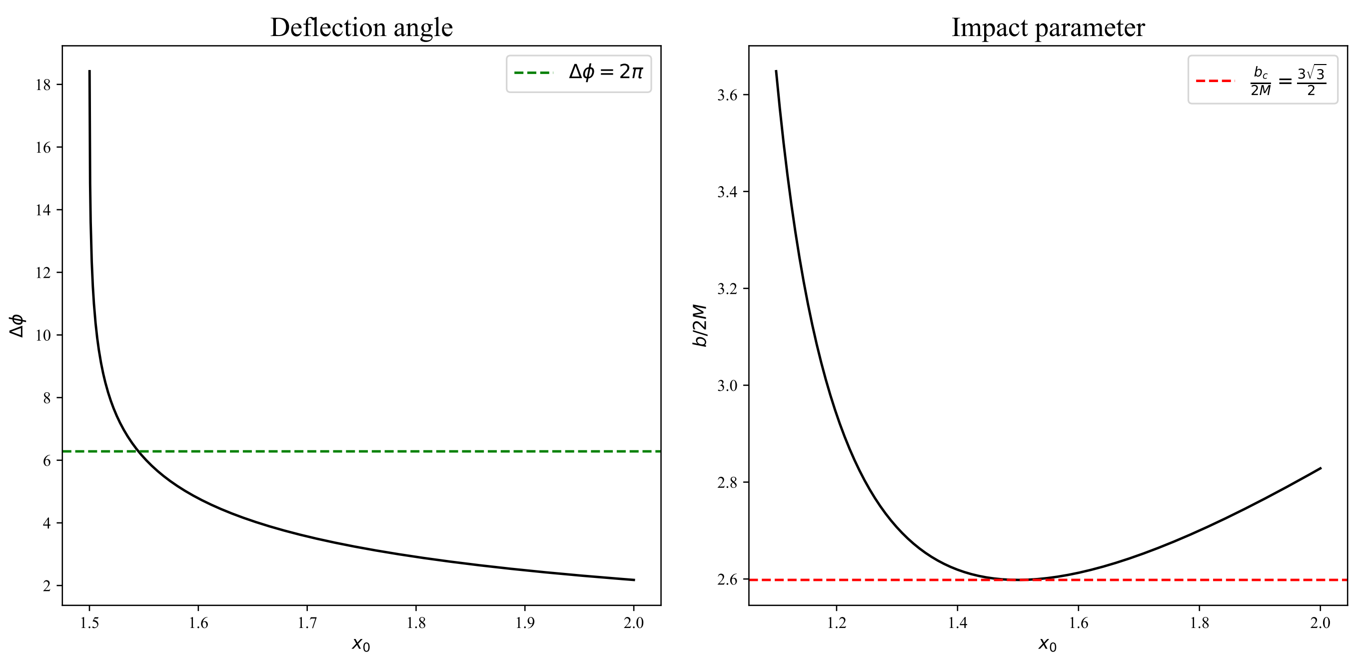

Figure 14: On the left hand side: Deflection angle in terms of the closest approach distance scaled by the Schwarzschild radius. On the right hand side: Impact parameter in terms of closest approach distance, both scaled by R_s.

In the first panel of figure 14 we show the value of the deflection angle by changing the lower bounds of the integral, which is the closest approach distance scaled by the Schwarzschild radius of the black hole. We can see that, as the closest approach distance reaches $r_0 = 3M$, which is the maximum of the potential barrier, this deflection angle diverges. In particular, it becomes higher than 2π, which represents **one full loop** around the BH - see schematic representation on top left corner of the plot 4. From the second panel of figure 14, we also confirm that the critical impact parameter corresponds exactly to the smallest possible approach distance, as expected.

In [18], the authors show the exact results displayed in figure 14, with the addition of the branch for x_0 smaller than 1.5, and they do this by using a numerical approximation to compute the deflection angle given by

$$\Delta\phi = -\log\left(\frac{b}{2M} - \frac{3\sqrt{3}}{2}\right) - \log\left(\frac{5+3\sqrt{3}}{1944}\right) - \pi. \tag{84}$$

Albeit the two lines in figure 14 seem to differ a lot for impact parameters close to the critical one, this numerical approximation, at least, gives us the freedom to explore the branch of $x_0 < 1.5$, unlike the analytical solution. Both of the solutions, for larger impact parameters, are expected to blend rendering little error in using the logarithmic approximation. This gives them the freedom to study the behavior of geodesics as they approach the closest approach distance x_0 both for $x_0 \to 1.5^+$ and $x_0 \to 1.5^-$. Essentially, they find, not unlike this work, that if we approach this $r_0 = 3M^+$, the geodesic is expected to loop around the black hole and create a photon ring - which in our case, would be a **graviton ring**. However, if we approach it from the other branch ($r_0 = 3M^-$), the geodesic very quickly plunges into the black hole and the photon gets absorbed - see figure 2 of [18]. The intermediate case is when the trajectory of the geodesic gets heavily deflected the particles traveling along it eventually reaches us, observers, creating **images**. Recovering the nomenclature used for geometric optics in weak gravity from section 2.2 , we can once again distinguish between **weak** and **strong lensing**. At a large approach distance x_0, the deflection angle $\Delta\phi$ becomes smaller and smaller, placing us in the weak lensing regime, where the trajectory of the geodesic becomes slightly deviated - see the scheme on the right of 4. Otherwise, when x_0 approaches its critical value and the geodesic loops around the BH, we expect to observe multiple images coming from the same source, placing us in the strong lensing regime.

A realistic scenario in which this relation between the impact parameter and the expected deflection angle is very useful is, for example, AGN disks. Essentially, there are several "channels" predicted by scientists through which BBHs are expected to meet and merge, creating GWs which we can detect on Earth. One of these channels is the **AGN channel**, and it describes how, in the center of every active galaxy, where there is a SMBH surrounded by a dense and bright gaseous disk, BBHs are expected to form. In these dense and dynamical environments, where we have a gaseous disk surrounded by a NSC (Nuclear Stellar Cluster), a lot of star formation and death occurs. As a result, a lot of stars in binary systems can die and form BHs that subsequently merge. Furthermore, this disk surrounding the SMBH can create what is called a **"migration trap"**due to the change in its density gradient. These traps are exactly what the name entails: a region (located at a certain radial distance from the SMBH horizon) where compact objects migrating through the disk get trapped and accumulate. If we estimate this as a likely region for GW emission to occur, using a very simple AGN disk model, we can use the height of this disk as a measure for the impact parameter (where sources could be located) and predict **whether or not this height is enough to allow the rays to escape from the SMBH and reach us**, or if they simply get absorbed. Naturally, the inclination of the disk with respect to us will have a large influence on this. However, let us consider the worst case scenario, in which the **disk is edge-on** with respect to the observer. We find that, if the migration trap is located between 20 and 200 R_s, then emission from this region is likely all captured by the central SMBH. However, in more outer regions of the disk, the height exceeds the critical impact parameter at which $r_0 = 3M$, which means the rays could, potentially, reach us. It is important to note that these results are not the absolute truth about emission from the AGN channel since this disk model is purely theoretical and not confirmed by observations - figure 16.

We can now reevaluate and realize that, if we can compute the deflection angle given the impact parameter (position

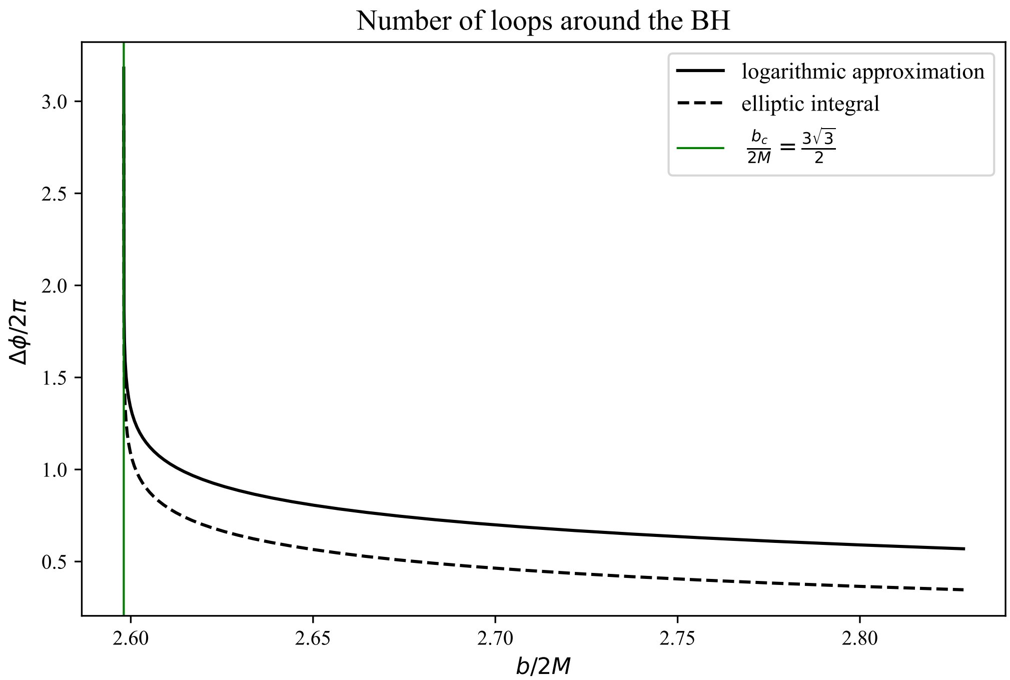

Figure 15: Number of loops a geodesic does around a Schwarzschild black hole when the impact parameter is close to its critical value. Computed using the expression derived when tracing the geodesic - Eq.(83) -and with the logarithmic approximation - Eq.(84).

of the source) we can, in theory, **predict the location of the images produced by the source, according to the lens equation**. Since Eq.(39) is taylored for small deflection angles (remember the small angle approximation made early in section 2) it is necessary to make some adjustments, since our deflection angles can become larger than 2π. However, if one defines our deflection angle as a small deviation from multiples of 2π, this small deviation can very well be used in the lens equation, allowing us to predict positions of the images generated by these small deflection, as such [10]:

$$\beta = \theta - \frac{D_{LS}}{D_S}\delta\phi_n, \quad \text{where } \Delta\phi = 2\pi n + \delta\phi_n \tag{85}$$

So, essentially, if we look at the range of values for x_0 in figure 14, we are interested in getting as close as possible to $x_0 = 1.5$ so that we have deflection angles above 2π without actually reaching it (otherwise the geodesic will plunge). For that purpose, we can define $x_0 = 1.5 + \epsilon$ (remember that x_0 gives us the deflection angle). In [7, 6], the author uses the logarithmic approximation of the deflection angle as a function of impact parameter to get the image positions, since $b \sim \theta D_L$ - see figure 1 of [7]. The author defines the θ_n^0 image positions, which are caused by deflection angles multiples of 2π, so they will be perfectly aligned with the initial trajectory of the ray. The actual image positions, created from deflection angles which are small deviations from deflections of $2\pi n$, are themselves, small deviations from the θ_n^0 images. Expanding in linear orders of $\delta\theta_n = \theta - \theta_n^0$:

$$\theta_n = \theta_n^0 + \frac{e^{A-2n\pi}(\beta - \theta_n^0)D_S}{D_{LS}D_L}, \tag{86}$$

where D_L, D_S and D_{LS} are the same as in figure 6, and β is the real angular position of the source, labeled θ_0 in figure 6.

[10]For the full derivation, one should follow [7, 6].

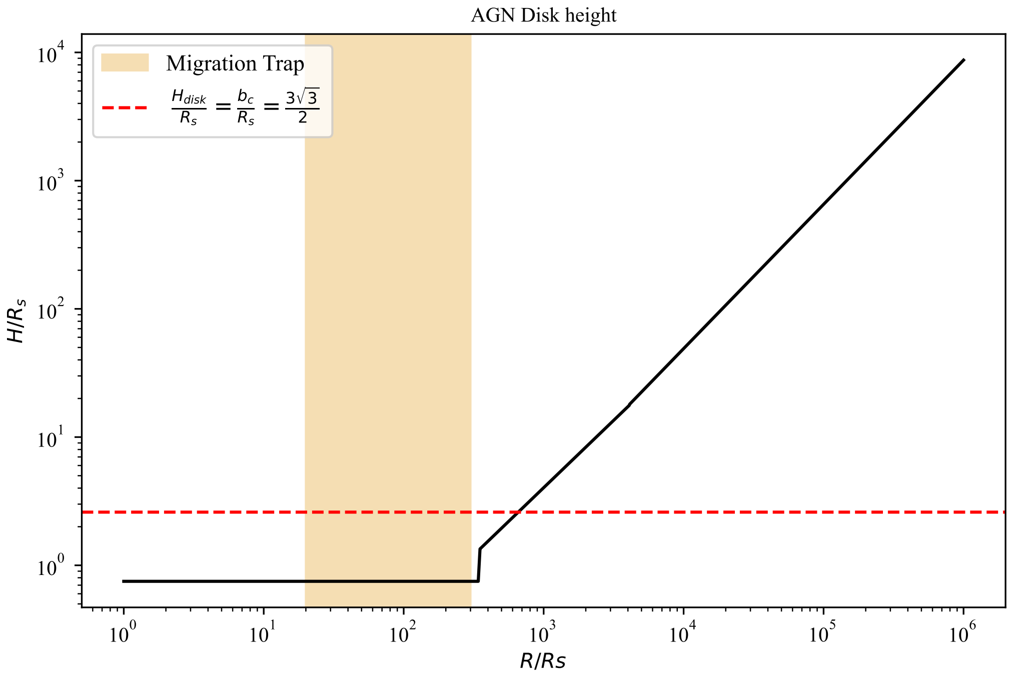

Figure 16: Plot of the approximate height of the disk of an AGN with a SMBH in the center predicted by theoretical models - [19], all scaled by the Schwarzschild radius of the central SMBH. We can also see the prediction for the location of these migration traps - [4] where binaries are likely to form, and in the y axis the critical impact parameter below which every ray plunges into the central SMBH.

The image magnifications are found, as done in section 2.2, through the lens equation, as such:

$$\mu_n = \frac{\theta_n^0}{\beta \frac{\partial \beta}{\partial \theta}\big|_{\theta_n^0}} = e^{A-2n\pi} \frac{(3\sqrt{3} + 2e^{A-2n\pi}) D_{OS}}{2\beta D_{LO}^2 D_{LS}}. \tag{87}$$

As we can see, this magnification decreases exponentially with n, which seems to show that the magnification of the first image dominates with respect to the subsequent ones. Furthermore, there is a divergence as we approach $\beta \to 0$, which is how we recover the concept of **caustics** - when the source and lens are aligned, magnifications are formally infinite.

3.2 Wave optics

Albeit the geodesic deviation is enough of a description for how a strong gravitational field deflects light, this formalism breaks down often for GWs because of their larger wavelengths. It is established that the important scale when distinguishing between geometric and wave optics is the size of the wave relative to the lens. However, more often than for light, **GWs have wavelengths comparable to the size of astrophysical objects that can act as lenses.** Furthermore, these objects, sometimes, cannot be described by a Newtonial potential due to their structure, which is the case for a black hole. Naturally, if the GW travels far enough from a BH acting as a lens, the weak gravity approximation becomes valid again, but it is not particularly trivial to draw the line between when one or the other is more valid. To fully study this phenomena, one has to resort to **Black Hole Perturbation Theory** , i.e., instead of considering an incoming gravitational wave that is changed by a lens, this theory aims to solve how a black hole responds (via GW emission) to a certain perturbation - in this case, created by an incoming GW. In section 1.3, we introduced the concept of black hole reflectivities and how they affect each spherical mode of the waveform at the observer (infinity). However, it is useful to translate this into an actual scattered waveform that can be observed.

Similarly to lensing in weak gravity, the black hole reflectivities introduced in section 1.3 - see figure 5 - have a large dependence on the comparable scales of the wave and the black hole being perturbed. At high values of ωM, the geometric optics limit dominates, and at small ωM, we are in the wave optics regime. **These reflectivities are the key variables in describing how the black hole responds to the incoming radiation**- if it transmits it or it absorbs it. At high frequencies, the reflectivities vanish and the wave gets almost fully absorbed, since the frequencies correspond to the real part of the fundamental quasinormal mode of each harmonic. Thus, for $\omega M \gg 1$, only very large ℓ modes contribute, corresponding to null geodesics, which makes us recover the geometric optics regime studied in section 3.1 - [9]. In particular, we can clearly see the reflectivities going to zero for smaller ℓ modes much earlier in frequency.

Having the tools to solve the scattering problem in the BH frame, there is still the need to construct the full gravitational perturbation before it reaches the black hole and when it reaches infinity, which represent the unlensed and scattered GWs.

3.2.1 Scattered Gravitational Waves

From section 1.3, we acquired a strong understanding of how each spherical mode of the incoming gravitational wave propagates through a Schwarzschild black hole. Therefore, in practical terms, all that is needed is to sum over all of these to obtain the initial and final wave.

Similarly to how the authors of [37] write the gravitational perturbation in a coordinate system that suits their goal, one can also write a gravitational perturbation in the Transverse Traceless (TT) gauge such that it can be described in terms of its' two propagating degrees of freedom:

$$h_{\mu\nu}dx^{\mu}dx^{\nu} = \begin{pmatrix} 0 & 0 & 0 & 0 \\ 0 & h_{+} & h_{\times} & 0 \\ 0 & -h_{\times} & h_{+} & 0 \\ 0 & 0 & 0 & 0 \end{pmatrix} \tag{88}$$

The contents of h_{+} and $h\times$ can be easily described in terms of properties of the source. In current detectors, one is able to resolve them, with some limited precision. Therefore, these two degrees of freedom are, effectively, what we detect. However, unlike what was done in section 2, where the polarization contents of the wave are irrelevant,**we will handle h_{+} and $h_{\times}$ separately since they are lensed differently.** This does not come to say that, in weak gravity, the lensing of both polarizations is the same. It is simply treated as being the same, proving that **the weak gravity approximation does not accurately account for the spin-2 nature of GWs.**

To a good extent, we can assume that the wave hitting on the lens is a **plane wave**. In particular, the distances at which this approximation becomes valid are $r \gg \frac{2M^2}{\lambda}$. For a wave of size $\lambda \sim M$ (wave optics regime), it is enough to say that the radial distance has to be larger than the size of the black hole, $r \gg 2M$. Therefore, for a source at about $50M$ (or $100R_s$) the exact "piece" that hits the lens (BH) will be plane, but strong gravity effects still need to be accounted for. Under this assumption, if we take our initially spherical wave, with an amplitude A and a time and radial dependence of the form

$$\frac{A}{r}e^{i(kr \pm \omega t)}, \tag{89}$$

and rewrite the radial coordinate as $r_{LS} + Z$, such that the plane wave hitting the black hole is:

$$h_+ = \Re\left\{\frac{e^{-i\omega(t-r_{LS})}}{r_{LS}}A_+(f,\Omega_{\rm LS})e^{i\omega Z}\right\}, \tag{90}$$

$$h_\times = \Re\left\{\frac{ie^{-i\omega(t-r_{LS})}}{r_{LS}}A_\times(f,\Omega_{\rm LS})e^{i\omega Z}\right\}. \tag{91}$$

Having defined the time and radial dependencies of our perturbation, we now want to decompose them into spherical harmonics centered around the lens and solve the scattering problem [11]. However, the two modes $(+,\times)$ don't have well defined spin weights. The helicity eigenstates $h_{\pm 2} = h_+ \pm ih_\times$ are given by:

$$h_{(\pm 2)} = H^{(\pm 2)}e^{i\omega Z} + \bar{H}^{(\mp 2)}e^{-i\omega Z}, \tag{92}$$

$$\text{where } H^{(\pm 2)} = \frac{e^{-i\omega(t-r_{\rm LS})}}{2r_{\rm LS}}\Big(A_+ \mp A_\times\Big), \tag{93}$$

and $\bar{H}$ is the complex conjugate. Having a well defined spin, it is possible to decompose our perturbation into spin weighted spherical harmonics [39], (since our gravitational perturbation is a spin-2 field), - [25, 34], centered around the lens. The radiative field at infinity (h_+ and $h_\times$) can be related to the Regge-Wheeler-Zerilli (RWZ) master variables ($\psi^\bullet_{\ell m}$), as done in Eq. (6.14) and (6.15) of [25]. Applying this to our spin eigenstates, we are able to extract the weight of each spherical harmonic with spin $s = \pm 2$ as such:

$$h_{(\pm 2)} = \sum_{\ell m} h^{(\pm 2)}_{\ell m} Y^{(\pm 2)}_{\ell m} \quad \text{where} \quad rh^{(\pm 2)}_{\ell m} = \frac{1}{2}\sqrt{\frac{(\ell+2)!}{(\ell-2)!}}\Big(\psi^{even}_{\ell m} \pm i\psi^{odd}_{\ell m}\Big). \tag{94}$$

Now that we have been able to relate the spin eigenstates of our incoming plane wave to the RWZ master variables, we can solve the scattering problem on $\psi^\bullet_{lm}$. However, we want to have a clear relation between the master variables and the amplitudes of our plane wave (we currently have the opposite). To do so, we can remind ourselves of the decomposition of a scalar plane wave into spherical harmonics

$$e^{i\omega r\cos\theta} = \sum_\ell i^\ell \sqrt{2\ell+1}\, j_\ell(\omega r) P_\ell(\cos\theta), \tag{95}$$

where $j_\ell(x)$ is the Bessel function of the first kind of order ℓ and $P_\ell(\cos\theta)$ are the Legendre polynomials. We know that our spin eigen states, which we decomposed into spherical harmonics, are a (spin-2) plane wave which we can also decompose using a generalization of Eq.(95) for spin-2 waves - [34, 35]. It leads to the following expression relating the amplitudes of the plane wave H to the RWZ master variables:

$$\psi^{even}_{\ell m=\pm s} = \frac{iH^{\mp 2}}{\omega}\sqrt{\pi(2\ell+1)}\sqrt{\frac{(\ell-2)!}{(\ell+2)!}}\Big[(-1)^\ell e^{-i\omega r_\star} - e^{i\omega r_\star}\Big] + \text{c.m}, \tag{96}$$

where c.m stands for the conjugate mode: for a given $\psi^\bullet_{\ell m}$, the conjugate mode is given as $(\psi^\bullet_{\ell,-m})^*$. The only azimuthal numbers that contribute are those equal to the possible spin weights, such that $|m| = s = 2$. However, the reflectivities do not depend on m due to spherical symmetry.

In order to account for the strong-field effects, we rescale the outgoing component of our RWZ solution ($e^{i\omega r_\star}$) by

[11] One can also follow [10] for the next steps of this derivation.

the reflectivities of the BH , and subtract the incoming component, in order to isolate the strong field effects:

$$\tilde{\psi}^{even}_{\ell m=\pm s} = \frac{iH^{\mp 2}}{\omega}\sqrt{\pi(2\ell+1)}\sqrt{\frac{(\ell-2)!}{(\ell+2)!}}\left[1+(-1)^{\ell}\mathcal{R}^{even}_{\ell m}\right]e^{i\omega r_\star} + \text{c.m}, \tag{97}$$

where the same relation between even and odd $\psi_{\ell m}$ holds. The incoming component will be summed back, unaffected, as a part of the wave that propagates without hitting the black hole. The following step is to re-sum over ℓ the spherical harmonic spin weights as introduced in Eq.(94), but with the lensed variables $\tilde{\psi}_{\ell m}$ instead of the original ones. That way, after some algebraic manipulation, the amplitudes of the helicity eigen states of the lensed waveform $\tilde{H}^{(\pm 2)}$ are related to the original ones via a frequency dependent factor [12]:

$$\tilde{H}^{\pm 2} = \mathfrak{F}^{\pm} H^{(\mp 2)}/\omega, \tag{98}$$

$$\text{with } \mathfrak{F}^{\pm}(\Omega_{\rm OL}) = \frac{i\sqrt{\pi}}{2}\sum_{\ell,|m|=2}\sqrt{2\ell+1}Y^{(\pm 2)}_{\ell m}(\Omega_{\rm OL})\left(\left[1+(-1)^{\ell}\mathcal{R}^{\rm even}_{\ell m}\right] \mp \frac{m}{|m|}\left[1+(-1)^{\ell}\mathcal{R}^{\rm odd}_{\ell m}\right]\right), \tag{99}$$

where $\Omega_{OL} = \{\theta_{OL}, \phi_{OL}\}$ is the angular position of the observer with respect to the lens (remember that the spherical harmonics are centered around the lens).

As stated earlier, for each ℓ mode, there are two contributions, one for $m=2$ and one for $m=-2$. As we can see, in the case of $m=2$, the sum depends explicitly on $\mathcal{R}^{even}_{\ell m} - \mathcal{R}^{odd}_{\ell m}$. As we go to higher ℓ modes, this difference converges to zero, which causes no obstacle in achieving very high values of ℓ and getting an accurate computation of these factors. However, for $m=2$, the exact opposite happens, which is why in [10], the authors resort to a Cesaro sum (see appendix A of the paper), for which this sum converges. However, there is still a numerical complication in summing up to large ℓ values when the angle between the lens and the observer θ_L is small - which, in weak gravity, corresponds to small impact parameters. This will heavily constrain the kind of physical system we can analyze.

Finally, similarly to how we took the propagation modes h_+ and $h_\times$ and rewrote them as spin eigenmodes, we can now do the opposite to get the lensed version of the two polarization modes. The lensed h_+ and $h_\times$, will be given as the sum of the scattered outgoing wave and the unaffected wave, as such:

$$h^{lensed}_{+/\times} = h^{unlensed}_{+/\times} + \tilde{h}_{+/\times} \quad \text{where, explicitly, the lensed component is given by} \tag{100}$$

$$\tilde{h}_+ = \frac{e^{-i\omega(t-r_{\rm LS}-r_{\rm OL})}}{4\omega r_{\rm LS} r_{\rm OL}}\left[\left(\mathfrak{F}^+ + \mathfrak{F}^-\right)A_+(\Omega_{\rm LS}) + \left(\mathfrak{F}^+ - \mathfrak{F}^-\right)A_\times(\Omega_{\rm LS})\right] + \text{c.c.}, \tag{101}$$

$$\tilde{h}_\times = \frac{e^{-i\omega(t-r_{\rm LS}-r_{\rm OL})}}{4i\omega r_{\rm LS} r_{\rm OL}}\left[\left(\mathfrak{F}^+ - \mathfrak{F}^-\right)A_+(\Omega_{\rm LS}) + \left(\mathfrak{F}^+ + \mathfrak{F}^-\right)A_\times(\Omega_{\rm LS})\right] + \text{c.c.} \tag{102}$$

In turn, the unlensed contributions are simply the plane waves measured at the observer, which are given by Eq.(91) for the coordinates of the observer with respect to the source Ω_{OS}, r_{OS}. As one can tell, the amplitudes of the plane waves A_+ and $A_\times$ that we need to sum in order to write the final lensed waves are measured in different sky locations - one is at the observer, and the other one at the lens (with respect to the source). However, we are interested in sources and lenses both located at cosmological distances from us (observers), but within the same system. Therefore, the solid angles at the lens and source are comparable to us, observers - $\Omega_{LS} \sim \Omega_{OS}$, such that we can approximate $A_{+/\times}(\Omega_{OS}) \sim A_{\times/+}(\Omega_{LS})$. Adding both of the contributions $\tilde{h}$ and $h^{unlensed}$, we arrive at a **final expression for the lensed polarizations h_+ and $h_\times$ in terms of the original ones**:

[12] this is done by expanding the conjugate mode explicitly, which yields a contribution that goes as $e^{i\omega r_\star}$ and one as $e^{-i\omega r_\star}$.

$$h^{lensed}_{+/\times} = \mathcal{F} h^{unlensed}_{+/\times} + \mathcal{G} h^{unlensed}_{\times/+} \quad \text{where the amplification functions } \mathcal{F} \text{ and } \mathcal{G} \text{ are:} \tag{103}$$

$$\mathcal{F} = 1 + \frac{r_{\rm OS} e^{-i\omega(r_{\rm OS} - r_{\rm OL} - r_{\rm LS})}}{2\omega r_{\rm OL} r_{\rm LS}} (\mathfrak{F}^+ + \mathfrak{F}^-) \text{ and } \mathcal{G} = \frac{r_{\rm OS} e^{-i\omega(r_{\rm OS} - r_{\rm OL} - r_{\rm LS})}}{2\omega r_{\rm OL} r_{\rm LS}} (\mathfrak{F}^+ - \mathfrak{F}^-) \tag{104}$$

The first takeaway from this expression is the evident **polarization mixing** that no amplification function in this project so far has been able to capture. In particular, there is a polarization conserving contribution from $\mathcal{F}$ and then there is contributions from the other polarization mode, scaled by the factor $\mathcal{G}$.

The second takeaway is that, after restoring the azimuthal angle dependence explicitly, both the amplification functions can be defined in terms of a single function $\mathbb{F}$ with different ϕ dependencies, which can be confirmed by isolating the $Y^{+2}_{\ell m}(\theta_{OL}, \phi_{OL}) \pm Y^{-2}_{\ell m}(\theta_{OL}, \phi_{OL})$ terms of the amplification functions:

$$\mathcal{F} = 1 + \mathbb{F} \cos(2\phi_{\rm OL}) \,, \qquad \mathcal{G} = i\mathbb{F} \sin(2\phi_{\rm OL}) \tag{105}$$

This means that, for a certain choice of ϕ, one can have full conservation of the initial polarization, and no mixing is observed. Therefore, it is natural to conclude that the **mixing of both of the polarizations is an effect that arises exclusively due to the tensorial treatment of the gravitational wave, and not due to the scattering off the black hole**. If one thinks about the fact that our black hole is non-rotating, it follows that polarization mixing is not necessarily an effect caused by it. If, ideally, the source, the lens and the observer were to be aligned in the equatorial plane, the polarizations would be fully preserved and, in fact, no mixing would be observed.

Nevertheless, the authors of [10], have been able to construct these frequency dependent amplification functions, similarly to the ones found in section 2 given in Eq. (61), (66), for example, which places us in the bottom left corner of figure 4. Therefore, it is worth to see what it looks like and make a hands on comparison to the ones for weak gravity. To do this, we must, first, establish a physical configuration of source-lens-observer, which is, in weak gravity, the same as choosing an impact parameter y.This physical configuration consists of:

- a distance between source and lens of $r_{LS} = 100 M_{Lens} = 50 R_s$, which renders strong field effects non-negligible, but retains the validity of the plane wave approximation;
- a lens and source at a cosmological distance from the observer ($z = 0.1$) but not from each other. Because both the lens and the source are in the same local universe, the distances source-observer and lens-observer are far more comparable than lens-source, $r_{LS} \ll r_{OS} \sim r_{OL}$, which greatly simplifies the exponentials in Eq.(104);
- we fix ϕ_{LS} at $\pi/6$ in order to be able to observe some polarization mixing, and $\theta_{LS} = \pi/6$ to be able to get a convergence on the sum in Eq.(99) - it becomes more computationally expensive for smaller angles, which would yield far more visible strong field effects.

We also wish to make an equivalence between strong gravity and weak gravity, therefore we set this same physical setup for weak gravity, but for a point mass lens model instead of a black hole - Eq.(61), in particular. The only parameter on which each of the amplification factor depends on (other than frequency) is the impact parameter. Due to the geometry of the system, the dimensionless impact parameter y can be rescaled by the Einstein angle θ_E to regain dimensions and then written in terms of the angle θ_{LS} and the distance r_{LS} , and, for our chosen physical setup, it gives:

$$y = \frac{\tan(\theta_{LS})}{\theta_E} \frac{D_{LS}}{D_{OL}} \sim 2.69 \tag{106}$$

The distances D_{LS} and D_{OL} are the distances between the plane of the lens and source and lens and observer, respectively. Keep in mind that, by construction, the dimensionless frequency introduced in section 2 differs from the dimensionless frequency ωM from this section by a factor of 4. Explicitly:

$$\varpi = 4\omega M. \tag{107}$$

Finally, for this physical setup, we plot in figure 17 the absolute values of the amplification factors $\mathcal{F}$ and $\mathcal{G}$ against the Point Mass Lens (PML) amplification factors as a function of the dimensionless frequencies ωM.

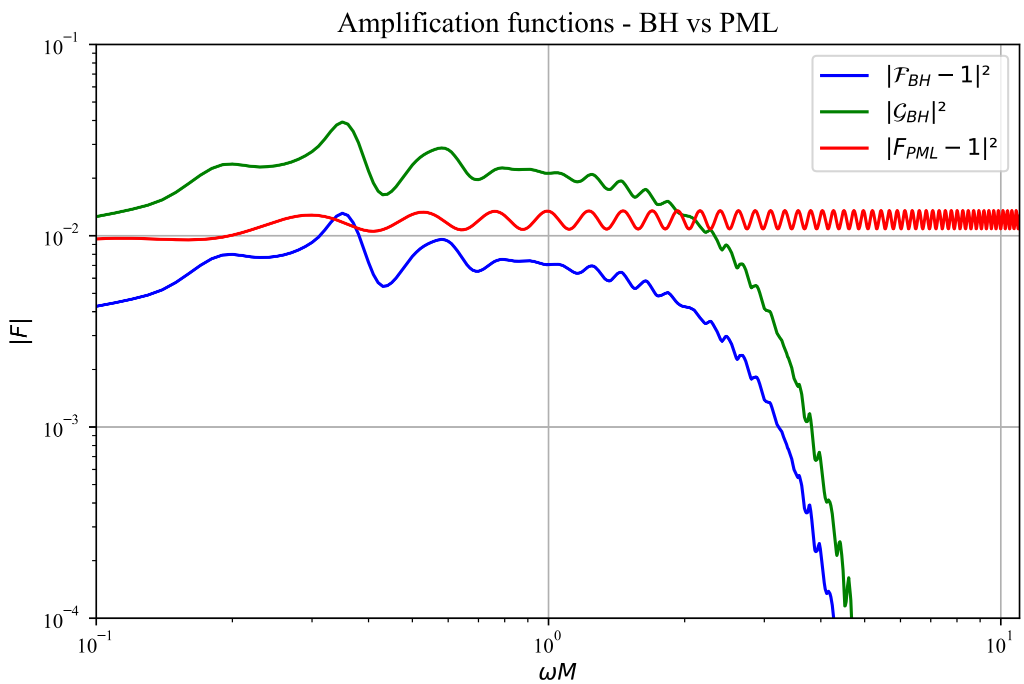

Figure 17: Amplification functions of the Schwarzschild black hole - both the polarization conserving and polarization mixing ones - Eq. (104); against the PML model - Eq.(61) in terms of the dimensionless frequency ωM.

As we can see in figure 17, the PML and BH amplification factors behave very differently at higher frequencies. When we approach the geometric optics limit - at high ωM - the polarization conserving factor $\mathcal{F} \to 1$ and the polarization mixing $\mathcal{G} \to 0$, whereas F_{PML} simply becomes highly oscillatory, as predicted. This is because, in strong gravity, the BH **absorbs** the radiation, which agrees with the behavior of the reflectivities at high ωM, causing the outgoing part of the wave, scaled by $\mathcal{R}$, not to reach infinity. Therefore, we see that the lensed strain becomes closer and closer to the unlensed one - which propagates unaffected by the gravitational potential of the BH.

Furthermore, we observe what seems to be a **beating pattern in the early frequency range of the $\mathcal{F}$ and $\mathcal{G}$ amplification factors, which could be associated with intrinsic properties of the BH. Therefore, even in a setup where the source alignment with the lens is not ideal for lensing, we can see clear qualitative differences between treating the lens as a black hole as opposed to a point mass**. This proves the need to account for the complex structure of extremely compact objects when handling lensing in strong gravity.

4 Lensed waveforms

4.1 Methods and detectability

To study exactly how these amplification functions act on a real GW event, we use the python package pyCBC - [32], github - for GW astronomy that allows us to generate templates for waveforms given the properties of the source. In this work, we will study the effect of different lenses on waveforms varying not only the total mass of the binary but also its mass ratio, and the placement of the source with respect to the line of sight (otherwise known as impact parameter). After generating a certain waveform, all one has to do is compute its Fourier transform and apply the frequency dependent amplification factors found in sections 2 and 3. However, it is important to note that these amplification factors depend on two free parameters - the **dimensionless frequency** and the **impact parameter** . To convert from dimensionless frequency to Hz, we need to fix a particular lens mass. The impact parameters is set by the relative position of the source with respect to the lens.

In this work we focus on binary sources that are within the **LIGO band**, with total masses no greater than $m_1 + m_2 = 200M_{\odot}$, and the minimum frequency we allow the waveform to have for analysis purposes is $f_{min} = 20$ Hz. This means that our waves will span over a certain range of frequency values, which, depending on the lens masses, can put us in the geometric optics or wave optics regime. We also fix the source at redshift $z = 0.1$ and include the cosmological propagation when converting between the dimensionless frequency at the lens and the frequency in Hz at the observer.

After lensing our waveforms we also compute the **mismatch** between the lensed and the original waveforms. The mismatch is a statistical measurement used in GW astronomy to match the waveform measured by detectors to the templates obtained from simulations, such as the ones used by pyCBC. The better the match between the two waveforms (measured and template), the more likely our event is to be from a source with the parameters set to run the simulations. This is, in broad terms, how scientists infer the properties of GW events. The mismatch is given as the internal product of the two waveforms, weighted by the noise of the detector. Specifically:

$$\text{Mismatch} = 1 - \mathcal{M}(h_1|h_2), \text{where } \mathcal{M}(h_1|h_2) = \frac{(h_1|h_2)}{\sqrt{(h_1|h_1)(h_2|h_2)}} \tag{108}$$

$$\text{and the inner product is } (h_1|h_2) = 4\Re\left\{\int_0^{\infty} df \frac{h_1^*(f)h_2(f)}{S_n(f)}\right\}. \tag{109}$$

This is computed in the frequency domain and $h_1^*(f)$ is the complex conjugate of the original strain $h_1(f)$ at that frequency value. This computation is also **minimized over time delay**. What this means is that, after the waveform is lensed, when we compare to the original one, we shift one of them in time domain so that they are as aligned as possible when computing the inner product. Ideally, the amplitude peaks are aligned with each other leading the mismatch to be minimized. $S_n(f)$ is simply the detector noise, which, for this work, is set to be the one from LIGO observing run 1, which is available the public - LIGO-O1-noise. Despite the fact that this is the true noise at the detector at the time of the first event - GW150914 [1] - it is a rather large noise. For the more recent observing runs, as well as for future ones, it is expected that this noise will be lower and the signals will have be louder (they will have a higher Signal to Noise Ratio). The optimal SNR (Signal to Noise Ratio) is given as the internal product of the signal with itself:

$$SNR^2 = (h|h). \tag{110}$$

To better visualize exactly what these measurements can tell us, we will focus on one particular example. The first step of the analysis will be to quantify exactly how to minimize the mismatch over time delay, for a random set of time delay values applied to one particular waveform. That waveform is chosen to be first detected GW event - GW150914, [1, 2]. We start by generating the waveform using pyCBC - which uses the original LVK collaboration waveform library LALsimulations [23] - for a binary with component masses $M_1 = M_2 = 30M_\odot$ and with spins aligned[13], which resemble the properties of GW150914. Afterwards, we move them into frequency domain via a Fourier transform, and then apply several values of time delay, $T_d \in [-0.08, 0.08]s$. Considering that the first detected event lasted for about 200 miliseconds in the detector, these are rather large time delays .

$$\tilde{h}(f) = h(f)e^{i2\pi f T_d}. \tag{111}$$

It is important to note that these time delays have no physical meaning in the sense that they are not caused by a specific lens, they are just values that were chosen with respect to the duration of the signal to test the effects of a time delay in computing mismatches. In real lensing systems, when galaxies act as lenses, time delays are expect to be in the order of hours, or even days, much larger than the duration of the signal. In that case, the images don't interfere and we just receive the same event several times, with different magnifications.

After applying the time delays to the generated waveform, we find that the mismatch behaves as seen in figure 18:

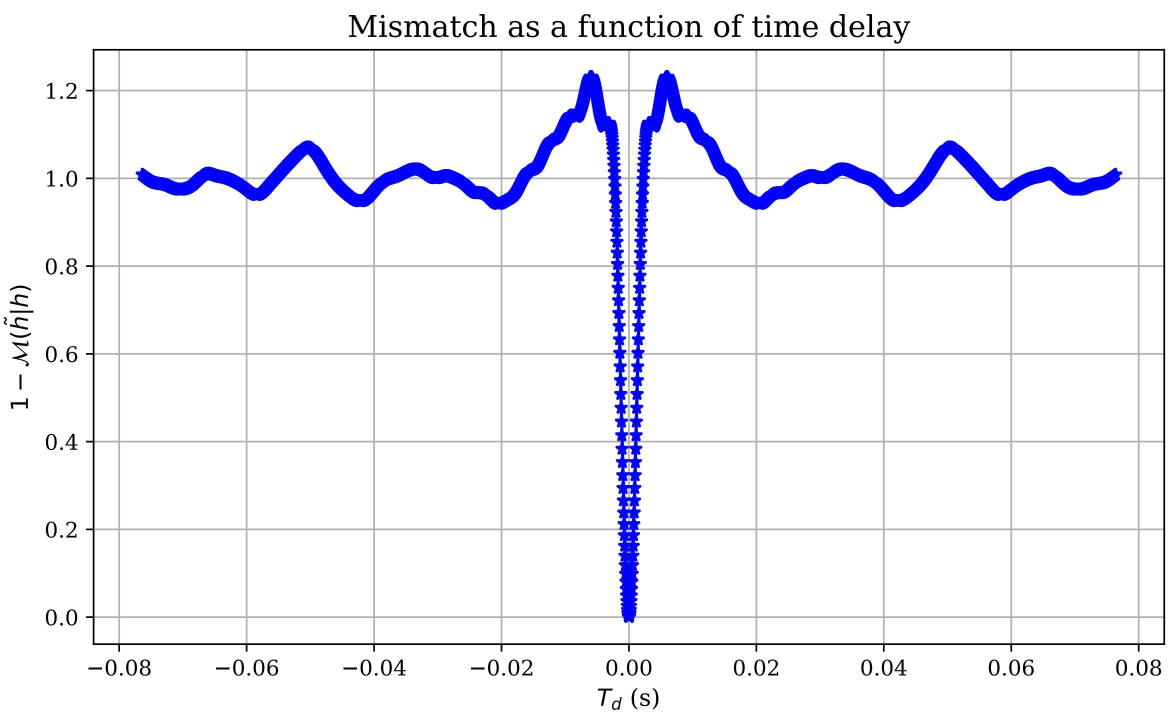

Figure 18: Mismatch of the delayed waveforms with respect to the original event GW150914 as a function of the time delay applied.

Because we are computing the match of a waveform with itself, this measurement is very sensitive to even the smallest of time delays. As logic dictates, the mismatch vanishes if the time delay applied is zero (the match is maximum). However, one would think that the mismatch would simply by $= 1$ for the whole remainder of the time delays, and that is not the case. When applying an overall time delay $\neq 0s$ to a waveform and then measuring the match of that waveform against the non-delayed one, two different things occur. Either that time delay is infinitely close to zero and the waveform almost doesn't get affected, in which case the mismatch is infinitely close to zero, which is why we see a big dip of the mismatch around $T_d \sim 0$; or the time delay actually "makes a difference", which makes the mismatch very quickly approach 1 (the waveforms match very little), which is also visible. The reason why the mismatch oscillates around

[13] The approximant used to generate these waveforms was 'IMRPhenomX', one of the many available through pyCBC.

$1 - \mathcal{M} = 1$ is because of the following: in the points where the mismatch peaks, both of the waveforms are completely out of phase, and the local minimums (excluding zero) are the points where the waves are not perfectly out of phase but match very little. This has to do with resonances between the period of the wave and the time delays applied. It makes sense that the largest peaks are right around zero, at very small time delays, since the points of highest intensity of the waveforms (the ones that contribute the most to the mismatch) are around the merger, where the frequency is highest and the period is the smallest. This means that it **it is not necessarily the largest time delays overall that lead to the highest mismatches**. It is also very important how that time delay compares to the period of the signal.

4.2 Astrophysical scenarios

4.2.1 Weak gravity lenses

For this section, we use the same waveform as earlier, with properties similar to GW150914 but, instead of applying time delays with no physical characteristics, we apply the amplification functions caused by the presence of a Point Mass Lens - section 2.3.2. We choose the mass of the lens to vary between 30 and $600 M_\odot$ and simulate three different physical setups, with the source being progressively more aligned with the lens (in the vicinity of a caustic).

To do so, we first must convert the frequency values into dimensionless frequencies. Remembering Eq.(35) where the dimensionless quantities were introduced, and adopting the Einstein angle as a normalizing constant, then:

$$\xi_0 = D_L \theta_E = D_L \sqrt{\frac{4GM}{c^2} \frac{D_{LS}}{D_L D_S}} \qquad \Longleftrightarrow \qquad \varpi = 8\pi f (1 + z_L) \frac{G M_L}{c^2}, \tag{112}$$

where $z_L = 0.1$ is the redshift of the lens and M_L is the mass of the lens. As we can see explicitly, **varying the mass of the lens changes where we are in dimensionless frequencies range**. Having done so, we simply choose one impact parameter in order to get the amplification factor that should be applied to the waveform. For this work, we chose $y = \{0.01, 0.1, 1\}$. [14] Following this, we compute the mismatch between the GW150914-like waveform generated initially and the lensed one. Similarly to what is done in the previous section, we minimize the mismatch over time delay, and find the following - figure 19:

We can see that the largest impact parameter ($y = 1$: solid line) displays a relatively constant behavior in the mismatch. This can be explained simply due to the fact that, for such a setup, where the lens and the source are quite misaligned, lensing does not play a vital role - i.e., changes to the waveform are almost negligible. As we can see, the mismatch is never greater than 0.08, which is quite low for observational purposes.

At $y = 0.1$ (dashed line), the mismatch oscillates and takes substantially larger values than both of the other two cases. This behavior is not intuitively simple to explain, but looking at individual cases of the lensed waveforms can, perhaps, shed some light on the situation. For example, one would assume that in the case where the source and lens are the most aligned ($y = 0.01$: dotted line) lensing would be more prominent and, therefore, the mismatch would be the highest.

One very possible way to account for this behavior is by looking at figure 10. We can see that smaller impact parameters have, indeed, much larger amplifications. However, **the signal being intrinsically brighter does not necessarily lead to higher mismatches**, and this simply stems from the definition of the inner product and how the mismatch is defined - see Eq.(109). The major source of measurable changes in waveforms is the oscillations in the amplification functions, which causes several images to form and interfere. Figure 10 shows that the smaller the impact parameter, the later the oscillatory behavior of the function starts. This means that, for the same range of dimensionless frequencies,

[14] It is important to keep in mind that the impact parameter is dimensionless, and is normalized by the Einstein angle of the lens; explicitly, $y = \theta_0/\theta_E$. As such, y takes into account both the angular position of the source (θ_0) and the angular extent of the lens (θ_E). Therefore, the same source position for two different lenses leads to different impact parameters y.

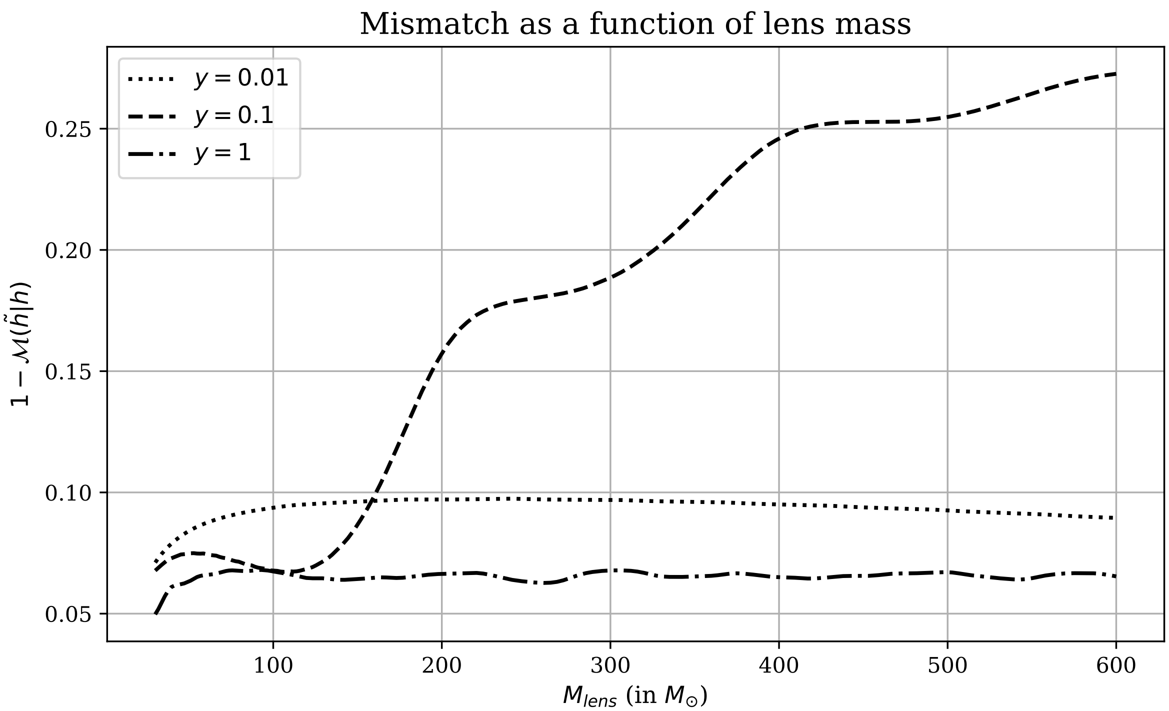

Figure 19: Plot of the mismatch between the waveform lensed using the PML model and the unlensed one as a function of the lens mass. Each line style and color represents a different impact parameter.

depending on the impact parameter, we can find ourselves in the wave optics and geometric optics regime. In other words, **there are more variables that play a part in setting which regime of lensing applies other than the dimensionless frequency.**

To better understand the tendencies in the mismatch, we look at three individual cases/waveforms: the maximum mismatch at $y = 0.01$, which happens for a lens mass of $M_L = 270M_{\odot}$ (green line of figure 20) and both the maximum and minimum mismatch for $y = 0.1$ ($M_L = 600M_{\odot}$ - blue line and $M_L = 111M_{\odot}$ - red line, respectively).

In this case, the red and blue line are subject to the same amplification function - orange line in figure 10. However, the lower lens mass places us in a lower (dimensionless) frequency range ϖ, and $M_L = 600M_{\odot}$ places us at high ϖ. We can clearly see that the green waveform in the top left plot is simply higher in overall amplitude $|h_{\times}|$, whereas the blue line has a totally different shape. The blue line corresponds to a waveform in the geometric optics regime that shows the interference between the images that are being created, and this can be confirmed by looking at the bottom left panel of figure 20. **The final waveform is not only amplified but completely distorted, which is why the mismatch in this case is much higher.**[15]

The red line is subject to a different amplification function since it has a different impact parameter, which corresponds to the light blue line of figure 10. Since it is being lensed by a mass slightly higher than the green line, but much lower than the blue line, we can infer that its range of ϖ is somewhere in between the other two. Therefore, in this case, the waveform suffers from a large amplification but not heavy distortions arising from the interference of multiple images.

Overall, **the brightest signals (highest SNR) are indeed those that are lensed in the wave optics regime, when the source is located near caustics.** However, the **most conspicuous signatures of lensing that dramatically increase the mismatch to the waveforms are found in the geometric optics regime**- blue line of figure 20.

Lastly, all of the waveforms are brighter than the original one, which proves the power of lensing in looking at distant

[15]It might be challenging to resolve all of the lines on the bottom left panel. However, the blue time domain is exactly the same as the one used on the right hand side of figure 1, so one can look at that for a better visualization.

sources. We can, furthermore, confirm that the SNR of the GW150914-like (unlensed) waveform, closely resembles the one at the first detection of LIGO O1 - authors of [1] find that SNR ~ 25.1 for a $36.2M_\odot$ on $29.1M_\odot$ binary.

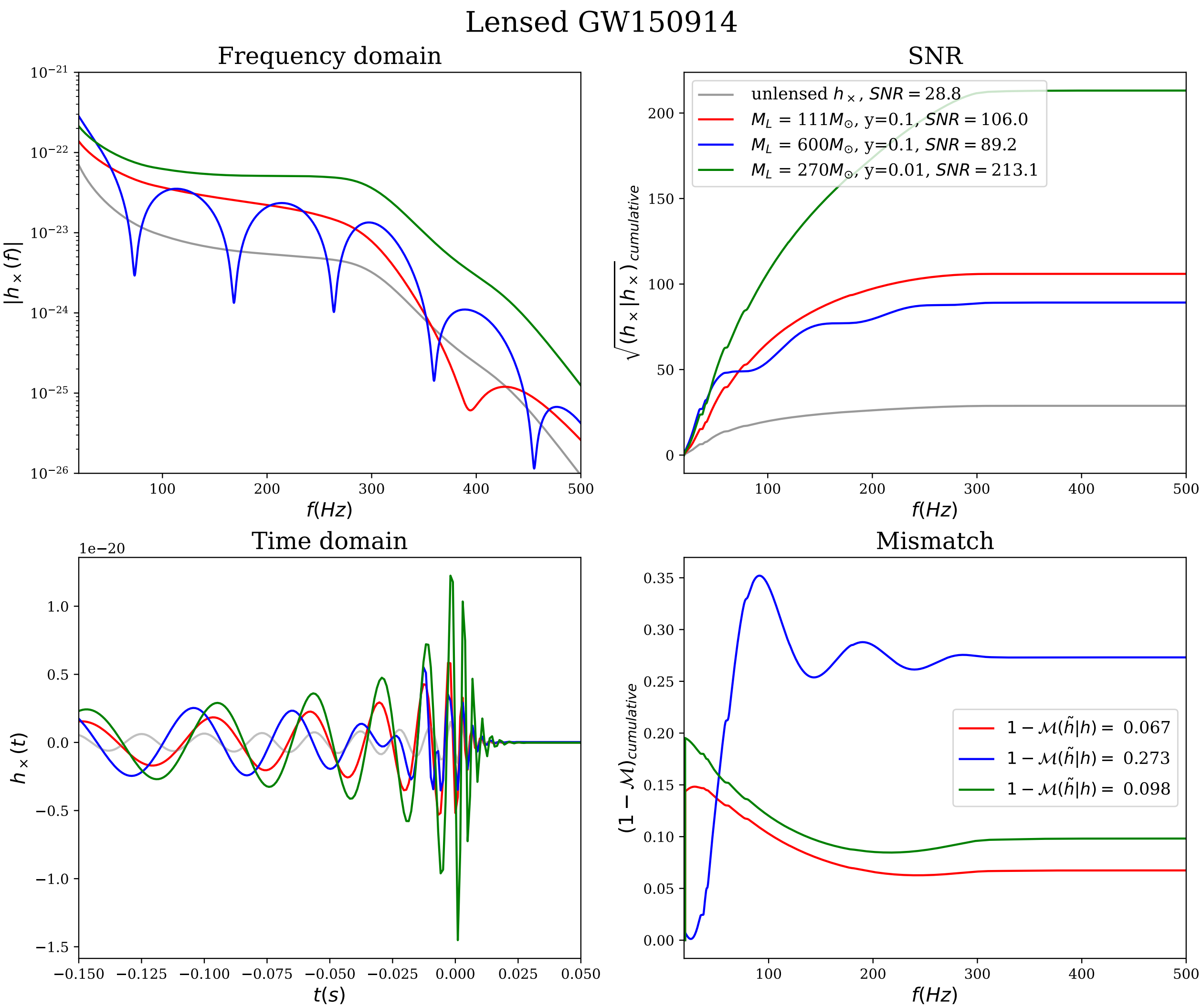

Figure 20: Same waveform lensed for three different setups. The red and blue lines are both at $y = 0.1$, one for a lens mass of $M_L = 111M_\odot$ - red; and the other for $M_L = 600M_\odot$ - blue. The line for a smaller impact parameter $y = 0.01$ (in the vicinity of a caustic) lensed for a lens mass of $M_L = 270M_\odot$ is green. The grey line is the original waveform. The **top left panel** shows the absolute value of the $h_\times$ polarization in frequency domain (the minimum frequency is set to $20Hz$). The **top right panel** shows the evolution of the SNR in frequency - the integral of the internal product of the signal against itself in Eq.(109) is computed cumulatively. The **bottom left panel** shows the time domain waveform, original and lensed ones, as we would see them on a detector. The **bottom right panel** shows the evolution of the mismatch with frequency. Similarly to the SNR, the integral in Eq.(109) is computed cumulatively, but in this case its of the original signal against the lensed one.

4.2.2 Strong gravity lenses

Having tested out how a PML acts on one specific waveform, we focus on employing a similar methodology, but for a Schwarzschild BH acting as a lens. Due to numerical obstacles, as mentioned in section 3.2, this study is limited to one specific physical setup and a range of dimensionless frequencies. However, despite being bound by these circumstances, we can **apply the amplification functions represented in figure 17 to several different waveforms, as long as their frequencies and lens masses place us in the range of ωM for which we can compute $\mathcal{F}$ and $\mathcal{G}$** (which are the BH amplification functions). This means we need to fine-tune both the mass of the binary and of the lens. The lens masses are chosen to be between 70 and $700M_{\odot}$.

Similarly to before, we set the minimum frequency to be that of LIGO sensitivity, which is $f = 20Hz$. We tackle this problem from two different fronts: at first, we set our binaries to have **equal component masses**. Different component masses will cause the waveforms to range over different frequency values, with the higher masses having shorter signals, with lower frequencies (it's little over one peak/oscillation); and the lower masses having longer signals that reach higher frequency values. The chosen component masses which place us within the correct range of dimensionless frequencies, for the previously introduced lens masses, is $m_1 \in \{4M_{\odot}, 100M_{\odot}\}$. This means that our binary masses range from 8 to $200M_{\odot}$. This range was chosen considering both how low in mass a BH can be (needs to have $M > M_C$, where $M_C = 1.4M_{\odot}$ is the Chandrasekhar mass), and how high in mass the detected events by LIGO are (so far, no binary heavier than $120M_{\odot}$ has been detected). After that, we look at binaries with **different component masses** but the total mass fixed at $100M_{\odot}$. We vary the mass ratio q from 1 to 15.

Having generated all of the waveforms, similarly to what is done before, we Fourier transform them and lens them using the amplification functions displayed in figure 17 for the different lens masses. The dimensionless frequency ωM on figure 17 differs from ϖ (Eq.(112)) by a factor of 1/4 . After lensing all of the waveforms, both for the PML and BH models, we compute the **mismatch** between the **lensed** (or **scattered**, respectively) and the **unlensed** one. To facilitate the analysis, we consider only the cross polarization $h_{\times}$, despite the fact that both h_{+} and $h_{\times}$ undergo distinct lensing effects. In particular, the choice of physical setup from [10] and section 3.2 favors lensing effects on $h_{\times}$. This, naturally, only becomes consequential when analyzing the BH lens, since the PML affects both equally. Explicitly:

$$\text{Lensed waveform:} \quad h(f)^{l}_{+/\times} = F_{PML}(f)h(f)^{u}_{+/\times} \tag{113}$$

$$\text{Scattered waveform:} \quad h(f)^{s}_{+/\times} = \mathcal{F}_{BH}(f)h(f)^{u}_{+/\times} + \mathcal{G}_{BH}(f)h(f)^{u}_{\times/+} \tag{114}$$

In figure 21 we show the mismatch between the **scattered and unlensed** waveforms, for all 10 of the lens masses in terms of binary mass. It is visible that all of these values are small, compared to the previous section 4.2.1, which is to be expected at such a large impact parameter - $y = 2.69$. Furthermore, one should bear in mind that all of these values have been minimized over time delay. However, all of the lines show different qualitative behaviors, and still show that the changes to the waveforms are measurable and visible. As a reference, we show in figure 22 a couple of these lines plotted against the mismatch between **lensed and unlensed** waveforms, to compare a BH versus a PML model. Finally, we will look at some individual cases to better understand the tendencies in the mismatch.

We can see that, despite being at such a large impact parameter, the PML model still shows a relatively large mismatch, more so than the BH scattered waveforms for most of the cases - see figure 22. However, the black hole scattering mismatches show qualitative features different from the point mass lens, rendering them more "interesting".

The **first noticeable feature** is that for $M_L = 70M_{\odot}$ we can see that the mismatch has much smaller values overall. This can be explained due to the fact that this particular mass is, in many cases, smaller than the mass of the binary (from $m_1 = 35M_{\odot}$ onward). This will lead the lens to become "invisible" to the waveform, which has a size larger than it, placing us in the **deep wave optics regime**. Therefore, as we move along the x axis of the $M_L = 70M_{\odot}$ line of both figures 21 and 22, the mismatch very quickly decreases, reaching almost zero for the BH case.

For the PML model, the mismatches change very little, which, to some extent, can also be observed in the BH lens case. In particular, for the BH case, it seems that for $M_L = 300M_{\odot}$ onward, all of the lines seem to blend into very similar mismatch values, even for lower binary mass values. In other words, **when we enter the geometric optics regime for the black hole lens, the mismatches all merge and acquire very small values due to absorption** . For the PML, because we are at too high of an impact parameter to form distinct images, the mismatch also remains approximately constant.

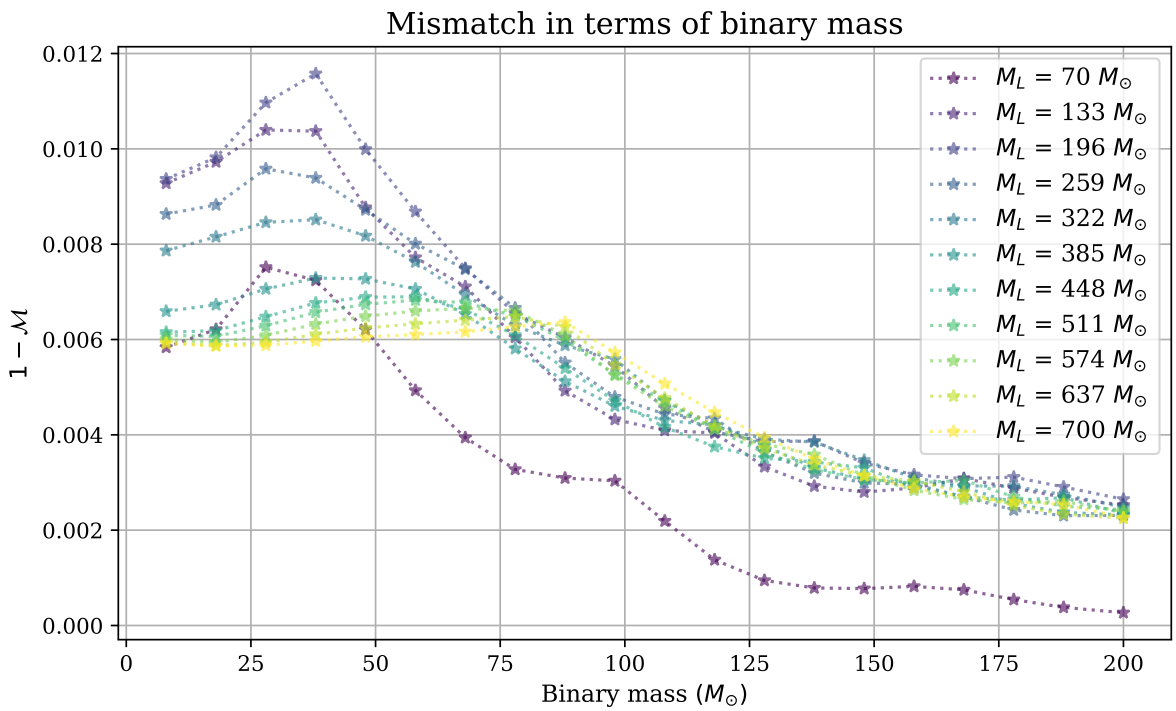

Figure 21: Mismatch between the original and scattered waveforms for equal mass binaries. Each one of the 10 colors is a different lens mass. The scattered waveforms are the ones to which $\mathcal{F}$ and $\mathcal{G}$ from Eq.(104) are applied.

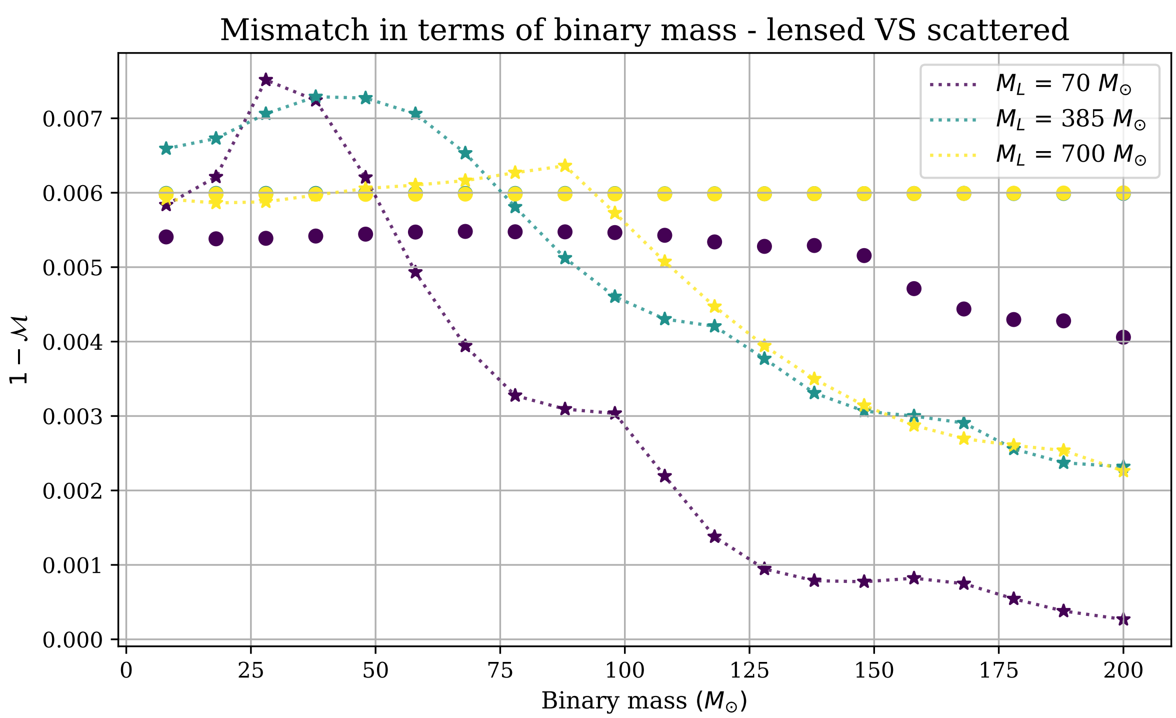

Figure 22: Mismatch between for equal mass binaries, for 3 lens mass values. The dashed lines with stars are the scattered waveforms (BH lens - Eq.(104)) and the dots are the lensed waveforms (PML - Eq.(61)).

The **lens masses that cover the wave optics regime**, which should be higher than $70M_\odot$ but lower than $300M_\odot$, **seem to peak at lower binary mass values before decreasing**, and the peak seems to be shifting along the x axis as we increase lens mass values. This could be caused by the beating pattern observed in the $\mathcal{F}$ and $\mathcal{G}$ amplification factors right before $\omega M \sim 1$ - see figure 17. This is a plausible explanation due to the fact that for those particular lens and binary masses, we are close enough to having $\omega M \sim 1$ (the size of the wave is majorly set by the size of the binary, off by some factors, therefore it is still possible to be in this regime despite the binary and lens masses not being exactly equal).

To further understand the different behaviors in the mismatch, we look at some cases individually: in figure 23, we show the waveforms with the maximum mismatch for the BH lens, which is achieved for a **binary mass of** $38M_{\odot}$ **and lens mass of** $196M_{\odot}$; and in figure 24, we show the smallest mismatch for a fixed lens mass of $700M_{\odot}$ - which , however, is not the minimum overall - achieved for a binary mass of $200M_{\odot}$.

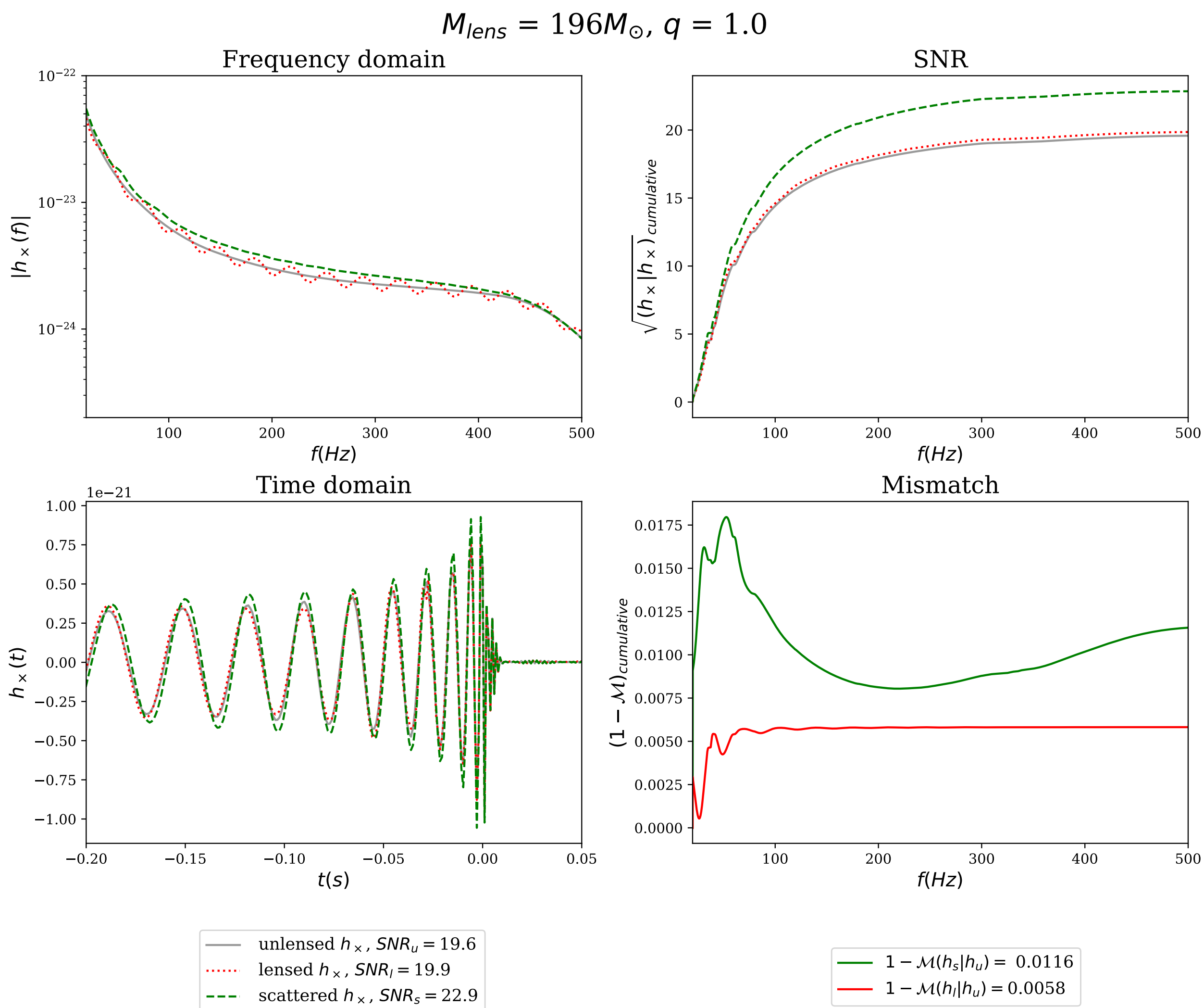

Figure 23: Looking at the individual case where the mismatch of the scattered waveform is maximum, which happens for a binary mass of $38M_{\odot}$ and a lens mass of $M_L = 196M_{\odot}$. The green line is the scattered waveform, and the red line is the lensed one. The layout is the same as figure 20 for the 4 panels.

In figure 23, we notice that the mismatch very quickly accumulates at low frequency values of the waveform, and then takes a "dip". This is caused because the early stages of the waveform are placed in the wave optics regime, which can be confirmed by looking at the time domain waveform. **In the early stages of the merger, the green line shows a slight amplification and a visible time shift, and the latter causes the mismatch to maximize for low frequencies.** The observed minimum is achieved when the dimensionless frequency starts approaching the geometric optics regime, but before absorption by the black hole begins to play a role. We can still see some slight amplification but no overall distortion on the waveforms, which is why the mismatch decreases.

On the other hand, figure 24 shows a different behavior. The waveform in frequency domain spans over much less frequency values than figure 23 - as one can see, it doesn't necessarily reach smaller frequencies than the one in figure 23, it simply fails to reach higher ones. This means that, even in dimensionless frequency, the wave spans over a much shorter frequency range. This will lead the mismatch to accumulate for a limited range of frequencies, making it smaller overall. However if, perhaps, this small range was in an earlier region of the x axis of figure 17, the mismatch would be able to reach higher values because it would be deeper in the optics regime. However, that behavior is hard to observe in figure 21 since all of the different lines are relatively concentrated around the same values.

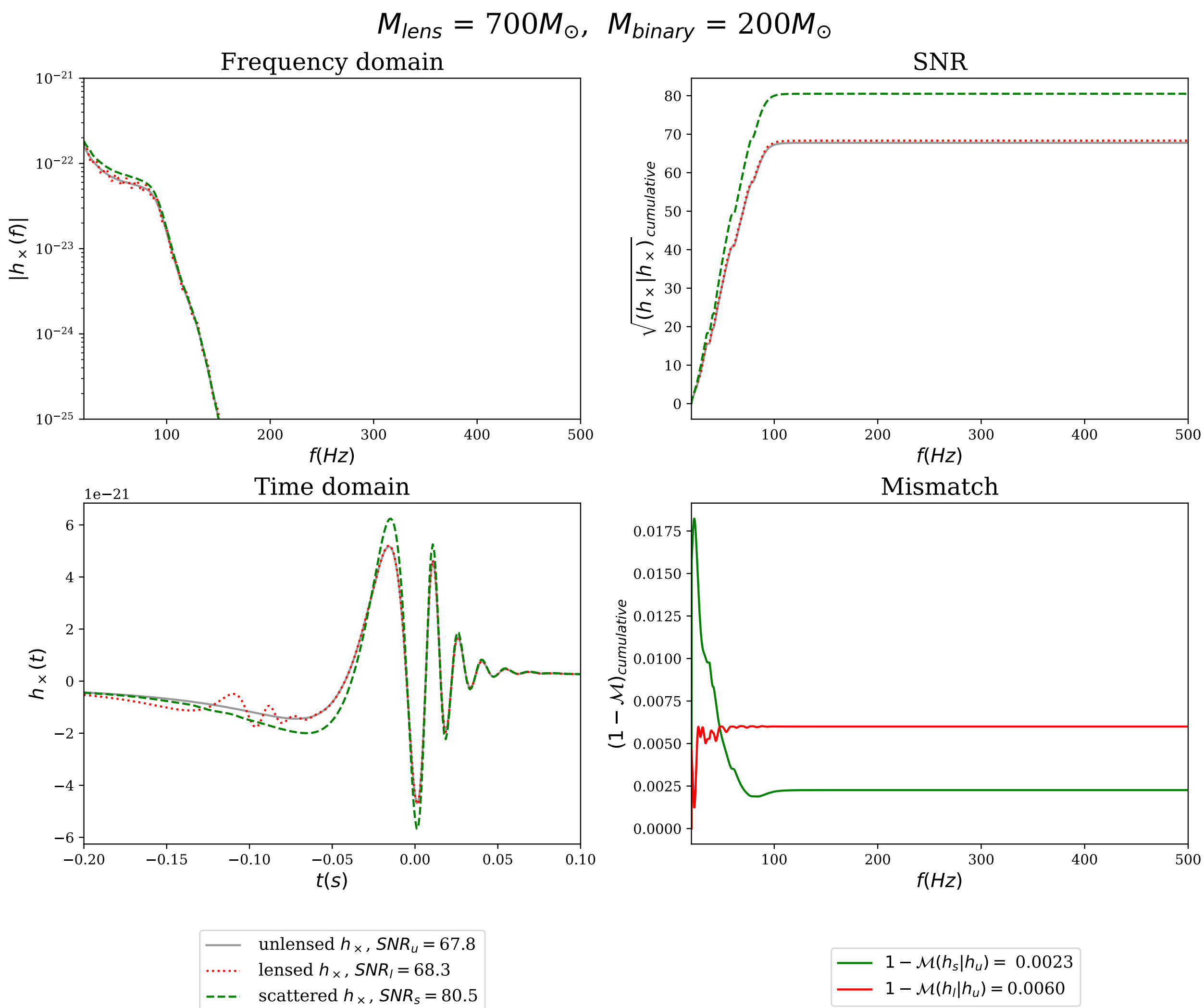

Figure 24: Looking at the individual case where the mismatch of the scattered waveform is minimum for a lens mass of $700M_{\odot}$, which happens for a binary mass of $200M_{\odot}$. The green dashed line is the scattered waveform, and the red dotted one is the lensed one. The layout is exactly the same as figure 23, except for a different waveform.

Essentially, there are more factors at play in the mismatch between scattered and lensed waveforms than one expects.

First and foremost, **more proeminent lensing signatures for the scattered waveforms are expected in the wave optics regime** (early ωM), since in geometric optics there is absorption. This is already a behavior exclusive to a black hole lens, since in the point mass lens approximation we found that highest mismatches are in the geometric optics regime, when different images interfere. However, if the lens mass is set to be too small, placing us in the **deep wave optics** regime, the wave travels virtually unaffected.

Secondly, for **the same binary mass**, except for the single case of $M_L = 70M_{\odot}$, we notice that the **mismatch seems**

to be smaller for higher lens masses. This is understood since changing the lens mass alone will define where in ωM the waveform is spanning over, and for higher lens masses, we start approaching geometric optics, which means, for a BH lens, absorption.

Lastly, as we move along the x axis in figures 21 and 22, the waveforms are much shorter bursts, unable to reach as high values of frequency. This means that the lens mass plays a very important role: if the range of ωM is very short, then the placement of that range will define if the wave will be distorted or absorbed. At high binary masses, all of the lines in figure 21 seem to blend, making it hard to distinguish this kind of behavior. In this case, **the fact that the signal is short "dominates" over whether we are in wave optics or geometric optics**. As we can see from figure 24, the mismatch peaks at a value as high as the one from 23. However, the mismatch stops accumulating at frequency values where we no longer have a strain, which causes it to acquire a much smaller value.

Having looked at equal mass binaries, **we now turn our attention to binaries with a mass ratio $q \neq 1$.** Fixing the total binary mass at $100M_\odot$ will lead to the waveform always having the same range of frequency values. The only change that we can actually enforce is how the strain is distributed within that same frequency range.

Essentially, a waveform is a superposition of several spherical modes. The same way that, in section 3.2, we decompose the incoming waveform into spherical modes centered around the lens, a GW can be decomposed into different modes centered around the source - binary. The properties of the binary will set how much each of these spherical modes will weigh into the final waveform. For more symmetric binaries, the $(\ell, m) = (2, 2)$ mode has a crushing contribution when compared to all the others. However, for more asymmetric binaries, other modes become more relevant. In short, **as we increase the mass ratio of the binary the waveforms become more "irregular".**

Similarly to what was done for equal mass binaries, we show in figure 25 the mismatch between the scattered and unlensed waveforms, for all 10 lens masses, as a function of mass ratio. In figure 26, we show a comparison with the PML model for three different lens masses.

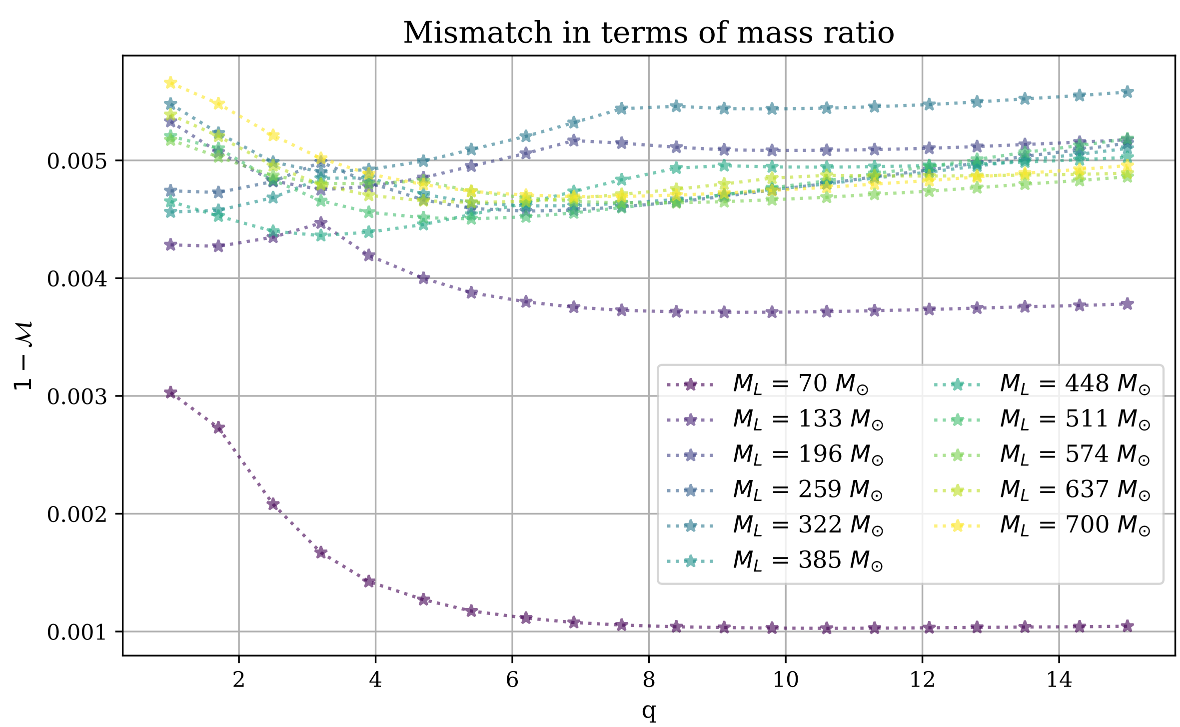

Figure 25: Mismatch between the original and scattered waveforms for different component mass binaries. Each one of the 10 colors is a different lens mass. These are the waveforms to which $\mathcal{F}$ and $\mathcal{G}$ from Eq.(104) are applied.

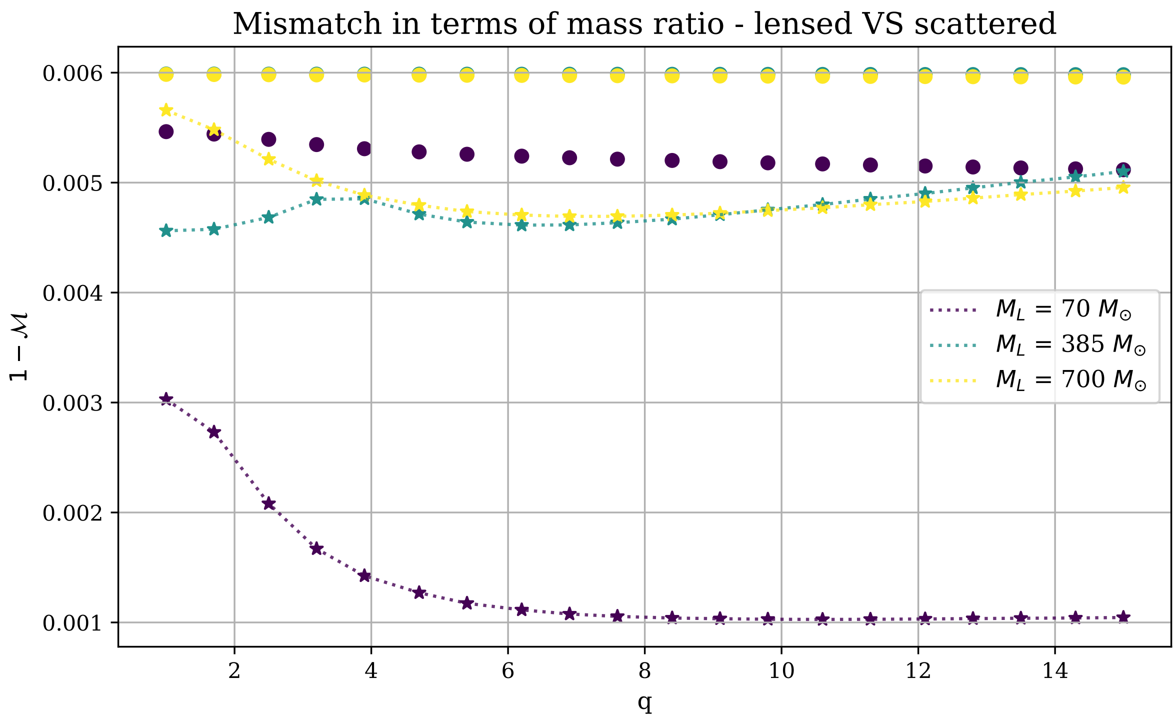

Figure 26: Mismatch between for different component masses binaries, for 3 lens mass values. The **dashed lines with stars are the scattered waveforms** (BH lens - Eq.(104)) and the **dots are the lensed waveforms** (PML - Eq.(61)). Each color is a different lens mass.

When compared to how much the mismatch changes with binary mass, the **mismatch as a function of mass ratio remains almost constant** for the scattered waveforms. For the PML model, it remains perfectly constant, fixed at $1-\mathcal{M} = 0.006$, as can be seen from figure 26. Once again, the mismatch for a lens mass of $M_L = 70M_\odot$ is significantly smaller than all the other ones, simply because we find ourselves in the deep wave optics regime - see figures 25 and 26. To understand whether there is a tendency in the mismatch that is specifically caused by the mass ratio, we will look at the individual case in which the mismatch is maximum, which is for $q = 15.0$ for a lens mass of $M_L = 322M_\odot$.

As we can see, the frequency domain strain of the original signal looks different from the ones we have observed for equal mass binaries. However, since the intensity of the strain and the frequency range is the same as it would be for equal mass binaries, one can only conclude that **the mass ratio of the binary source plays very little role on how the waveform will be lensed and/or scattered.** The reason that the maximum value of mismatch for this particular analysis is obtained for the configuration showed in figure 27 could be a spurious event. One possible explanation is, however, that the early frequency stages of the waveform could coincide with the beating patterns on the amplification functions of the black hole. It is still not enough to explain the increase of the line for $M_L = 322M_\odot$ altogether.

To properly evaluate the validity of this statement, further research would be needed. In particular, the study of a physical setup were lensing effects are more prominent would, perhaps, shed some light on these and other lingering questions regarding lensing in strong gravity. However, as far as this project goes, we are bound by a system that doesn't allow to probe very small impact parameters and very large lens masses.

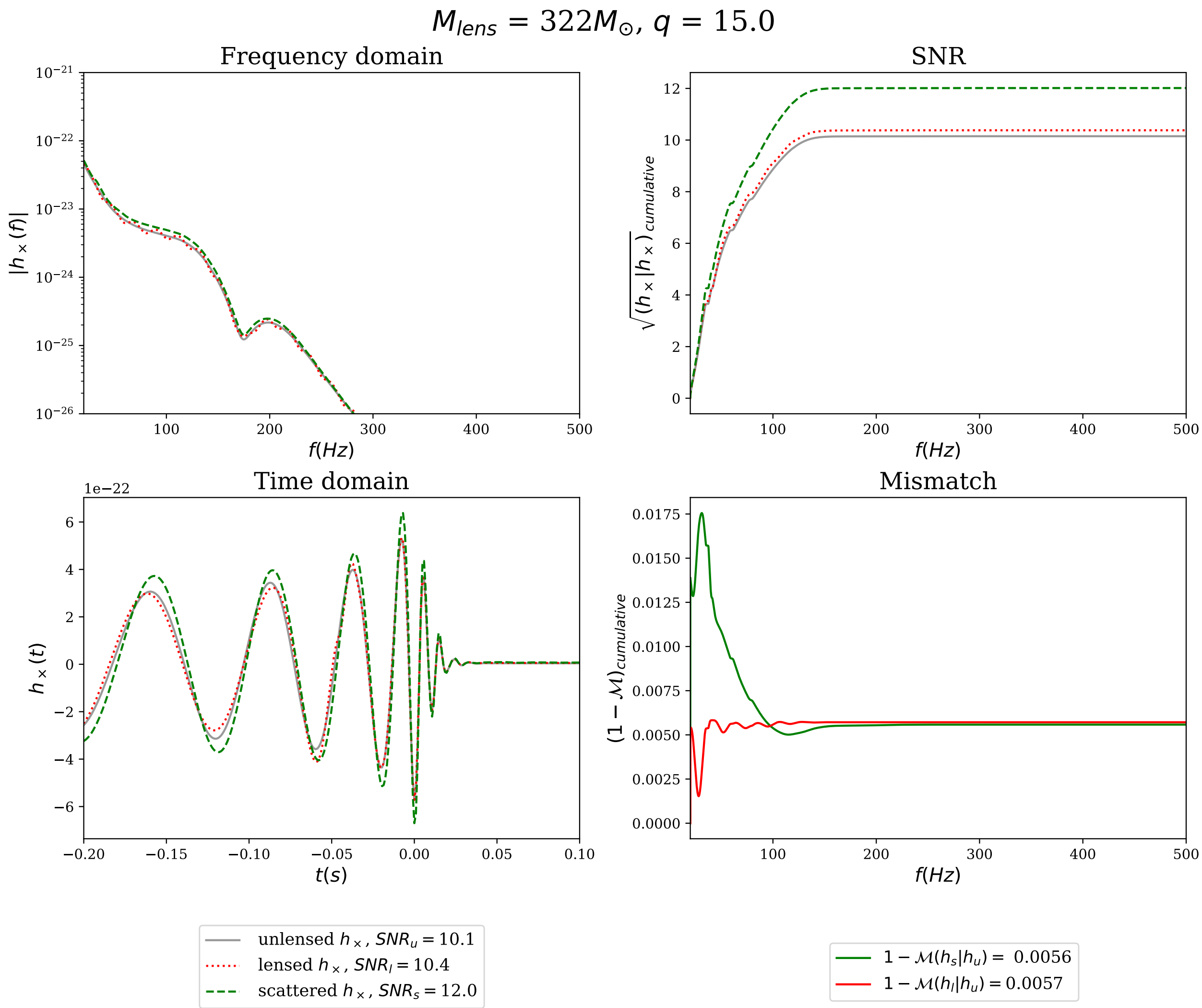

Figure 27: Looking at the individual case where the mismatch of the scattered waveform is maximum, which happens for a binary mass ratio of 15 and a lens mass of $M_L = 322M_{\odot}$. The green dashed line is the scattered waveform, and the red dotted one is the lensed one. The layout is the same as figures 20, 23, 24 for the 4 panels.

5 Discussion

This project investigates how gravitational waves propagate in the presence of different lenses/mass distributions. We start by introducing all of the different lensing **regimes**, which are set by three main parameters - recall figure 4:

- the dimensionless frequency ωM - size of the wave compared to the lens - defines wether we are in geometric or wave optics;
- the nature of the lens - wether we consider it to be have a strong gravitational potential that deeply curves the space-time around it, or if we use the weak gravity approximation - strong versus weak gravity;
- the impact parameter of the source position with respect to the line of sight that connects the observer (us) to the lens - strong VS weak lensing (this particular terminology is only used to describe the geometric optics regime based on how many images are produced, but the impact parameter also affects how the wave is lensed in wave optics).

Before dwelling into all of the regimes, we show how **gravitational wave propagation** is analytically described from Einstein's General Relativity - section 1.2. Supposing a particular background metric, gravitational waves are described as a small perturbation for which one only consider linear orders in amplitude. To study their propagation, we solve Einstein's field equations for the first order perturbed Ricci tensor in vacuum and arrive at a form of a wave equation - Eq.(9). This equation fully describes how a perturbation of the first order propagates in an arbitrarily curved background metric. Knowing that curvature in the metric is induced by the presence of mass, then the nature/compactness of the lens will set how curved the background metric is.

5.1 Weak gravity lensing

Starting off, in the **weak gravity approximation** , the propagation equation is solved for a nearly flat metric except for the presence of a Newtonian potential, which slightly curves it very locally - Eq.(19). This kind of potential is a very good approximation for a number of systems: galaxies, which are very massive but very disperse in radii - section 2.3.3; stars, which are compact but still well enough described by a point mass; or, even for black holes, which are very compact objects, if the wave propagates far enough from it - section 2.3.2. Under this formalism, **the gravitational wave is treated as a scalar**. We arrive at an integral expression - **diffraction integral** - Eq.(36) - that encapsulates the information of how the gravitational wave is lensed according to different lens models. Solving this integral yields **amplification functions** that are applied to a Fourier transformed waveform to get a lensed gravitational wave.

For high enough dimensionless frequencies, this integral becomes too oscillatory and it is solved using the stationary phase approximation, which places us in the **geometric optics regime**. It is very familiar since it's how we describe the lensing of light waves - section 2.2. In this regime:

- we can obtain the **lens equation** - Eq.(39) - which tells us the position of the images given a certain source position and deflection angle created by the gravitational potential, which is controlled by the choice of lens model;
- the amplification function is given as a sum of **discrete images** that arrive at different times, each with a different magnification - Eq.(46);
- if the time delay between the images is not large enough, they interfere and heavily distort the final waveform - see blue line in figure 20.

However, for lower frequencies, geometric optics breaks down. For a certain range of frequencies, it is possible to rectify this without solving the diffraction integral in full, which becomes quite challenging for more complex lens models - section 2.2.1. This is done simply by accounting for higher orders in the Taylor expansion of the Time delay surface. These **beyond geometric optics corrections** successfully make the geometric optics approximation better converge with the analytical solution for a range of dimensionless frequency values that is in between deep wave optics and full geometric optics - figure 9.

Lastly, when the dimensionless frequency is lower, we are in the **wave optics regime** and are forced to solve the diffraction integral in full, analytically. We find that for lens models which have an axially symmetric 2-D projected potential - section 2.3.1, the diffraction integral greatly simplifies, and the lens equation turns into a scalar one, meaning the source and images are all along one axis (instead of a plane, which is the usual case) - figure 8. Furthermore, by looking at two very familiar lens model - point mass (section 2.3.2) and singular isothermal sphere (section 2.3.3) - we predict amplifications up to order 14 - figure 10 - in the vicinity of caustics (low impact parameters).

After laying out the theoretical foundations of the weak gravity approximation, the amplification functions from a point mass lens model are applied to a waveform, for lens masses between 30 and 300 solar masses, and three impact parameters between 1 and 0.01. For smaller impact parameters, the waveforms are, in the wave optics regime, largely amplified, which results in a **very high signal-to-noise ratio-** top right sub-panel of figure 20. In the geometric optics regime, the oscillations in the amplification functions cause the multiple images to **interfere and distort the waveform**- top and bottom left sub-panels of figure 20.

To quantify the changes in the waveform caused by the point mass lens model, we compute the **mismatch** between lensed and unlensed waveforms - Eq.(108). By definition, a mere amplification to the waveform (causing higher signal-to-noise) is not discernible in the mismatch. Furthermore, the mismatch is minimized over time delay, meaning that we shift the lensed waveform in time domain in order to coincide with the unlensed one as much as possible - figure 18. Nevertheless, we can get mismatches as high as 0.25 (it is usually between 0 and 1), meaning that, in some cases, **lensed waveforms can go by undetected due to the incompleteness of the current gravitational waveform model template banks, if their signal-to-noise is not high enough** - see figure 19.

There is a lot of future work to be done in weak gravity lensing, particularly in solving the diffraction integral for complicated lens models - [44, 46] and extending current templates to account for heavy distortions - [15, 11].

5.2 Strong gravity lensing

When studying lensing in **strong gravity**, the formalism is drastically different and the techniques used to describe the geometric optics and wave optics regime are also very distinct.

In **geometric optics**, a **short wave expansion**is performed. Essentially, we use the WKB technique of expanding the wave in amplitude with an exponential (phase), and solve for orders of that expansion. The amplitude of the wave is taken to change slowly with respect to the phase, valid when the wave has a small wavelength when compared to the scale of the background curvature. When solving Eq.(9) for the leading order of the expansion, we arrive at the condition for a **null geodesic** propagating in a background metric. Tracing geodesics is very well known in Schwarzschild metric, which is the case we focus on.

- We find that solving the geodesic equation in spherical coordinates leads to two constants of motion (through Euler-Lagrange equations), whose ratio is defined as the **impact parameter at infinity**.

- We also find that the equation of motion for the radial coordinate - Eq.(79) - resembles that of a particle subject to a **potential barrier**(figure 13). To overcome it, the trajectory of the geodesic needs to have a close approach distance (x_0) from the center of mass of the black hole larger than 1.5 Schwarzschild radii, which is where the maximum of the potential lies. This means that the impact parameter at infinity - Eq.(81) - must acquire a certain value larger than its critical one in order for the geodesic to not plunge directly into the black hole - see right hand side plot of figure 14.

- We also find that by tracking the motion of the angular coordinate ϕ, the **deflection angle** of the trajectory of the geodesic is obtained. We can, then, relate it to the **impact parameter**- recall the first panel of figure 14 and Eq.(83).

- We show how the relation between deflection angle and impact parameter can be used to trace the trajectory of gravitational waves emitted in Active Galactic Nuclei disks. In these disks, it is predicted that certain mechanisms ("migration traps") should lead binaries to migrate close to the central supermassive black hole, where they are expected to merge. For the rather theoretical disk model this is applied to, we find that sources located in the trap will mostly emit waves that directly plunge into the black hole - figure 16. However, in more outer regions, they could be lensed and deflected. It is worth to explore this for **more evolved disk and population models** as future work.

- Since the deflection angles are very often larger than 2π, the geodesic is expected to loop around the black hole which is, for light, what is known as the photon ring. In this case, it is useful to employ the logarithmic approximation -

Eq.(84) - in computing the deflection integral, to better resolve when exactly we have a direct plunge into the black hole, a "graviton" ring, or an extremely large deflection angle.

- It is also possible to define the deflection angles as deviations from 2π which should be small enough to follow the lens equation. We are therefore, able to predict the magnifications of the image for a given source position (or impact parameter), as well as their magnifications. Essentially, every time the wave loops around the black hole, it creates an image and they are progressively fainter.

In **wave optics**, due to lower wavelengths, it is no longer possible to resort to the short wave expansion. Therefore, we use black hole perturbation theory to solve the **scattering of the gravitational wave off a Schwarzschild black hole** - recall sections 1.3 and 3.2.

The scattering phenomena is described by the **Regge - Wheeler equation**, which arises from considering a background Scharzschild metric in the initially derived propagation equation Eq.(9). By preforming a separation of variables, we can describe the angular dependence in spin-2 tensor spherical harmonics ${}_2Y_{\ell m}$, and then the radial dependence of each of these **spherical modes** will be the solution to the Regge-Wheeler equation - Eq.(11). In order to solve our lensing problem, we take the solution to this equation at infinity, which is where the observer would be placed. This resulting radial function is taken to be as an outgoing wave scaled by the **black hole reflectivities** - see figure 5. These reflectivities are a function of the dimensionless frequency ωM between 0 and 1, for each (ℓ, m) mode. For higher ℓ modes, they go to 0 at much higher frequencies than for lower ℓ (for low frequencies, these reflectivities are always 1, meaning the wave is fully transmitted). Therefore, for shorter wavelengths, which account for higher ℓ modes, the wave gets **absorbed**, and we recover the geometric optics limit.

After having an understanding on how the black hole will affect the radial contributions of each spherical harmonic mode (ℓ, m), we still need to deconstruct the incoming gravitational wave and reconstruct the outgoing one according to these modes - section 3.2. To do so, we take the following steps, based off the methodology we developed in [10]:

- We write the incoming gravitational wave in the transverse traceless gauge and approximate it to a **plane wave** - Eq.(91) - which, for the distance source-lens we are considering, is a good enough approximation.

- We expand the spin eigen states $h_{(\pm 2)}$ into spherical harmonics centered around the lens, where the weight of each mode can be related to the Regge-Wheeler variables (of the lens) at infinity.

- We then apply the reflectivities to the outgoing piece of the wave, and rewrite the plane wave with the outgoing amplitude already being "lensed". This requires summing over all of the (ℓ, m) modes, which we found to be numerically challenging.

- We then add back the incoming piece of the wave to be able to write the final waveform analytically as the initial one times a scaling factor.

The first thing we are able to notice is that the final expression for each of the polarizations after being lensed has a contribution from the initial polarization by a factor $\mathcal{F}$, but also a contribution from the opposite one by a factor of $\mathcal{G}$ - Eq.(104). This means that, in strong gravity, we are able to capture **polarization mixing**. We also quickly found that for a particular choice of azimuthal angle $\phi = 0$, the polarization mixing term $\mathcal{G}$ vanishes, meaning that **polarization mixing is a phenomena fully caused by the tensorial treatment of the wave, not the black hole itself**. This follows logically from the fact that we are considering a spherically symmetric, non-rotating black hole. Applying this kind of methodology to, for example, Kerr metric, might yield very different results, but this will be left for future work.

Another clear feature of the amplification functions - see figure 17 - that is exclusive to the black hole lens, is the fact that the amplification factors go to zero at high frequencies, making the lensed and unlensed waveforms converge. This means that the part of the wave that hits the black hole (incoming) is **absorbed at higher dimensionless frequencies**. This is to be expected given the behavior of the black hole reflectivities at high ωM, and it's how we recover the results of section 3.1.

Having derived the **frequency dependent amplification factors** as done in lensing in weak gravity, we apply them to several waveforms, varying several parameters. For **equal mass binaries**, we change the total mass between 8 and $200 M_{\odot}$. For higher mass binaries, the waves are expected to be very short in time (one, maybe two oscillations before the merger) and very small in frequency - at least for the frequencies LIGO is sensitive to; for lower mass binaries, the opposite is true. For **different component masses binaries**, we fix the total mass at $100 M_{\odot}$ and change the mass ratio q from 1 to 15. For both of these analysis, we apply these waveforms to lens masses ranging from 70 to $700 M_{\odot}$ - which will convert the frequency of the wave into dimensionless frequencies, placing us either in the geometric or wave optics (or deep wave optics) regime.

After applying the amplification factors, we measure the mismatch between the scattered and unlensed waveforms, and we find several interesting tendencies.

- For a lens mass of $70 M_{\odot}$, we are in the deep wave optics regime, which causes the lens to be unnoticeable to the waveform, causing the mismatches to be much lower overall - figures 21, 25, 22 and 26.
- We notice that for higher binary masses, the mismatches are lower due to the fact that the waves are short in frequency space, causing the mismatch to accumulate over less frequency values - figure 23 versus 24.
- For higher lens masses, which place us in the geometric optics regime, the mismatches seem to all blend together and become very similar, meaning that absorption is playing an important role - both visible in figures 21 and 25.
- For lens masses that place us in the wave optics regime - between deep wave optics and geometric optics, the mismatches seem to peak at lower binary masses (the higher the lens mass, the later it peaks), which could be caused by the structure in the BH amplification factors at $\omega M \sim 1$ - figure 21.
- Lastly, we find that the mass ratio of the binary doesn't seem to affect the mismatch in an obvious way, meaning that, at least for the system we are considering, lensing seems to be independent on the mass ratio.

All of these findings are still rather limited by our choice of physical system, which yields the amplification factors for a black hole rather small. To further explore these effects, it is useful to try and overcome the numerical issues encountered in order to be able to probe smaller impact parameters (y in weak gravity, or θ in strong gravity). Furthermore, to make it more applicable to real, physical systems, it would be relevant future work to expand this methodology to rotating black holes, to see more intense effects on the final waveform caused by the polarization mixing. However, for lensing systems where accounting for strong gravity effects is important, **we can clearly see phenomenological differences between a black hole and, for example, a point mass lens model** (which would be applicable to, for example, a large star or a very distant black hole). The complex structure of black holes creates effects that weak gravity cannot account for, namely, the **polarization mixing** and **absorption of the gravitational wave .**

6 Acknowledgments

I want to start by expressing my deepest gratitude to my supervisor, Professor Jose María Ezquiaga. His unwavering support and exceptional guidance throughout the whole year have been invaluable. He went above and beyond simply overseeing my research project and provided me with the best opportunities a student could hope for to start a career in academia with the right foot forward. Working under his supervision has been a privilege, a pleasure, and a formative experience that I will always carry with the utmost appreciation.

I am also extremely grateful to all of the members of the Strong group. They have created an inclusive and thriving academic and social environment that has been crucial for me. Feeling so included and encouraged in this group will be something I will always remember and be grateful for. However, I want to give a special thank you to the members of the Gravitational Wave explorers, and the participants of Lenshouse. Rico Lo, Lorena Zertuche, Juno Chan, Luka Vujeva, Jaime Redondo-Yuste and Conor Dyson have been indispensable to me and to my project. The academic discussions, as well as personal insights on all of the obstacles I have faced throughout the year have been invaluable to me. I want to thank them for being such amazing colleagues and friends. I also want to acknowledge the Niels Bohr International Academy, which is where my research journey started, and with a special heartfelt gratitude to Astronomer Daniel D'Orazio, who supervised my thesis preparation project and helped me throughout this year.

I also want to acknowledge my good friends from the Niels Bohr Institute - Maya Merchant, Freja Nørby, Anna Manou and Ruza Markovic, who have been truly an unwavering and reliable source of support that I cannot appreciate enough.

I also want to thank my parents and brother, who gave me the strength and inspiration I needed to pursue a Master's abroad, and have been my biggest support, always.

Lastly, I want to express my deepest gratitude to my grandparents, Professor Arnaldo Pereira and Professor Maria Helena Serôdio, to whom I dedicate this thesis. They have always inspired and pushed me to pursue my dreams, and it is thanks to them that I have gotten this far.

References

[1] B. P. Abbott et al. “GW150914: First results from the search for binary black hole coalescence with Advanced LIGO”. In: *Physical Review D* 93.12 (June 2016). ISSN: 2470-0029. DOI: 10.1103/physrevd.93.122003. URL: http://dx.doi.org/10.1103/PhysRevD.93.122003.

[2] B. P. Abbott et al. “Properties of the Binary Black Hole Merger GW150914”. In: *Phys. Rev. Lett.* 116 (24 June 2016), p. 241102. DOI: 10.1103/PhysRevLett.116.241102. URL: https://link.aps.org/doi/10.1103/PhysRevLett.116.241102.

[3] Lars Andersson, Jérémie Joudioux, Marius A. Oancea, and Ayush Raj. “Propagation of polarized gravitational waves”. In: *Phys. Rev. D* 103 (4 Feb. 2021), p. 044053. DOI: 10.1103/PhysRevD.103.044053. URL: https://link.aps.org/doi/10.1103/PhysRevD.103.044053.

[4] Jillian M. Bellovary, Mordecai-Mark Mac Low, Barry McKernan, and K. E. Saavik Ford. “MIGRATION TRAPS IN DISKS AROUND SUPERMASSIVE BLACK HOLES”. In: *The Astrophysical Journal Letters* 819.2 (Mar. 2016), p. L17. ISSN: 2041-8213. DOI: 10.3847/2041-8205/819/2/l17. URL: http://dx.doi.org/10.3847/2041-8205/819/2/L17.

[5] *Black Hole Perturbation Toolkit*. (bhptoolkit.org).

[6] V. Bozza. “Gravitational lensing in the strong field limit”. In: *Physical Review D* 66.10 (Nov. 2002). ISSN: 1089-4918. DOI: 10.1103/physrevd.66.103001. URL: http://dx.doi.org/10.1103/PhysRevD.66.103001.

[7] V. Bozza, S. Capozziello, G. Iovane, and G. Scarpetta. “Strong Field Limit of Black Hole Gravitational Lensing”. In: *General Relativity and Gravitation* 33.9 (Sept. 2001), pp. 1535–1548. ISSN: 1572-9532. DOI: 10.1023/a:1012292927358. URL: http://dx.doi.org/10.1023/A:1012292927358.

[8] Ginevra Braga, Alice Garoffolo, Angelo Ricciardone, Nicola Bartolo, and Sabino Matarrese. *Proper time path integrals for gravitational waves: an improved wave optics framework*. 2024. arXiv: 2405.20208 [astro-ph.CO]. URL: https://arxiv.org/abs/2405.20208.

[9] Vitor Cardoso, Alex S. Miranda, Emanuele Berti, Helvi Witek, and Vilson T. Zanchin. “Geodesic stability, Lyapunov exponents, and quasinormal modes”. In: *Phys. Rev. D* 79 (6 Mar. 2009), p. 064016. DOI: 10.1103/PhysRevD.79.064016. URL: https://link.aps.org/doi/10.1103/PhysRevD.79.064016.

[10] Juno C. L. Chan, Conor Dyson, Matilde Garcia, Jaime Redondo-Yuste, and Luka Vujeva. *Lensing and wave optics in the strong field of a black hole*. 2025. arXiv: 2502.14073 [gr-qc]. URL: https://arxiv.org/abs/2502.14073.

[11] Juno C. L. Chan, Eungwang Seo, Alvin K. Y. Li, Heather Fong, and Jose M. Ezquiaga. “Detectability of lensed gravitational waves in matched-filtering searches”. In: *Physical Review D* 111.8 (Apr. 2025). ISSN: 2470-0029. DOI: 10.1103/physrevd.111.084019. URL: http://dx.doi.org/10.1103/PhysRevD.111.084019.

[12] Lester A. Edelstein and C. V. Vishveshwara. “Differential Equations for Perturbations on the Schwarzschild Metric”. In: *Phys. Rev. D* 1 (12 June 1970), pp. 3514–3517. DOI: 10.1103/PhysRevD.1.3514. URL: https://link.aps.org/doi/10.1103/PhysRevD.1.3514.

[13] LUTHER PFAHLER EISENHART. *Riemannian Geometry*. Princeton University Press, 1997. URL: http://www.jstor.org/stable/j.ctt1cx3vd7 (visited on 04/17/2025).

[14] José María Ezquiaga. “Black Holes and Gravitational Waves”. Lecture notes, Niels Bohr Institute, University of Copenhagen. Sept. 2023.

[15] Jose María Ezquiaga, Rico K. L. Lo, and Luka Vujeva. “Diffraction around caustics in gravitational wave lensing”. In: (Mar. 2025). arXiv: 2503.22648 [gr-qc].

[16] Valeria Ferrari and Bahram Mashhoon. “New approach to the quasinormal modes of a black hole”. In: *Phys. Rev. D* 30 (2 July 1984), pp. 295–304. DOI: 10.1103/PhysRevD.30.295. URL: https://link.aps.org/doi/10.1103/PhysRevD.30.295.

[17] Richard Phillips Feynman and Albert Roach Hibbs. *Quantum mechanics and path integrals*. International series in pure and applied physics. New York, NY: McGraw-Hill, 1965. URL: https://cds.cern.ch/record/100771.

[18] Samuel E. Gralla, Daniel E. Holz, and Robert M. Wald. “Black hole shadows, photon rings, and lensing rings”. In: *Physical Review D* 100.2 (July 2019). ISSN: 2470-0029. DOI: 10.1103/physrevd.100.024018. URL: http://dx.doi.org/10.1103/PhysRevD.100.024018.

[19] Zoltán Haiman, Zoltan Haiman, Bence Kocsis, Bence Kocsis, Kristen Menou, and Kristen Menou. “The Population of Viscosity- and Gravitational Wave-Driven Supermassive Black Hole Binaries Among Luminous AGN”. In: *Astrophys. J.* 700 (2009). [Erratum: Astrophys.J. 937, 129 (2022)], pp. 1952–1969. DOI: 10.1088/0004-637X/700/2/1952. arXiv: 0904.1383 [astro-ph.CO].

[20] Abraham I. Harte and Marius A. Oancea. “Spin Hall effects and the localization of massless spinning particles”. In: *Phys. Rev. D* 105 (10 May 2022), p. 104061. DOI: 10.1103/PhysRevD.105.104061. URL: https://link.aps.org/doi/10.1103/PhysRevD.105.104061.

[21] Richard A. Isaacson. “Gravitational Radiation in the Limit of High Frequency. I. The Linear Approximation and Geometrical Optics”. In: *Phys. Rev.* 166 (5 Feb. 1968), pp. 1263–1271. DOI: 10.1103/PhysRev.166.1263. URL: https://link.aps.org/doi/10.1103/PhysRev.166.1263.

[22] Calvin Leung, Dylan Jow, Prasenjit Saha, Liang Dai, Masamune Oguri, and Léon V. E. Koopmans. *Wave Mechanics, Interference, and Decoherence in Strong Gravitational Lensing*. 2023. arXiv: 2304.01202 [astro-ph.HE]. URL: https://arxiv.org/abs/2304.01202.

[23] LIGO Scientific Collaboration, Virgo Collaboration, and KAGRA Collaboration. *LVK Algorithm Library - LALSuite*. Free software (GPL). 2018. DOI: 10.7935/GT1W-FZ16.

[24] Rico K. L. Lo, Luka Vujeva, Jose María Ezquiaga, and Juno C. L. Chan. “Observational Signatures of Highly Magnified Gravitational Waves from Compact Binary Coalescence”. In: *Phys. Rev. Lett.* 134 (15 Apr. 2025), p. 151401. DOI: 10.1103/PhysRevLett.134.151401. URL: https://link.aps.org/doi/10.1103/PhysRevLett.134.151401.

[25] Karl Martel and Eric Poisson. “Gravitational perturbations of the Schwarzschild spacetime: A practical covariant and gauge-invariant formalism”. In: *Physical Review D* 71.10 (May 2005). ISSN: 1550-2368. DOI: 10.1103/physrevd.71.104003. URL: http://dx.doi.org/10.1103/PhysRevD.71.104003.

[26] Norihito Matsunaga and Kazuhiro Yamamoto. “The finite source size effect and wave optics in gravitational lensing”. In: *Journal of Cosmology and Astroparticle Physics* 2006.01 (Jan. 2006), pp. 023–023. ISSN: 1475-7516. DOI: 10.1088/1475-7516/2006/01/023. URL: http://dx.doi.org/10.1088/1475-7516/2006/01/023.

[27] Maarten van de Meent. “Black Holes and Gravitational Waves”. Lecture notes, April 2024. Apr. 2024.

[28] Y. Mellier et al. “Euclid. I. Overview of the Euclid mission”. In: (May 2024). arXiv: 2405.13491 [astro-ph.CO].

[29] C. W. Misner, K. S. Thorne, and J. A. Wheeler. *Gravitation*. Ed. by Misner, C. W., Thorne, K. S., & Wheeler, J. A. 1973.

[30] V. Moncrief. “Gravitational perturbations of spherically symmetric systems. I. The exterior problem.” In: *Annals Phys.* 88 (1974), pp. 323–342. DOI: 10.1016/0003-4916(74)90173-0.

[31] T. T. Nakamura and S. Deguchi. “Wave Optics in Gravitational Lensing”. In: *Progress of Theoretical Physics Supplement* 133 (Jan. 1999), pp. 137–153. DOI: 10.1143/PTPS.133.137.

[32] Alex Nitz, Ian Harry, Duncan Brown, Christopher M. Biwer, Josh Willis, Tito Dal Canton, Collin Capano, Thomas Dent, Larne Pekowsky, Gareth S Cabourn Davies, Soumi De, Miriam Cabero, Shichao Wu, Andrew R. Williamson, Bernd Machenschalk, Duncan Macleod, Francesco Pannarale, Prayush Kumar, Steven Reyes, dfinstad, Sumit Kumar, Márton Tápai, Leo Singer, Praveen Kumar, veronica-villa, maxtrevor, Bhooshan Uday Varsha Gadre, Sebastian Khan, Stephen Fairhurst, and Arthur Tolley. *gwastro/pycbc: v2.3.3 release of PyCBC*. Version v2.3.3. Jan. 2024. DOI: 10.5281/zenodo.10473621. URL: https://doi.org/10.5281/zenodo.10473621.

[33] Marius A. Oancea, Richard Stiskalek, and Miguel Zumalacárregui. “Frequency- and polarization-dependent lensing of gravitational waves in strong gravitational fields”. In: *Physical Review D* 109.12 (June 2024). ISSN: 2470-0029. DOI: 10.1103/physrevd.109.124045. URL: http://dx.doi.org/10.1103/PhysRevD.109.124045.

[34] Martin Pijnenburg, Giulia Cusin, Cyril Pitrou, and Jean-Philippe Uzan. *Wave optics lensing of gravitational waves: theory and phenomenology of triple systems in the LISA band*. 2024. arXiv: 2404.07186 [gr-qc]. URL: https://arxiv.org/abs/2404.07186.

[35] Cyril Pitrou and Thiago S. Pereira. “Beyond scalar, vector, and tensor harmonics in maximally symmetric three-dimensional spaces”. In: *Phys. Rev. D* 100 (12 Dec. 2019), p. 123535. DOI: 10.1103/PhysRevD.100.123535. URL: https://link.aps.org/doi/10.1103/PhysRevD.100.123535.

[36] Eric Poisson and Misao Sasaki. “Gravitational radiation from a particle in circular orbit around a black hole. V. Black-hole absorption and tail corrections”. In: *Physical Review D* 51.10 (May 1995), pp. 5753–5767. ISSN: 0556-2821. DOI: 10.1103/physrevd.51.5753. URL: http://dx.doi.org/10.1103/PhysRevD.51.5753.

[37] Tullio Regge and John A. Wheeler. “Stability of a Schwarzschild singularity”. In: *Phys. Rev.* 108 (1957), pp. 1063–1069. DOI: 10.1103/PhysRev.108.1063.

[38] Peter Schneider, Jürgen Ehlers, and Emilio E. Falco. *Gravitational Lenses*. 1992. DOI: 10.1007/978-3-662-03758-4.

[39] *Spin Weighted Spherical Harmonics*. (AngularModes).

[40] Teruaki Suyama, Ryuichi Takahashi, and Shugo Michikoshi. “Wave propagation in a weak gravitational field and the validity of the thin lens approximation”. In: *Physical Review D* 72.4 (Aug. 2005). ISSN: 1550-2368. DOI: 10.1103/physrevd.72.043001. URL: http://dx.doi.org/10.1103/PhysRevD.72.043001.

[41] Ryuichi Takahashi. “Quasigeometrical optics approximation in gravitational lensing”. In: *Astron. Astrophys.* 423 (2004), pp. 787–792. DOI: 10.1051/0004-6361:20040212. arXiv: astro-ph/0402165.

[42] Ryuichi Takahashi and Takashi Nakamura. “Wave Effects in the Gravitational Lensing of Gravitational Waves from Chirping Binaries”. In: *The Astrophysical Journal* 595.2 (Oct. 2003), pp. 1039–1051. ISSN: 1538-4357. DOI: 10.1086/377430. URL: http://dx.doi.org/10.1086/377430.

[43] Giovanni Tambalo, Miguel Zumalacárregui, Liang Dai, and Mark Ho-Yeuk Cheung. “Lensing of gravitational waves: Efficient wave-optics methods and validation with symmetric lenses”. In: *Phys. Rev. D* 108 (4 Aug. 2023), p. 043527. DOI: 10.1103/PhysRevD.108.043527. URL: https://link.aps.org/doi/10.1103/PhysRevD.108.043527.

[44] Hector Villarrubia-Rojo, Stefano Savastano, Miguel Zumalacárregui, Lyla Choi, Srashti Goyal, Liang Dai, and Giovanni Tambalo. "GLoW: novel methods for wave-optics phenomena in gravitational lensing". In: (Sept. 2024). arXiv: 2409.04606 [gr-qc].

[45] C. V. Vishveshwara. "Stability of the Schwarzschild Metric". In: *Phys. Rev. D* 1 (10 May 1970), pp. 2870–2879. DOI: 10.1103/PhysRevD.1.2870. URL: https://link.aps.org/doi/10.1103/PhysRevD.1.2870.

[46] Luka Vujeva, Jose María Ezquiaga, Rico K. L. Lo, and Juno C. L. Chan. "Effects of Galaxy Cluster Structure on Lensed Transients". In: (Jan. 2025). arXiv: 2501.02096 [astro-ph.CO].

[47] Robert M. Wald. *General Relativity*. The University of Chicago Press, 1984.

[48] Fei Xu, Jose María Ezquiaga, and Daniel E. Holz. "Please Repeat: Strong Lensing of Gravitational Waves as a Probe of Compact Binary and Galaxy Populations". In: *The Astrophysical Journal* 929.1 (Apr. 2022), p. 9. ISSN: 1538-4357. DOI: 10.3847/1538-4357/ac58f8. URL: http://dx.doi.org/10.3847/1538-4357/ac58f8.

[49] Chengjiang Yin and Jian-hua He. "Detectability of Single Spinless Stellar-Mass Black Holes through Gravitational Lensing of Gravitational Waves with Advanced LIGO". In: *Physical Review Letters* 132.1 (Jan. 2024). ISSN: 1079-7114. DOI: 10.1103/physrevlett.132.011401. URL: http://dx.doi.org/10.1103/PhysRevLett.132.011401.

[50] Frank J. Zerilli. "Effective potential for even parity Regge-Wheeler gravitational perturbation equations". In: *Phys. Rev. Lett.* 24 (1970), pp. 737–738. DOI: 10.1103/PhysRevLett.24.737.

A Computing the first order perturbed Ricci tensor $R^{(1)}_{\mu\nu}$

For this derivation, one can follow chapter 3.2 of the lecture notes [27], section 7.5 of the book [47] or even the original derivation, first done by the mathematician Eisenhart - [13].

In order to compute the first order perturbation of the Ricci tensor, we first have to trace back to the Riemann curvature tensor, the Christoffel symbol and covariant derivatives.

Essentially, we have two different covariant derivatives compatible with two different metrics: D_μ is the covariant derivative acting on the perturbed metric, and $D^{(B)}_\mu$ is the covariant derivative of the background metric. The difference between these two is given by a rank-3 tensor $C^\nu_{\mu\alpha}$, as such:

$$(D_\mu - D^{(B)}_\mu)V^\nu = (\Gamma^\nu_{\ \mu\alpha} - \Gamma^{\nu(B)}_{\mu\alpha})V^\alpha = C^\nu_{\ \mu\alpha}V^\alpha \tag{115}$$

$$\iff D_\mu V^\nu = D^{(B)}_\mu V^\nu + C^\nu_{\ \mu\alpha}V^\alpha. \tag{116}$$

One can make the association between Eq.(116) and the usual expression for a covariant derivative $D_\mu V^\nu = \partial_\mu V^\nu + \Gamma^\nu_{\ \mu\alpha}V^\alpha$: the $D^{(B)}_\mu V^\nu$ term corresponds to to the partial derivative $\partial_\mu V^\nu$ (which is just a covariant derivative in a flat background); and the difference between the two Christoffel symbols of the two metrics ($C^\nu_{\ \mu\alpha}V^\alpha$) corresponds to the Christoffel symbol in the expression for a covariant derivative ($\Gamma^\nu_{\ \mu\alpha}V^\alpha$) (which is just the "difference" between a flat and a curved background). Following chapter 3 of [47], one can write the higher-rank tensor generalization of Eq.(116) as such:

$$D_a V^{b_1\cdots b_k}_{\ \ c_1\cdots c_l} = D^{(B)}_a V^{b_1\cdots b_k}_{\ \ c_1\cdots c_l} + \sum_i C^{b_i}_{\ ad} V^{b_1\cdots d\cdots b_k}_{\ \ c_1\cdots c_l} - \sum_j C^d_{\ ac_j} V^{b_1\cdots b_k}_{\ \ c_1\cdots d\cdots c_l} \tag{117}$$

so that we can apply it to our metric.

Due to the compatibility of $D^{(B)}_\mu$ with the background metric $g^{\nu\lambda(B)}$ ($D^{(B)}_\mu g^{\nu\lambda(B)} = 0$) we arrive at an expression for the 3-rank tensor:

$$D^{(B)}_\mu g^{(B)}_{\nu\alpha} = D_\mu g_{\nu\alpha} - C^\lambda_{\ \mu\nu}g_{\lambda\alpha} - C^\lambda_{\ \mu\alpha}g_{\lambda\nu} = 0 \tag{118}$$

(the intermediate steps are done in Eq.s (3.1.24)-(3.1.27) of [47]) (119)

$$\iff C^\alpha_{\ \mu\nu} = \frac{1}{2}g^{\alpha\lambda}(D^{(B)}_\mu g_{\nu\lambda} + D^{(B)}_\nu g_{\mu\lambda} - D^{(B)}_\lambda g_{\mu\nu}). \tag{120}$$

It is also important to note that, due to the fact that we only consider up to linear orders in our perturbation $h_{\mu\nu}$, the inverse metric can easily be obtained as $g^{\mu\nu} = g^{\mu\nu(B)} - h^{\mu\nu} + \mathcal{O}(h^2)$.

We can simply plug in Eq.(120) our expression for the metric, as in Eq.(3), as well as the inverse one, and due to the compatibility of the background metric with the background covariant derivative, as well as the insignificance of the terms quadratic in h, we can rewrite our $C^\alpha_{\mu\nu}$ tensor:

$$C^\alpha_{\ \mu\nu} = \frac{1}{2}g^{\alpha\lambda(B)}(D^{(B)}_\mu h_{\nu\lambda} + D^{(B)}_\nu h_{\lambda\mu} - D^{(B)}_\lambda h_{\mu\nu}) + \mathcal{O}(h^2). \tag{121}$$

The next step in computing the Ricci tensor is, then, obtaining an expression for the Riemann curvature tensor and then contracting the first and third indices. Starting by the definition of the Riemann curvature tensor:

$$R^\mu_{\ \nu\rho\sigma} = \partial_\rho\Gamma^\mu_{\ \nu\sigma} - \partial_\sigma\Gamma^\mu_{\ \nu\rho} + \Gamma^\mu_{\ \alpha\rho}\Gamma^\alpha_{\ \nu\sigma} - \Gamma^\mu_{\ \alpha\sigma}\Gamma^\alpha_{\ \nu\rho}, \tag{122}$$

one can separate the Christoffel symbol into the background one + the one arising from the pertubation: $\Gamma^{\mu}_{\nu\sigma} = \Gamma^{\mu(B)}_{\nu\sigma} + \delta\Gamma^{\mu}_{\nu\sigma}$ and recover the expression for the background Reimann and then extra terms linear in $\delta\Gamma^{\mu}_{\nu\sigma}$ (once again, we ignore the quadratic ones) and get the following expression for the Riemann curvature tensor:

$$R^{\mu}_{\ \nu\rho\sigma} = \partial_\rho\Gamma^{\mu(B)}_{\nu\sigma} + \partial_\rho\delta\Gamma^{\mu}_{\ \nu\sigma} - \partial_\sigma\Gamma^{\mu(B)}_{\nu\rho} - \partial_\sigma\delta\Gamma^{\mu}_{\ \nu\rho} + \Gamma^{\mu(B)}_{\alpha\rho}\Gamma^{\alpha(B)}_{\nu\sigma} + \Gamma^{\mu(B)}_{\alpha\rho}\delta\Gamma^{\alpha}_{\ \nu\sigma} + \delta\Gamma^{\mu}_{\ \alpha\rho}\Gamma^{\alpha(B)}_{\nu\sigma} + \mathcal{O}(\delta\Gamma)^2 \tag{123}$$

$$- \Gamma^{\mu(B)}_{\alpha\sigma}\Gamma^{\alpha(B)}_{\nu\rho} - \Gamma^{\mu(B)}_{\alpha\sigma}\delta\Gamma^{\alpha}_{\ \nu\rho} - \delta\Gamma^{\mu}_{\ \alpha\sigma}\Gamma^{\alpha(B)}_{\nu\rho} - \mathcal{O}(\delta\Gamma)^2 \tag{124}$$

which, after grouping some terms together and manipulating a couple indices, gives us (125)

$$R^{\mu}_{\ \nu\rho\sigma} = R^{\mu(B)}_{\ \nu\rho\sigma} + (D^{(B)}_{\rho}C^{\mu}_{\ \sigma\nu} - D^{(B)}_{\sigma}C^{\mu}_{\ \rho\nu}) + \mathcal{O}(h^2). \tag{126}$$

The second term in this equation gives us, then, the first order perturbation of the Riemann curvature tensor in terms of the 3-rank tensor C. All there is left to do, is to insert Eq.(120) into Eq.(126), contract the first and third indices (μ and ρ) of the Riemann curvature tensor and equate it to zero. This will lead us to:

$$R^{(1)}_{\nu\sigma} = \frac{1}{2}\big(D^\lambda D_\nu h_{\sigma\lambda} + D^\lambda D_\sigma h_{\lambda\nu} - D^\lambda D_\lambda h_{\sigma\nu} - D_\sigma D^\lambda h_{\nu\lambda} - D_\sigma D_\nu(g^{\alpha\lambda}h_{\alpha\lambda}) + D_\sigma D^\alpha h_{\alpha\nu}\big) = 0. \tag{127}$$

(from now on, all of the covariant derivatives and $g^{\alpha\lambda}$ are referring to the background metric) (128)

The first thing we notice, is that in the fourth and sixth terms, λ and α are mute indices and they are actually the same thing, so we can cancel these two out ($h_{\mu\nu}$ is, of course, a symmetric tensor). Secondly, the first and second terms are just permutations of the indices μ and ν of each other. Thirdly, we can also see that $g^{\alpha\lambda}h_{\alpha\lambda}$ is actually the trace of the perturbation (h), and $D^\lambda D_\lambda$ is the background d'Alembertian operator $\Box$, so we can rewrite the equation as (we also substitute the indices ν and σ with μ and ν so that the notation aligns with the one from sec.1.2):

$$R^{(1)}_{\mu\nu} = \frac{1}{2}(-\Box h_{\nu\mu} - D_\nu D_\mu h + 2D^\lambda D_{(\nu}h_{\mu)\lambda}) = 0. \tag{129}$$

B Scalar wave equation in weak gravity

Here we will simply show the intermediate steps of solving the scalar wave equation (Eq.(26)) for the metric introduced in Eq.(19). To do so, let us first compute the components of our equation:

$$\sqrt{-g} = (1+2\Phi)^{1/2}(1-2\Phi)^{3/2}r^2\sin\theta \tag{130}$$

$$g^{tt} = -(1+2\Phi)^{-1} \simeq -(1-2\Phi) \quad \text{(because } \Phi \text{ is small)} \tag{131}$$

$$g^{rr} = (1-2\Phi)^{-1} \simeq (1+2\Phi) \tag{132}$$

$$g^{\theta\theta} = (1+2\Phi)r^{-2}, \quad g^{\phi\phi} = (1+2\Phi)r^{-2}(\sin\theta)^{-2} \tag{133}$$

Also important to note that, in weak gravity, the source of our potential is, to a good approximation, static, which means $\partial_t\Phi \sim 0$. This leads to the first term (time derivatives) of our equation to become:

$$\frac{1}{\sqrt{-g}}\partial_t(\sqrt{-g}g^{tt}\partial_t h_A) = g^{tt}\partial_t^2 h_A = -(1-2\Phi)\partial_t^2 h_A. \tag{134}$$

Remembering the Laplacian operator in spherical coordinates:

$$\nabla^2 = \frac{1}{r^2}\partial_r(r^2\partial_r) + \frac{1}{r^2\sin\theta}\partial_\theta(\sin\theta\partial_\theta) + \frac{1}{r^2\sin^2\theta}\partial_\phi^2, \tag{135}$$

one can also notice that the rest of the terms of our scalar wave equation ((r, θ, ϕ) derivatives) give the Laplacian of h_A with an extra $(1+2\Phi)$ term. Starting with the θ derivatives:

$$\frac{1}{(1+2\Phi)^{1/2}(1-2\Phi)^{3/2}r^2\sin\theta}\partial_\theta\left[\left((1+2\Phi)^{1/2}(1-2\Phi)^{3/2}r^2\sin\theta\right)(1+2\Phi)r^{-2}\partial_\theta h_A\right] = \tag{136}$$

$$\text{(remember } \partial_{\theta,\phi}\Phi = 0 \text{ because of spherical symmetry)} \quad = (1+2\Phi)\frac{1}{r^2\sin\theta}\partial_\theta(\sin\theta\partial_\theta h_A); \tag{137}$$

And similarly for ϕ:

$$\frac{1}{(1+2\Phi)^{1/2}(1-2\Phi)^{3/2}r^2\sin\theta}\partial_\phi\left[\left((1+2\Phi)^{1/2}(1-2\Phi)^{3/2}r^2\sin\theta\right)(1+2\Phi)r^{-2}(\sin\theta)^{-2}\partial_\phi h_A\right] = \tag{138}$$

$$= (1+2\Phi)\frac{1}{r^2\sin^2\theta}\partial_\phi^2 h_A. \tag{139}$$

For the radial derivatives, however, we get two terms: one which is, similarly as for θ and ϕ, simply the radial derivatives term of the Laplacian operator on h_A wiht a factor of $(1+2\Phi)$; the other one is the cross term, given by

$$\frac{1}{(1+2\Phi)^{1/2}(1-2\Phi)^{3/2}}\frac{1}{r^2}\partial_r\left((1+2\Phi)^{3/2}(1-2\Phi)^{3/2}\right)r^2\partial_r h_A. \tag{140}$$

Fortunately for us, after applying the product rule, this term becomes negligible since it's of the order $\Phi\partial_r\Phi \sim \mathcal{O}(\Phi^2/r)$, which means it's highly subleading compared to derivatives of h_A. This means that the contributions to the equation from the radial derivatives are as such:

$$(1+2\Phi)\frac{1}{r^2}\partial_r(r^2\partial_r h_A). \tag{141}$$

This allows us to write the scalar wave equation

$$-(1-2\Phi)\partial_t^2 h_A + (1+2\Phi)\nabla^2 h_A = 0 \tag{142}$$

in the form of Eq.(27) simply by multiplying everything by $(1+2\Phi)^{-1}$, simplifying into $(1-2\Phi)$ for a small potential and neglecting $\mathcal{O}(\Phi^2)$ terms.